5-19-2023

TOWARDS OPTIMAL OPERATION AND CONTROL OF EMERGING ELECTRIC DISTRIBUTION NETWORKS

Jimiao Zhang
Rowan University

TOWARDS OPTIMAL OPERATION AND CONTROL OF EMERGING ELECTRIC DISTRIBUTION NETWORKS

by

Jimiao Zhang

A Dissertation

Submitted to the
Department of Electrical and Computer Engineering
College of Engineering
In partial fulfillment of the requirement
For the degree of
Doctor of Philosophy
at
Rowan University
May 16, 2023

Dissertation Chair: Jie Li, Ph.D., Associate Professor, Department of Electrical and Computer Engineering

Committee Members:
Ying Tang, Ph.D., Professor, Department of Electrical and Computer Engineering, Rowan University
Ben Wu, Ph.D., Associate Professor, Department of Electrical and Computer Engineering, Rowan University
Shen-Shyang Ho, Ph.D., Associate Professor, Department of Computer Science, Rowan University
Tuyen Vu, Ph.D., Assistant Professor, Department of Electrical and Computer Engineering, Clarkson University

Dedication

This dissertation is dedicated to the memory of my two late grandmothers, Yongwen Xiong and Sumei Tian, who would have been able to witness my Ph.D. graduation. I adore both of you!

Acknowledgments

I would like to extend my heartfelt appreciation to my advisor Dr. Jie Li, for her guidance, motivation, and support throughout my research. I also would like to thank my committee members, Dr. Tuyen Vu, Dr. Ben Wu, Dr. Ying Tang, and Dr. Shen-Shyang Ho, for their advice and contributions to this study.

Furthermore, I am appreciative of Dr. Lei Wu at Stevens Institute of Technology and Dr. Thomas Ortmeyer at Clarkson University, who provided insightful recommendations on my research ideas in the first two years of my Ph.D. journey. Finally, I wish to thank my parents, Ping Zhang and Xiaomei Li, for their unwavering support and encouragement throughout my life.

I am excited and ready to embark on a new adventure in my life.

Abstract

Jimiao Zhang
OPTIMAL OPERATION AND CONTROL OF EMERGING ELECTRIC DISTRIBUTION NETWORKS
2022 - 2023
Jie Li, Ph.D.
Doctor of Philosophy

The growing integration of power-electronics converters enabled components causes low inertia in the evolving electric distribution networks, which also suffer from uncertainties due to renewable energy sources, electric demands, and anomalies caused by physical or cyber attacks, etc. These issues are addressed in this dissertation. First, a virtual synchronous generator (VSG) solution is provided for solar photovoltaics (PVs) to address the issues of low inertia and system uncertainties. Furthermore, for a campus AC microgrid, coordinated control of the PV-VSG and a combined heat and power (CHP) unit is proposed and validated. Second, for islanded AC microgrids composed of SGs and PVs, an improved three-layer predictive hierarchical power management framework is presented to provide economic operation and cyber-physical security while reducing uncertainties. This scheme provides superior frequency regulation capability and maintains low system operating costs. Third, a decentralized strategy for coordinating adaptive controls of PVs and battery energy storage systems (BESSs) in islanded DC nanogrids is presented. Finally, for transient stability evaluation (TSE) of emerging electric distribution networks dominated by EV supercharging stations, a data-driven region of attraction (ROA) estimation approach is presented. The proposed data-driven method is more computationally efficient than traditional model-based methods, and it also allows for real-time ROA estimation for emerging electric distribution networks with complex dynamics.

Table of Contents

Table of Contents (Continued)

Table of Contents (Continued)

Table of Contents (Continued)

List of Figures

Figure Page

List of Figures (Continued)

Figure Page

List of Figures (Continued)

Figure Page

List of Figures (Continued)

Figure Page

List of Tables

Table Page

Chapter 1

Introduction

1.1 Background and Overview

Across the globe, most people agree that global climate change is a pressing concern that demands swift solutions. Rising sea levels, shrinking mountain glaciers, more frequent and longer droughts, more severe hurricanes, and other extreme weather events have resulted from global warming. The main culprit for global warming is greenhouse gasses (GHGs) including carbon dioxide. In the U.S., the electricity generation sector alone constitutes up to 25% of all GHG emissions in 2019 [1]. As a result, one strategy for lowering GHG emissions is to switch out highly polluting fossil fuel generators with sustainable and eco-friendly renewable energy sources (RESs) such as solar and wind. However, as with other distributed energy resources (DERs) and loads that are geographically dispersed, these RESs are challenging to manage from the perspective of a bulk power system. They bring about lower inertia, uncertainties, reverse power flows, etc. For these reasons, the concept of active distribution networks (ADNs) came into being about two decades ago [2]. In contrast to passive distribution networks (PDNs) that are designed conservatively in their component capacities to handle worst-case scenarios, ADNs comprehensively embrace technological attempts to address operational issues through real-time monitoring and control, enabled by recent advancements in smart grid technologies, such as automation, computation, and communication. Specifically, microgrids serve as the foundation of ADNs for integrating multiple grid assets. A microgrid is defined by the Consortium for Electric Reliability Technology Solutions

(CERTS) as a collection of loads and micro-sources that operate as one system to supply both electricity and heat [3]. Indeed, a large electrical grid can be structurally split into smaller but self-sufficient grids that integrate DERs, energy storage systems (ESSs) (batteries, ultracapacitors, flywheels, etc.) and controllable loads (smart buildings, plug-in electric vehicles (EVs), etc.). According to Mordor Intelligence, the global microgrid market will be worth USD 25.45 billion by 2026, with a compound annual growth rate of 21.5% from 2021 to 2026 [4].

1.1.1 Classification of Microgrids

Microgrids can mainly be categorized into two types according to their operational setups: alternating current (AC) and direct current (DC). An AC microgrid is connected to the three-phase utility grid via a static transfer switch at the point of common coupling (PCC), while a DC microgrid is interfaced through a bidirectional DC-AC converter for common integration. Each type has its pros and cons. The DC microgrids have higher conversion efficiency because there are no additional DC-AC and AC-DC power conversion stages as seen in the AC microgrids. Furthermore, the transmission losses due to reactive current and skin effect in AC microgrids do not exist in the DC microgrids. Another advantage of DC microgrids is their controllability. Only the DC bus voltages need to be regulated rather than both the voltage magnitude and frequency. Moreover, frequency synchronization is no longer a concern to DC microgrids. Nonetheless, relay protection system design is more challenging for DC microgrids, since a natural zero-crossing point does not occur in DC systems. In addition, DC loads are not widely available yet because most of the electrical apparatuses are designed for the AC systems.

Other of microgrid variants are also noteworthy: the hybrid AC/DC microgrids [5], the networked microgrids (or ADNs) [6] and the nanogrids. A hybrid microgrid enjoys the combined benefits of individual AC and DC microgrids. In the concept of networked microgrids, multiple microgrids are operated in coordination with the distribution network to further enhance the shared reliability and resiliency of the power supply. Moreover, the nanogrids are considered as the building cells of a microgrid and have a wide range of applications.

1.1.2 Operating Modes of Microgrids

There are two basic operating modes for microgrids. **i)** A microgrid normally connects to the utility main grid and thus operates in the grid-connected node. In this case, the microgrid balances the electricity supply and demand by either purchasing electricity from the main grid or selling excess electricity to the main grid to maximize its operational benefits. The frequency and/or voltage stabilities rely on the main grid. **ii)** However, in the event of faults, scheduled maintenance, etc. on the main grid, the microgrid is expected to seamlessly transition to the islanded mode, and the DERs and ESSs should be dispatched to maintain the microgrid frequency and/or voltage stability in a self-governed manner. It should be noted that islanded microgrids are a highly viable option for isolated rural areas that lack or have expensive access to electricity and modern energy services.

1.1.3 Control Strategies for Microgrids

The implemented system control strategies play an enormous role in ensuring the power quality and efficiency of microgrids in both microgrids' operating modes. The hierarchical control architecture [8, 9] has been around for more than a decade, originally

inspired by the operation of bulk power systems [10], for which the system control architecture is commonly divided into three levels: primary, secondary, and tertiary, as shown in Figure 1.1. The primary level operates on the fastest timescale and automatically maintains frequency and voltage stabilities when there is an instantaneous imbalance between generation and demand. Primary control commonly relies on the local droop control, which utilizes only the local measurements without the need for additional communication links, thus making the system simple and reliable. The secondary control aims to eliminate the steady-state deviations in frequency (f) and voltage (v) caused by primary control, and it also handles restoration and synchronization. The tertiary level oversees economic dispatch (ED) and manages the active (P) and reactive (Q) power flows between the microgrid and the main grid. It is noted that the same control architecture also applies to the DC microgrids [11]. However, there would be no reactive power control and frequency control involved; instead, only the DC bus voltages are considered.

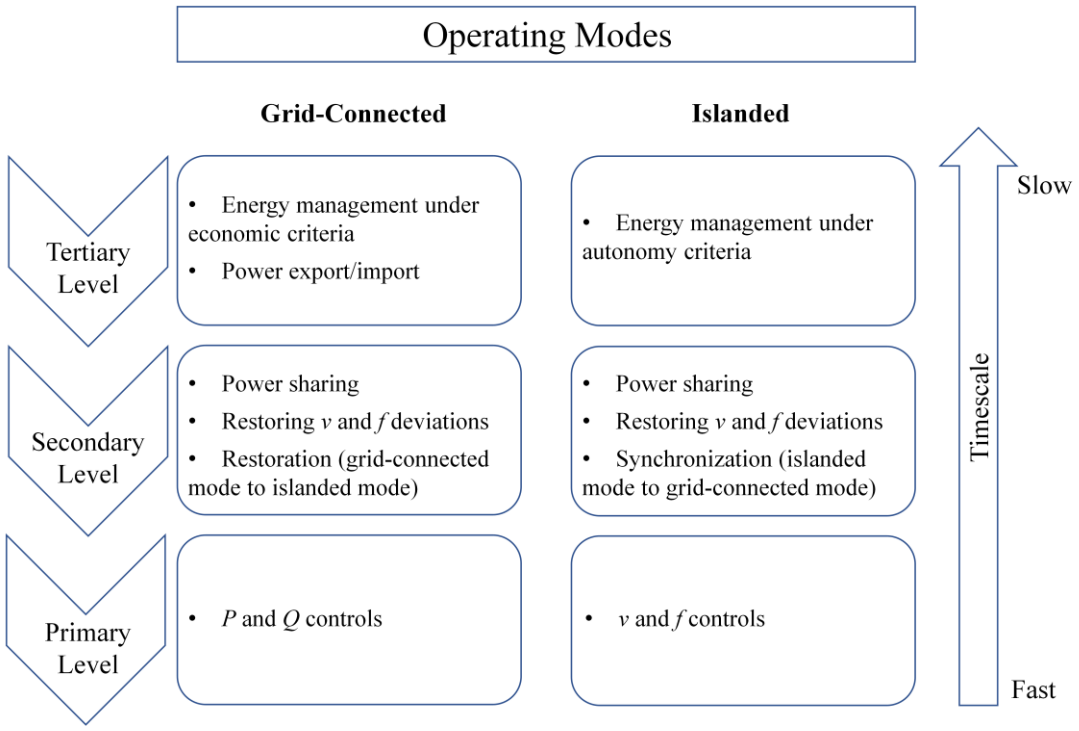

Figure 1.1. Hierarchical control architecture of AC microgrids.

Furthermore, the secondary control can be designed and implemented as a centralized control [12] or distributed control [13] manner . In the centralized control, a central controller collects system measurement information from all the nodes in the microgrid and executes the prescribed control algorithm before sending back the commands. Nevertheless, the centralized controller is eliminated in the distributed control, within which only local controllers communicate with their neighbors to execute local behaviors to achieve global optimal consensus. The distributed control strategies have well-recognized advantages including scalability, high reliability without a single point of failure, privacy preservation, low communication latency, etc. In comparison, the centralized control has higher observability and is structurally simpler with more

guaranteed convergence to the optimal solution. It was specifically pointed out in [14] that centralized control is better suited for an islanded microgrid with critical demand-supply balances as well as limited and fixed infrastructure, whereas distributed control could be a better fit for a grid-connected microgrid with expanding and/or dynamic infrastructure.

1.1.4 Major Challenges in ADNs and Microgrids

The implementations of ADNs and their building blocks, i.e., microgrids are faced with various technical challenges, some of which are intertwined. They are briefly summarized as follows:

- **Economic loss**: The voltage limits and the power line limits could be violated more easily with an increasing penetration of RESs in ADNs and microgrids, which may further introduce large system disturbances, preventing the local component controllers to closely follow the economic power setpoints.

- **Low inertia**: More DERs and ESSs are being integrated to the ADNs and microgrids through the interface of power-electronics converters, but these devices have no rotational kinetic energy as in the conventional synchronous generators (SGs). The ADNs and microgrids thus lack spinning reserves and experience decreasing system inertia. Consequently, considerable frequency and/or voltage deviations as well as system instability are likely to occur, particularly when ADNs and microgrids are islanded.

- **Uncertainty**: The system uncertainties introduced by the intermittency in RESs such as solar and wind due to varying meteorological conditions along with the

stochasticity in electricity consumptions make the reliable and economic operation of ADNs and microgrids more difficult.

- **Cyber-physical threats**: In the ADNs and microgrids, the cyber components and the underlying physical systems are tightly coupled. More frequent potential cyber-physical threats could disrupt the normal operation of ADNs and microgrids, causing system collapse, cascading failure, etc. Thus, advanced monitoring and control are critical to ensuring cyber-physical security and resiliency.

- **Transient instability:** Integration of RESs reduces the system's inertia, while the power electronics converters interface loads such as EV chargers and introduce negative damping. Both pose a new challenge to the transient stability of ADNs and microgrids, which is not common in conventional bulk power systems. In addition, system modeling of ADNs and microgrids is made more difficult by the increasing number of distributed power-electronics-based devices, their intricate control loops, and the broad time scales of control dynamics. Hence, systematic and efficient transient stability studies should be conducted for the safe and stable operation of ADNs and microgrids.

1.2 State of the Art in Addressing Distribution Network Operational Challenges

1.2.1 Control of Solar PV Systems in ADNs and Microgrids

Solar PV systems, one of the key components of emerging ADNs and microgrids, are traditionally operated in maximum power point tracking (MPPT) mode to take full advantage of the free and clean solar energy and thereby minimize the levelized cost of energy (LCOE) of local supply, particularly when the ADNs or microgrids are connected

to an AC main grid. In this case, frequency and voltage of the ADNs or microgrids are supported by the external AC grid. As more solar generations are integrated, the existing distribution lines and substations are being stressed out. One solution is to upgrade the infrastructure of the electric grids; yet the associated exorbitant costs pose an economic hurdle. Another potential challenge facing the power system operation is the sudden ramp up or down of electricity net demand (i.e., total demand minus generation) during certain periods of time in one day, giving rise to large grid voltage fluctuations. Resolution of this issue requires other dispatchable energy sources to respond fast to meet the sharp fluctuations when solar power is under-supplied or over-supplied. A similar issue has been reported by the California Independent System Operator (CAISO) in its bulk system [15]. When there is an oversupply of solar power, some system operators may opt to limit PV installations, which however runs counter to the national and state level long-term energy strategies. Alternatively, the generated solar power could be curtailed, as is CAISO's current practice. This option is not economically sound, though. For these reasons, it is desired that the PV systems be flexibly controlled instead of being controlled only in MPPT mode. In addition, without support from a stiff external grid during emergencies when islanding is enforced, the high penetration of renewables including solar PVs has presented an even greater operational challenge to ADNs and microgrids. Conventionally, the SGs provide damping, and absorb or release the kinetic energy stored in the rotating masses to arrest sudden frequency deviations once there is an active power imbalance [16]. Since inverter-based resources (e.g., solar PV) are replacing SGs while not providing the same natural inertia as the SGs, the ADNs and microgrids are experiencing greater frequency excursions and higher rates of change of frequency (RoCoF) especially when operated in

islanded mode. Frequency-related generator/load protection tripping has been increasingly frequent. All these challenges call for advanced control strategies to improve the stability and reliability of emerging renewable-dominated grid systems.

In principle, the PV systems operated in MPPT mode are controlled using grid-following inverters, which rely heavily on the grid voltage and angle measurements to remain synchronized with the rest of the grid [17]. Hence, the small-signal stability margins could be greatly reduced with sudden changes in the measured grid signals. Droop control, on the other hand, is normally implemented for grid-supporting inverters. Droop control is equivalent to the primary frequency regulation of SGs governed by a speed governor with a slow response. However, it does not contribute to the system's inertia and damping and cannot respond to fast grid frequency swings during transient states. To date, some efforts have been directed towards controlling the PV systems to mimic the electromechanical characteristics of conventional SGs for improved damping and inertial response. Figure 1.2 illustrates the frequency response improvements with virtual inertia in the event of a generation loss, as well as the typical corresponding timescales of different power system controls.

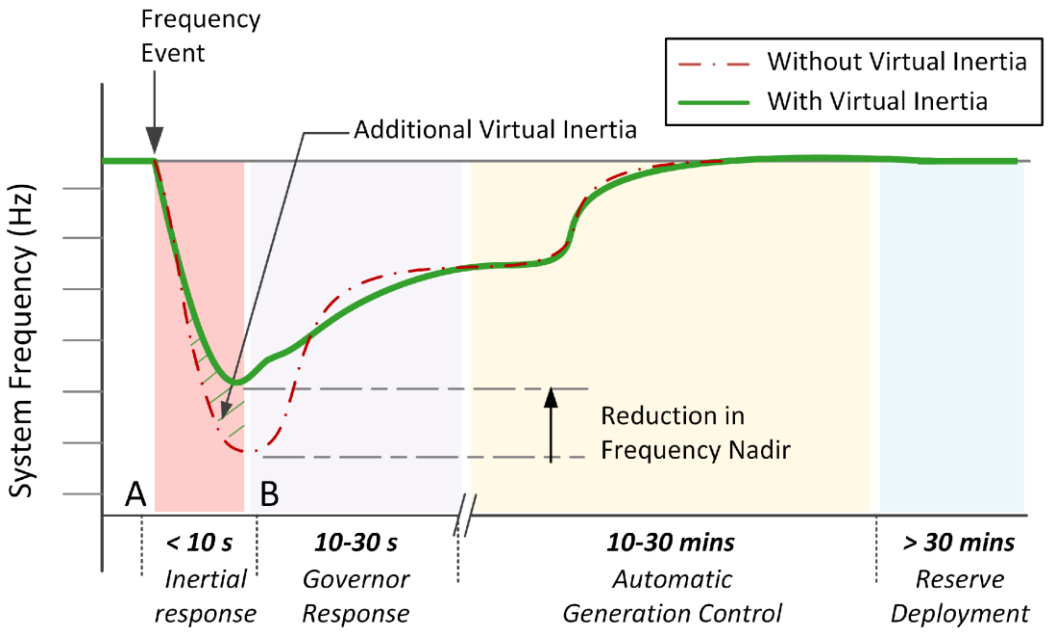

Figure 1.2. Multiple time-frame frequency response following a frequency event [18].

In virtual SG (VSG) technologies, an additional inertia control loop is commonly integrated into the control loops of grid-supporting inverters [19] to emulate inertia. There are primarily two types of PV-VSG approaches depending on whether ESSs are utilized. In some studies, ESSs and their bi-directional DC-DC converters are placed at the DC link to stabilize the voltage [20, 21]. Nevertheless, the addition of ESSs would incur additional operation and maintenance costs. In addition, the contribution of PV cannot be explicitly justified because the primary regulation is only provided by the ESSs. Other methods eliminate ESSs, and the PV-VSGs are controlled away from the MPP to provide active power reserve [22-24] or using the DC-link capacitor of the inverter to provide inertia support [25, 26]. However, a phase-locked loop (PLL) was required in [21-23, 26], which might cause instability issues, particularly in a non-stiff grid [27]. Further, some papers such as [22, 28] adopted a single-stage topology and limited the PV voltage operating range

to the right side of the MPP for stability concerns. Also, the dynamics of the PV are affected by those of the inverter. To this end, the addition of a DC-DC stage is preferred. Moreover, the proposed PV-VSG schemes in [25, 26] were validated only in a single-ESS system. Since solar power shortage is possible, control of a PV-VSG without ESSs needs to be coordinated with other DERs, particularly in islanded microgrids. Combined heat and power (CHP) units [29-33] could bring significant energy cost savings to the electricity consumers and reduce carbon emissions. Therefore, they are an ideal candidate to coordinate with the operation of PV-VSGs. For CHP modeling, Rowen's model is well known for being more explicit in terms of control functions than the others. It was originally created for industrial heavy-duty gas turbines (GTs). However, one limitation to the Rowen's model is that system and control parameters need to be customized based on the actual CHPs.

1.2.2 Power Management of Microgrids with Uncertainties

Uncertainty management is a challenge for the operation of microgrids and other electric power systems due to the prevalence of RESs and demand variation. Along with the intermittency in RESs, the randomness in electricity consumption behaviors compounds the uncertainties in microgrids, particularly when the microgrids are in islanded mode. The difficulty of coping with the adverse impacts of RESs and local loads on the power quality poses severe challenges to the system's power management. For instance, the local controllers acting on frequency and voltage deviations need to respond more quickly and frequently due to high uncertainties. Apart from the commonly observed high deviations in system frequency and voltage, real-time ED of distributed generators

inside the microgrid may also be compromised, because the actual power outputs will deviate greatly from the optimal power commands. Meanwhile, for an islanded microgrids with low inertia, unpredictable demand responses, and high penetrations of RESs, the system's states could be extremely volatile. Moreover, microgrids, as one type of cyber-physical systems, are becoming increasingly vulnerable to extreme weather events, component outages, and cyber-physical attacks [34], which are generally termed as anomalies. These anomalies may lead to unreliable transmission of sensor measurements and control signals, thus threatening microgrid security.

Whether a microgrid is islanded or connected to the main grid, the primary operational goal of the microgrid control system is to ensure stable delivery of electrical power to its local loads using DERs in a reliable and cost-effective manner in the face of uncertainties. The uncertainties in generation and demand can be managed or mitigated by using energy storage systems (ESSs) to achieve power balance [35], implementing demand-side management [36] or improving generation and load forecasting techniques [37, 38]. A host of studies have tried to address this challenge via advanced modeling approaches, e.g., stochastic programming (SP) [39, 40], robust optimization (RO) [41-43], or chance-constrained programming (CCP) [44, 45], wherein the microgrid system uncertainties are explicitly modeled. Nonetheless, performance of these methods is highly constrained by the accuracy of the uncertainty modeling, and they are based on offline open-loop optimization, which may have limited robustness to external disturbance or noise compared with the closed-loop feedback mechanism. Hence, potential performance degradation and computational complexity are commonly criticized in practical applications.

Advanced control strategies, such as model predictive control (MPC), are the subject of another line of research [46]. MPC provides an inherent feedback mechanism, which makes the system more robust against uncertainties. Furthermore, the ability of MPC to explicitly incorporate physical constraints alongside forecasting information enables constrained optimal control. The rising popularity of MPC theories has indeed spurred a growing interest in their applications in microgrid power management [47-50]. Velasquez *et al.* [51] presented a single-level distributed MPC for solving the intra-hour ED of a microgrid. The controller keeps adjusting the generation schedules in real time along with updated forecasting. To cope with inevitable forecast errors, a two-level stochastic MPC scheme was proposed in [52] to minimize the discrepancy between the actual energy exchange and the optimally planned one. A supervisory MPC was presented in [53] to ensure reliable and economic operation of islanded hybrid AC/DC microgrids. In [54], a hierarchical predictive controller executed daily scheduling and real-time control of a PV microgrid, with ESSs and diesel generators making up for the load and RES fluctuations. Among all these MPC-based research, linear MPC is preferred for its capability of dramatically reducing the complexities in controller design and control signal computation. Furthermore, the designed controllers can still provide corrective actions for enhanced system robustness in the presence of disturbances [55, 56].

It should be noted that the performance of MPC depends highly on the prediction model's accuracy, which in turn relies on the system's current states. Aside from cost optimization, the control system should also encompass monitoring functions. Monitoring provides overarching information about the current system's states for increased situational awareness. This information supports not only optimal control decisions but also prediction

of the system's future states and events. However, one common assumption in all the above works is that the system states are already known or directly measurable when MPC is implemented, which is not necessarily the case when the states are volatile. Furthermore, state variables of conventional SGs, such as rotor angle and field winding voltage, cannot be directly measured in practice [57-59]. Although the Kalman filter and its variants have been adopted to detect anomalies in sensor readings by means of analytical redundancy [60] and to estimate unmeasurable system states [61], they are unable to detect such anomalies in the manipulation of control signals. Lastly, many MPC-based approaches, e.g., [47] and [51], employed static system models for secondary control, following the convention of bulk power systems that this control level is implemented on a timescale of minutes. However, forecasting errors of load and renewables will increase when the secondary control is executed on a longer timescale. Thus, to simultaneously track the economic power commands from the tertiary controller and react to high fluctuations on the grid, it is desired for the secondary controller to operate in shorter time control intervals (i.e., several seconds) using near real-time forecasting techniques with reduced prediction errors. On the other hand, unlike power electronics converters whose dynamics may decay quickly in several milliseconds, conventional DGs such as electrically excited SGs have relatively slow dynamics that cannot be ignored on the timescale of a few seconds. On this timescale, a dynamic system model would be preferred. To ensure the economic benefits and security of microgrids, an advanced MPC control system is thus necessary.

1.2.3 Decentralized Control

Decentralized control is advantageous because the active elements of emerging electrical distribution networks can operate in concert with one another using locally available information. No complex communication is required. Due to their system efficacy, size, and cost, DC electrical networks are more attractive than their AC counterparts. In islanded DC microgrids/nanogrids, the PV MPPT strategies will not work properly unless additional battery energy storage systems (BESSs) are available to regulate the common DC bus voltage. Even if the PVs can operate in the MPPT mode, the grid may experience DC bus overvoltage and overcharging of batteries in view of the increasing penetration of PVs and the limited state of charge (SoC) of BESSs. In the other extreme case, the BESSs could over-discharge to supply the loads once the on-site PVs become unavailable. In either case, the lifespan of BESSs will be shortened and the grid voltage stability will be adversely affected. Hence, it is desired that PVs possess a certain degree of voltage regulation capabilities.

Coordinated control between PVs and BESSs is critical to maintaining the common DC bus voltage and the power balance. Indeed, there has been extensive research in operating PVs also in a power-limiting mode such that they can regulate the common DC bus voltage along with BESSs [62, 63]. Nevertheless, these methods rely heavily on communications links for smooth mode switching, thus decreasing the system reliability with potential communication failure. For this reason, communication-less decentralized control methods such as droop control have been favored for PV-BESS coordination [64, 65]. In [66], cooperative adaptive droop was employed for BESSs to design a unified

energy management system. However, the criteria for operating mode switching were complicated and the transient performance was limited between switches. The $v - \frac{dp}{dv}$ droop methods [67, 68] sensed the DC bus voltage and integrated the MPPT and the DC bus voltage regulation into a single control configuration. However, this scheme might suffer from slow transient responses in the case of a sudden change in environmental conditions because it utilized a fixed PV voltage search step. To this end, [69] presented a $v - \frac{dp}{di}$ droop strategy with improved dynamic responses and power quality. But as with [67], this technique necessitates accurate measurements, and differentiation of the PV mathematical model may result in severely incorrect control set-points in practice. Paper [70] reported a proportional droop index algorithm to adjust the droop coefficient of a PV unit, yet it still requires real-time measurements of each load demand to implement the operating mode selection. A PV-BESS coordinated control method was proposed in [71]. The SoC-based droop control allowed the BESSs to provide DC bus voltage regulation with balanced SoCs. However, overcharging BESSs also poses hazards, and their protection was not considered in this study. Overall, most of this line of research in the existing literature relies heavily either on reliable communication links or on complicated mode switching criteria that are hard to implement in practice. Hence, it is desired to have a simple and efficient decentralized control scheme that accounts for BESS over-discharging and over-charging protection.

1.2.4 System Stability Evaluation

With the widespread deployment of power-electronics devices into ADNs and microgrids to integrate renewables, ESSs, EV charging stations, etc., the emerging electric

power grid's functionality has been considerably enriched. However, the ADNs and microgrids differ from conventional bulk power systems on several fronts. Firstly, they have different dynamic characteristics. In the bulk systems, the main system state variables are invulnerable to disturbances due to the wide presence of SGs which possess large inertia and damping capabilities. In contrast, the dynamics of ADNs and microgrids are more susceptible to high volatility due to lower inertia and higher stochasticity in renewables and loads. Additionally, the electromechanical stability of SGs is of major concern in bulk systems, and it is mainly related to slow controls whose dynamics are below the fundamental frequency. Nevertheless, in power-electronics-dominated ADNs and microgrids, a wider range of dynamics must be taken into account, as shown in Figure 1.3. Secondly, accelerated deployment of high-power EV charging stations is expected to alleviate range anxiety, while imposing stress on the existing ADNs and threatening their transient stability. The loads (such as EVs) tightly regulated by power-electronics converters behave as constant power loads (CPLs) of the ADNs and microgrids with negative impedance characteristics [72], thus further reducing the effective system damping. Thirdly, higher complexity in system-level modeling and analysis ensues because of an increased uptake of distributed energy assets with dedicated control systems.

A growing body of research has been conducted on the stability analysis of ADNs and microgrids. These methods are based on small-signal modeling or large-signal modeling. The small-signal stability evaluation mainly comprises the eigenvalue analysis and the impedance-based methods. The time-domain eigenvalue methods obtain a linear-time invariant (LTI) state-space model by linearizing the system model around an equilibrium operating point. Calculating the eigenvalues of the state matrix enables the

identification of oscillation modes and instability roots [73]. However, the eigenvalue analysis method requires full system information, which may be confidential due to private ownership of assets. For the impedance-based methods applicable to the frequency domain, the system of interest is simplified as one aggregated source subsystem and one aggregated load subsystem. Stability can then be studied using the Nyquist criterion [74]. While the impedance-based methods have good scalability in model representation and can be implemented based only on measurements with frequency sweeping, they provide highly conservative results and cannot identify the oscillation modes. Notably, the aforementioned small-signal stability analysis methods may become ineffective for power systems characterized by nonlinearity, high orders, and large disturbances due to the approximation/simplification inherent in their system modeling.

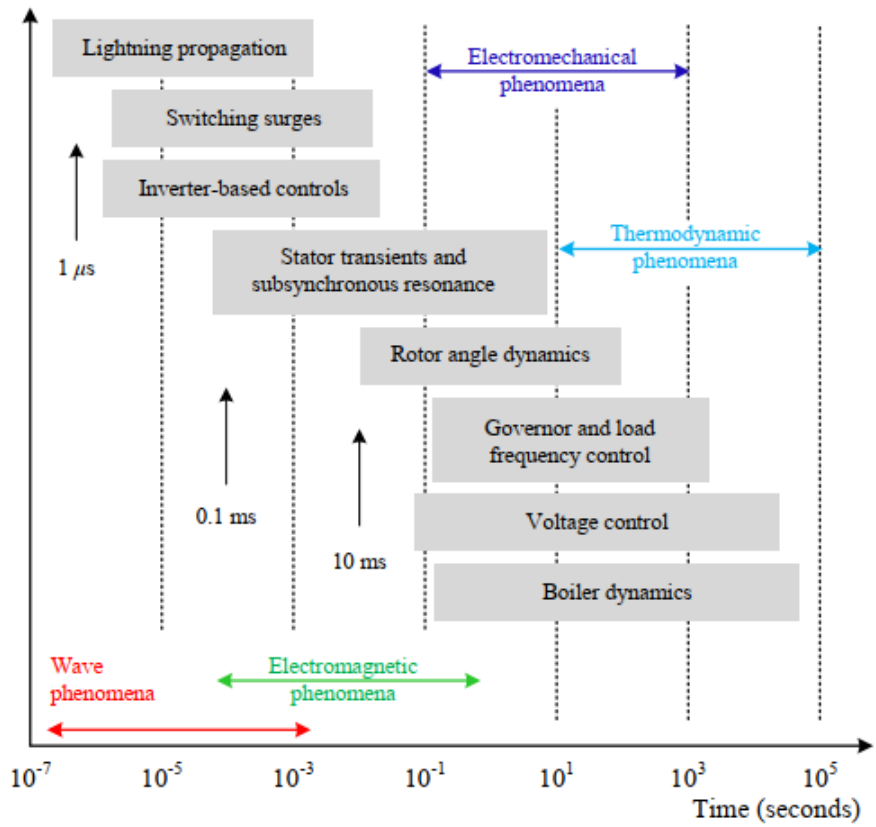

Figure 1.3. Multi-timescale dynamics of power-electronics dominated power systems [75].

To this end, large-signal stability (a.k.a. transient stability) is being researched to ensure situational awareness for the system operator and stable system operation. Transient stability evaluation (TSE) mainly utilizes stability theory by Lyapunov's direct method to quantify how large disturbances a system can tolerate by estimating the region of attraction (ROA) of a locally asymptotically stable equilibrium point [76]. The crux of this type of research is to find an appropriate Lyapunov function which often lacks a general method. The Takagi-Sugeno (TS) multi-modeling method originally proposed in [77] for system identification was employed for ROA estimation of an inverter-motor drive system [78] and a droop-controlled inverter connected to an infinite bus [79], respectively. In [80], the

transient stability of a multi-bus inverter-based dynamic microgrid was analyzed, where the adopted T-S multi-modeling further took account of communication delays. Although the above T-S multi-modeling works well for small-scale power systems, it will encounter the curse of dimensionality when the system orders and nonlinearities increase. While model order reduction such as Kron reduction [81] can be performed to reduce computation burdens, certain important system dynamics might be lost. In addition, Brayton-Moser's mixed potential theory has been widely applied to ROA estimation of power systems that are simplified as RLC networks. The equilibrium of an RLC network is guaranteed to be stable if it is a local minimum of the constructed mixed potential function. In [82], a DC microgrid under droop control was simplified and its ROA was estimated. However, such simplification of models always leads to conservativeness in ROA estimation. To mitigate conservativeness and increase scalability, [83] presented a revised mixed potential theory, where the operating bounds of practical CPLs were accounted for and the state variables with strong and weak correlations to stability were separated. Some works leverage mathematical optimization to calculate the maximum ROA from a proper Lyapunov function [84]. The transient stability of grid-connected converters with PLLs was studied in [85] using an iterative sum-of-squares programming (SOSP) method. Nonetheless, the use of SOSP is generally limited to polynomial systems, and the system discussed only consisted of one converter. It is thus unclear if the proposed method would be computationally efficient for an ADN dominated by many distributed assets such as EV charging stations. Reference [86] estimated the ROA of a DC microgrid with CPLs, and the proposed SOSP-based method showed higher accuracy than other mainstream model-based approaches.

As an alternative to the Lyapunov-based approaches, geometric methods such as normal form analysis have also been applied to ROA estimation [87]. However, these geometry tools are constrained by their locality and low dimensionality [88]. Besides, authors of [89] applied the theory of occupation measures to approximate the ROA of power systems comprising SGs. Nevertheless, the method's suitability relies heavily on polynomial reformulation of the original dynamical system models.

It should be noted that all above-mentioned model-based methods only considered power systems with homogenous bus dynamics (viz., either all power electronics converters or all SGs). However, SGs and power electronics converters, which are key components of future ADNs and microgrids, have considerably different dynamic characteristics. Another common limitation of these methods is that their ROA estimation accuracy hinges on accurate system modeling, which is always compromised by their simplified mathematical models in exchange for acceptable solution times. Practical ADNs and microgrids are generally highly nonlinear with complex dynamics. The systems are exposed to uncertainties in model parameters due to varying operating conditions, let alone the high uncertainties attributed to stochasticity of load consumption (such as EV charging) and intermittency of renewables. Moreover, the uncertainties could be compounded by the fact that control algorithms of the distributed assets are usually proprietary and unknown to the user. Meanwhile, with a wealth of operational data available from smart meters and micro-phasor measurement units (μPMUs) and advances in data analytics, the data-driven TSE becomes more appealing.

1.2.5 Data-Driven System Analysis Methods

Conventionally, the behavior of complex nonlinear dynamical systems including electric power grids is analyzed by explicitly solving equations of motion, which can be difficult or impossible to solve. Recently, data-driven approaches are more attractive are becoming more attractive due to their model-free nature. In emerging electric power systems, smart sensors and other advanced monitoring devices are providing large volumes of system operation data, which makes data-driven system analysis methods more feasible. Specifically, the prominent features of the Koopman operator theory have lent itself to a wide range of data-driven applications in electric power systems, such as dynamic state estimation [90], power flow calculations [91], system identification [92], and model predictive control (MPC) of wind farms [93], etc. The Koopman operator theory is an operator-theoretic formalism of classical dynamical system theory, which enables a scalable reconstruction of the underlying dynamical system using only measurement data. In addition, it provides a principled linear embedding of nonlinear dynamics, which can reduce computational complexities. Using the Koopman Operator theory, information regarding the system's behavior can be extracted directly from data. Most notably, this theory finds its application in TSE, since its spectral properties could properly capture the system’s stability properties [94]. In [95], unstable power flow patterns were detected by applying the Koopman mode analysis (KMA) to historical power flow data, while the characteristics of mutual interference between microgrid voltage stability and frequency stability were extracted from simulation data in [96]. However, both studies employed the Arnoldi-type method to approximate the Koopman operator, where linear basis functions were utilized which cannot sufficiently capture the system’s strong nonlinear behavior

sufficiently. Further, the spectral analysis results are generally posterior, and thus not as comprehensible and straightforward as the ROA visualization. Reference [97] proposed a ROA estimation scheme using the extended dynamic mode decomposition (EDMD) method [98], which was heuristic and lacked rigorous theoretical guarantees for system stability. Moreover, the EDMD method could lead to instability and long-term approximation errors in the learned Koopman operator due to its single-time-step approximation [99]. To overcome the aforementioned deficiencies and pursue rigorous theoretical guarantees for system stability without compromising computational efficiency, further research is required to develop an efficient data-driven TSE approach.

1.3 Research Motivation and Objectives

To fill the gaps identified in the state-of-the-art research, this dissertation focused on addressing the following challenges:

- Control of solar PV systems as VSGs to address the challenges of **low inertia**, **uncertainty**, and **transient instability** that are common to ADNs and microgrids.

Specifically, the researcher proposes a double-stage PV-VSG model that can be flexibly controlled away from the MPP. The PV-VSG only uses its DC-link capacitor to simulate inertia, and even small capacitances can be used to make a large amount of virtual inertia. Furthermore, the PV-VSG does not necessitate PLLs to avoid PLL-associated instability issues. Rowen's single-shaft GT prototype model will also be modified to more closely resemble the common GTs used in CHPs. Lastly, coordinated control between a PV-VSG and a CHP unit will be conducted under large solar irradiance intermittency for the stable operation of an AC microgrid in islanded mode.

- Predictive hierarchical power management to address the challenges of **economic loss**, **uncertainty**, and **cyber-physical threats** in islanded microgrids.

An enhanced predictive hierarchical power management framework is proposed to systematically integrate and coordinate the core system operational functions of microgrids, i.e., frequency regulation, optimal power flow, and state estimation via an enhanced predictive hierarchical power management framework for the economic and secure operation. Specifically, an MPC controller is proposed for the secondary control, which is highly responsive to system frequency fluctuations and renewable power variations. The controller is designed based on a linearized dynamic system model that is periodically updated at runtime for uncertainty mitigation. Furthermore, an optimal recursive filter is proposed for joint estimation of the system states and the control signals received by primary controllers in an unbiased minimum-variance (UMV) sense for cyber-physical resilient MPC control capabilities.

- Coordinated and decentralized control of PVs and BESSs to tackle the challenges of **low inertia** and **uncertainty** in islanded DC power grids.

A simple adaptive control scheme is proposed for the PVs to switch seamlessly between the *V-P* droop mode and the MPPT mode with satisfactory dynamic response. When the DC bus voltage is high enough, the PVs follow the droop curve and limit their power outputs, thus participating in DC voltage regulation. If the DC bus voltage decreases below a certain threshold, PVs will adaptively switch to the MPPT mode to provide full power support. In addition, an SoC-based adaptive droop control technique is implemented for the BESSs interfaced by the dual-active bridge (DAB) DC-DC converters. The

proposed technique can mitigate overcharging and over-discharging of the batteries by adaptively adjusting the DC bus voltage references. Lastly, the proposed coordination scheme will be rigorously simulated, which allows enhanced voltage regulation and power sharing among PVs and BESSs in a plug-and-play fashion, without the need to measure loads.

- Data-driven transient stability evaluation of ADNs and microgrids dominated by EV supper charging stations to combat the issues of **low inertia**, **uncertainty**, and **transient instability**.

To address the limitations of the model-based ROA estimation methods, a data-driven approach to estimating ROAs based on the Koopman operator theory is proposed. Specifically, a stable Koopman operator is first learned by imposing stability constraints in a data-driven gradient-descent algorithm (the SOC), instead of applying the EDMD. Numerically stable Koopman eigenfunctions are approximated from the ADN/microgrid operating data and then employed to establish a set of linearly parameterized Lyapunov candidate functions. Such a design can reduce the number of decision variables for improved computational efficiency, compared with other optimization-based methods such as the SOSP. And it is also directly interpretable from the perspective of Koopman spectral analysis and stability properties. Various trajectory data are then rigorously applied to form a tight feasible polytope. Through efficient sampling and linear optimization, the union of invariant sublevel sets of the determined Lyapunov functions can constitute a tight inner approximation to the actual ROA in real-time.

1.4 Dissertation Structure

Below, Figure 1.4 shows the structure of this Ph.D. dissertation. Chapter 1 introduces the state of the art in operation and control of emerging electric distribution networks (microgrids, nanogrids, and ADNs) and sets forth the major challenges, research motivation and objectives. In Chapters 2 through 5, four major projects conducted during the author's Ph.D. studies are discussed, which try to address the major challenges of emerging electric distribution networks in different system settings. Chapter 6 concludes the findings of the Ph.D. projects and discusses the future work along this line of research.

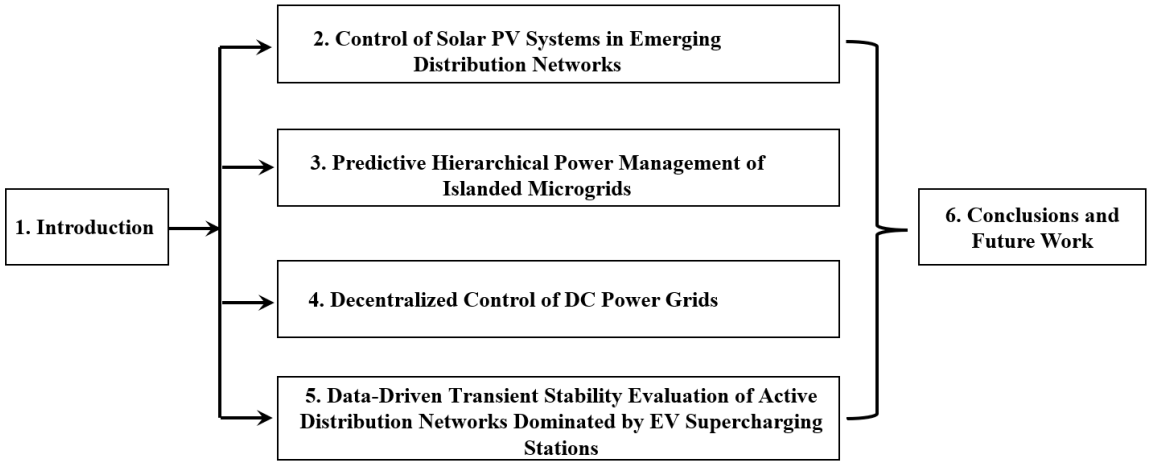

Figure 1.4. Dissertation structure.

Chapter 2

Control of Solar PV Systems in Emerging Distribution Networks

2.1 Introduction

Using RESs such as solar and wind to generate electricity rather than fossil fuels drastically reduces GHG emissions from the electric power sector and helps to mitigate the impacts of climate change. However, these types of renewables are highly weather-dependent. For instance, due to variability and intermittency in solar irradiation, solar PVs may frequently experience high output power fluctuations, which can cause grid frequency fluctuations. Furthermore, in ADNs and microgrids with resistive distribution lines, the rapid change in active power outputs also causes grid voltage fluctuations. Such adverse impacts will become more pronounced as PV systems become more widely deployed and are expected to dominate future electric power distribution networks. Thus, high-performance controls of solar PV systems are crucial to the reliable operation of emerging ADNs and microgrids. The principles of PV and their commonly used MPPT control strategies are reviewed, and the modeling and control of a grid-connected PV-BESS system are implemented when PV penetration in the grid is low. The PV-VSG strategy and its coordinated control with CHP units are then presented as PV penetration increases in ADNs and microgrids.

2.1.1 Modeling of Solar PV Systems

For a solar PV system, the effective utilization of its solar cells depends not only on the internal characteristics but also on external factors such as solar radiation, temperature, and loading conditions. The PV cells are constructed using differently doped

semiconducting materials with the *p-n* junction exposed to light. Equivalent electrical circuit-based models are commonly used to simulate PV cells. Figure 2.1 presents the equivalent circuit of a practical PV cell, which is sometimes termed as the five-parameter model [100].

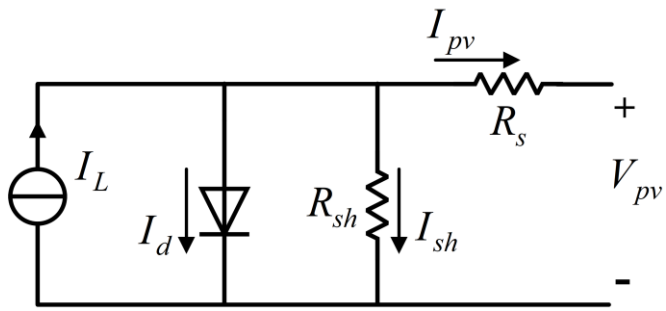

Figure 2.1. Single-diode model of a practical PV cell.

In the absence of solar irradiation, the PV cell behaves as a simple *p-n* junction diode, and its characteristics is governed by the well-known Shockley diode equation:

$$I_{d,c} = I_{o,c}\left[\exp\left(\frac{q\left(V_{pv,c} + R_{s,c} \cdot I_{pv,c}\right)}{akT}\right) - 1\right] \tag{2.1}$$

where the subscript c stands for "cell", $I_{o,c}$ is the diode saturation current (A), a is the ideality factor, and k is the Boltzmann's constant ($-1.380653 \times 10^{-23}$J/K). Furthermore, q means the absolute value of electron's charge ($-1.60217646 \times 10^{-19}$ C) and T denotes the cell temperature (K). $R_{s,c}$ depicts the losses due to the contact resistance between the

silicon and electrode surfaces, the current flow resistance in the silicon material and the resistance of the electrodes.

In Figure 2.1, the following current relationship holds:

$$I_{pv,c} = I_{L,c} - I_{d,c} - I_{sh,c}$$
$$= I_{L,c} - I_{o,c}\left[\exp\left(\frac{q\left(V_{pv,c} + R_{s,c} \cdot I_{pv,c}\right)}{akT}\right) - 1\right] - \frac{V_{pv,c} + R_{s,c} \cdot I_{pv,c}}{R_{sh,c}} \tag{2.2}$$

where $I_{pv,c}$ is the cell terminal current (A) and $V_{pv,c}$ is the cell terminal voltage (V). $I_{L,c}$ represents the photo-generated current (A). $R_{sh,c}$ is used to account for the leakage current in the *p-n* junction.

In practice, multiple PV cells are configured in parallel and series connections to constitute a PV module. Furthermore, PV modules are assembled as a PV panel or even a PV array. Without loss of generality, it is assumed that a PV array consists of N_p strings connected in parallel, and each string contains N_s PV cells connected in series. R_{sh} and R_s are the equivalent shunt and series resistances of the PV array, respectively. Thus, the equivalent terminal current-voltage relationship for the PV array is expressed as:

$$I_{pv} = N_p \cdot I_{L,c} - N_p \cdot I_{o,c}\left[\exp\left(\frac{q\left(V_{pv} + R_s \cdot I_{pv}\right)}{N_s akT}\right) - 1\right] - \frac{V_{pv} + R_s \cdot I_{pv}}{R_{sh}} \tag{2.3}$$

When the effects of solar irradiance (G) and cell temperature (T) are considered, the photo-generated current becomes

$$I_L = \frac{G}{G_{STC}}\left[I_{L,STC} + K_i(T - T_{STC})\right] \tag{2.4}$$

where the subscript *STC* refers to the Standard Test Conditions defined by IEC-60904-3, where $G_{STC} = 1000\ \mathrm{W/m^2}$ and $T_{STC} = 298.15\ \mathrm{K}\ (25^o\mathrm{C})$. K_i is a temperature coefficient.

The diode saturation current only depends on the cell temperature:

$$I_o = I_{o,STC}(\frac{T_{STC}}{T})^3 \exp\left[\frac{q \cdot E_g}{a \cdot k}(\frac{1}{T_{STC}} - \frac{1}{T})\right] \tag{2.5}$$

where E_g is the band gap energy of the semiconductor.

2.1.2 MPPT Control

Figure 2.2 shows how the electrical characteristics of a typical PV module are affected by the cell temperature and the solar irradiance. These curves can be derived from the above-mentioned mathematical equations or from field experiments; PV module manufacturers also often provide them. It could be observed that under different circumstances (i.e., cell temperature and solar irradiance), the PV system can operate at various but unique maximum power points (MPPs): the knees of those P-V curves. The PV module terminal current at MPP is almost directly proportional to the solar irradiance. However, an increase in the cell temperature causes a slight reduction in the PV module terminal voltage at MPP, and thereby leads to a lower power output at the same solar irradiation level. As the meteorological conditions may change throughout the course of a day, so does the MPP. Hence, it is important to maintain the PV system operating at its MPP regardless of the varying environmental conditions. The control techniques that maximize the PV power outputs are thus referred to as maximum power point tracking (MPPT). The core of MPPT techniques are impedance matching based on the maximum power transfer theorem. The equivalent impedance of a PV source can be considered as the

ratio between the voltage and the current at MPP. To maximize the power withdrawal from a PV system, its load characteristics need to be adjusted such that the equivalent load impedance matches the PV's.

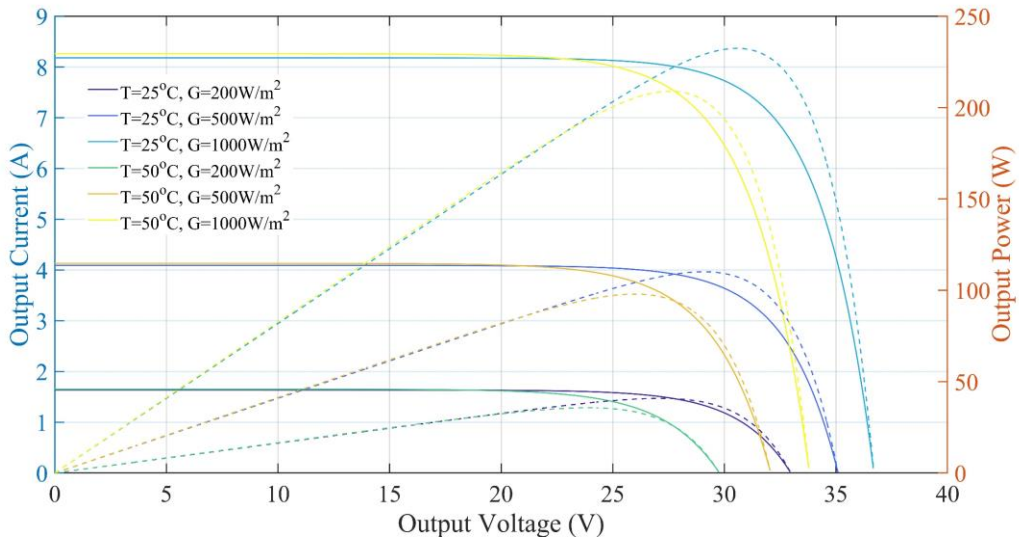

Figure 2.2. I-V and *P-V* Characteristics curves of a typical PV module.

Reference [101] conducted a comprehensive review of the existing MPPT methods, where those algorithms were compared in terms of tracking speed, algorithm complexity, dynamic tracking under partial shading, and hardware implementation. In comparison with the soft computing approaches, the traditional extremum-seeking algorithms such as the perturb and observe (P&O) and the incremental conductance (IC) have lower computational complexity at the cost of reduced tracking accuracy. Given the fact that each *P-V* curve normally has a unique MPP as shown in Figure 2.3, both P&O and IC aim to find the point where $\frac{dP_{pv}}{dv_{pv}}$ equals 0. However, P&O approximates dP_{pv} based on the

difference between the PV powers sampled in two consecutive time steps, which has limited accuracy and tracking performance. Alternatively, IC approximates dP_{pv} using the total derivative.

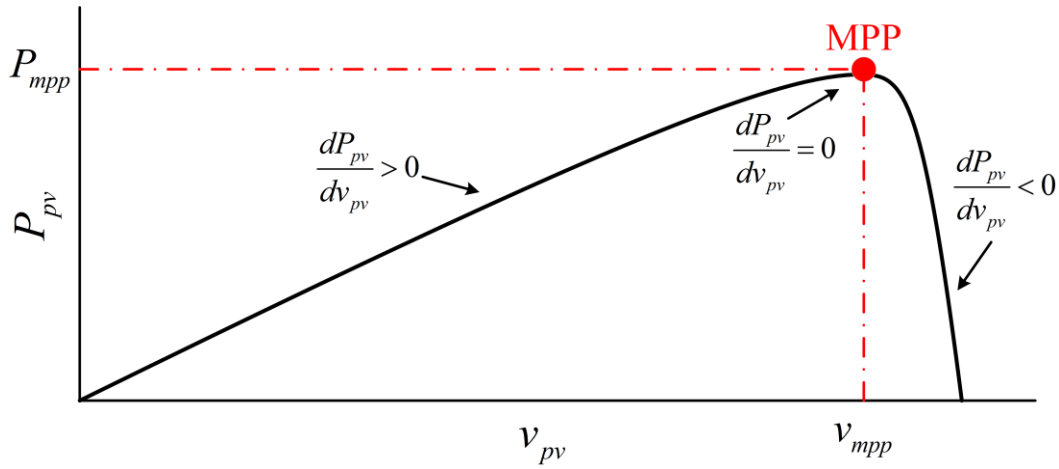

Figure 2.3. Slopes of the *P-V* characteristic curve.

The main idea is briefly illustrated here. The instantaneous PV power output is

$$P_{pv} = v_{pv} i_{pv} \tag{2.6}$$

Differentiating both sides with respect to v_{pv} yields

$$\frac{dP_{pv}}{dv_{pv}} = i_{pv} + v_{pv} \frac{di_{pv}}{dv_{pv}} \tag{2.7}$$

When $\frac{dP_{pv}}{dV_{pv}} = 0$, the operating point should satisfy the following *V-I* relationship:

$$\frac{di_{pv}}{dv_{pv}} = -\frac{i_{pv}}{v_{pv}} \tag{2.8}$$

In practice, $\frac{\Delta i_{pv}}{\Delta v_{pv}}$ is used to approximate $\frac{di_{pv}}{dv_{pv}}$. The logic behind IC is presented as below:

$$\begin{aligned} &\frac{\Delta i_{pv}}{\Delta v_{pv}} > -\frac{i_{pv}}{v_{pv}} && \text{on the left side of the MPP} \\ &\frac{\Delta i_{pv}}{\Delta v_{pv}} = -\frac{i_{pv}}{v_{pv}} && \text{at the MPP} \\ &\frac{\Delta i_{pv}}{\Delta v_{pv}} < -\frac{i_{pv}}{v_{pv}} && \text{on the right side of the MPP} \end{aligned} \tag{2.9}$$

At each time step, v_{pv} is adjusted by a fixed voltage increment or decrement to generate the voltage reference for the next time step. This process continues until the difference of the measured v_{pv} between two consecutive time steps, i.e., Δv_{pv}, becomes close to zero.

2.2 Modeling and Control of Grid-Connected PV-BESS Systems

PV systems alone would not be able to operate at night or on cloudy days. Paring with battery energy storage systems (BESSs) can add more power control flexibility to the PV systems. They can smooth out the potential fluctuations in solar power output. In addition, a BESS might be an economically viable option since it stores excess solar power on-site and can choose to sell electricity to the main grid or consume locally.

A conceptual illustration of a grid-connected PV-BESS system is presented in Figure 2.4. In the front end of this double-stage configuration, the PV array is operated in MPPT mode via a DC-DC boost converter, while the BESS is connected in parallel to the

DC link via a synchronous buck converter. Regulation of the DC-link voltage v_{dc} at a constant is necessary to maintain a dynamic balance between the DC input power and the AC output power. In the rear end, the inverter delivers the extracted maximum DC power from the PV system to the AC grid. The corresponding control loops are elaborated as follows.

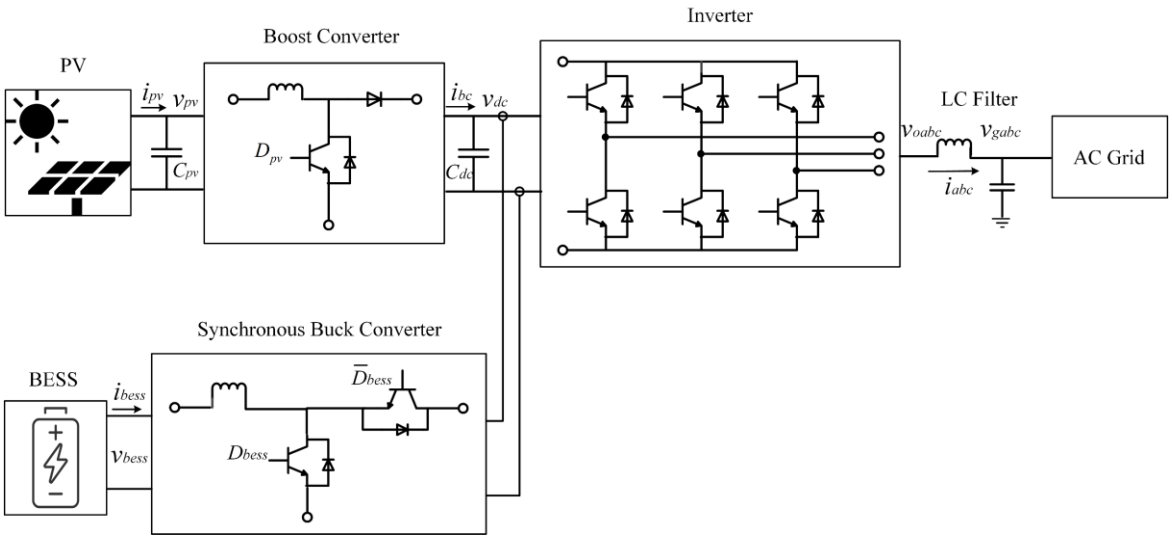

Figure 2.4. Diagram of PV-BESS system connected to a grid.

2.2.1 PV MPPT Control

Figure 2.5 shows the implemented MPPT closed-loop feedback control for the PV array. The MPPT algorithm takes in the PV voltage and current measurements filtered by low-pass filters (LPFs) and calculates the voltage reference v_{mpp} with the help of the boost converter. Then the voltage error is fed to the proportional-integral (PI) -based MPPT controller which generates the duty cycle through pulse-width modulation (PWM) for the boost converter [102].

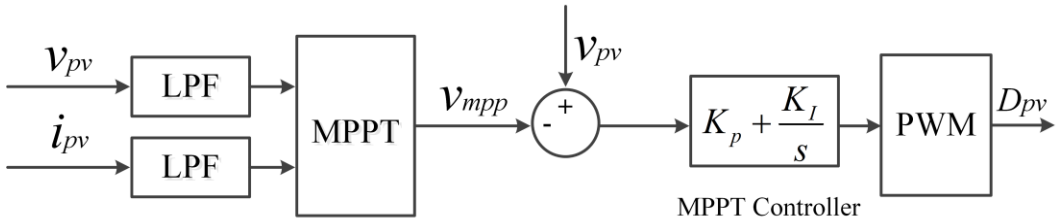

Figure 2.5. MPPT control loop.

2.2.2 BESS Control

In general, BESSs are utilized to stabilize the DC-link voltage of the PV-BESS system. Since the inverter can also perform this function, only a simple BESS current control loop is implemented to absorb and release stored energy, as shown in Figure 2.6. P^*_{bess} denotes a discharging power command if it is positive, and thus the synchronous buck converter works in the boost mode. When P^*_{bess} is negative, the BESS is charged by absorbing power via the DC link. The PI-based BESS controller acts on the BESS current error and generates a duty cycle D_{bess} for the synchronous buck converter.

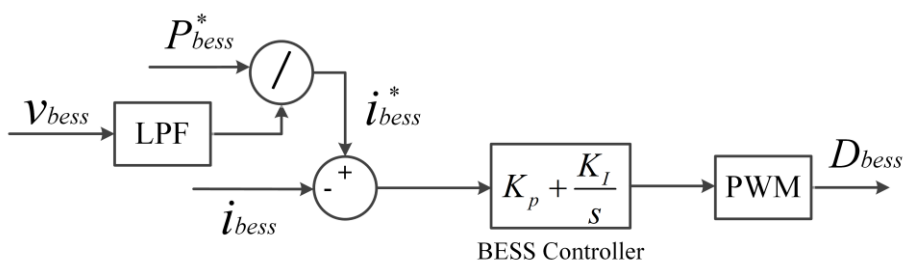

Figure 2.6. BESS control loop.

An important criterion for limiting the BESS charging and discharging capacities

is the range of the state of charge (SoC). In case the BESS reaches its lower bound of SoC, it must stop discharging so that no power should be pumped out of the battery. Likewise, if the BESS reaches its higher bound of SoC, it should not be charged further. In both cases, the BESS control is blocked simply by switching D_{bess} and its complement $\overline{D}_{bess}$ to zero. A simple logic module for deactivation (and activation) of BESS control is implemented.

2.2.3 Inverter Control

The inverter control is implemented through a dual control loop. The outer control loop deals with DC-link voltage control and/or power control, while the inner control loop is responsible for current regulation. Figure 2.7 presents the outer control loop.

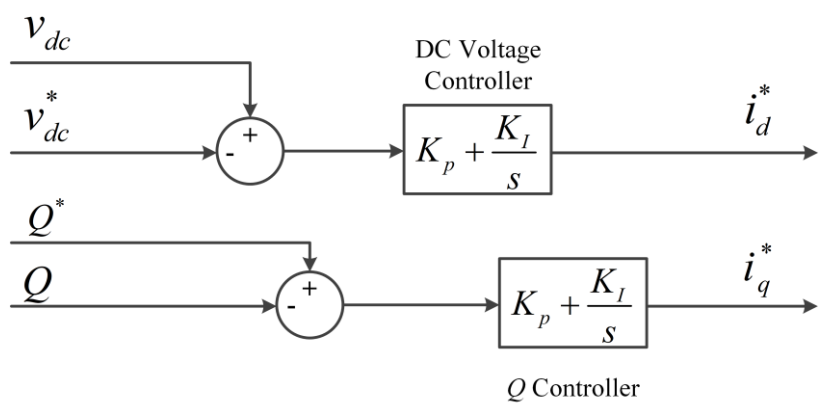

Figure 2.7. Outer control loop.

After the Park transformation is applied, the three-phase AC variables (*abc*) are converted to two orthogonal DC variables (*d*-*q*), which facilitates the use of PI controllers. Furthermore, the inverter instantaneous active power and reactive power on the grid side can be calculated based on the instantaneous power theory [103]:

$$\begin{cases} P_g = v_{gd} i_d + v_{gq} i_q \\ Q_g = v_{gq} i_d - v_{gd} i_q \end{cases} \tag{2.10}$$

Since the d-axis of the synchronous rotating reference frame is aligned with the grid voltage via a PLL that extracts the grid phase angle (θ), $v_{gd} = V_{gm}$ (V_{gm} is the magnitude of the grid phase voltage) and $v_{gq} = 0$. In terms of the DC link, the DC input power and the AC output power should be equal under the assumption that the inverter is lossless:

$$v_{dc} i_{dc} - v_{dc} C_{dc} \frac{dv_{dc}}{dt} = V_{gm} i_d \tag{2.11}$$

In the Laplace domain,

$$v_{dc}(s) \approx -\frac{V_{gm}}{V_{dc} C_{dc} s} i_d(s) + \frac{1}{C_{dc} s} i_{dc}(s) \tag{2.12}$$

where V_{dc} is the average DC-link voltage and $i_{dc}(s)$ can be considered as a disturbance. From this relationship, the DC-link voltage control can be designed using a PI controller, as shown in Figure 2.7. The average DC-link voltage is thus controlled at the reference v_{dc}^*, which is usually the nominal value. Meanwhile, reactive power closed-loop control is also implemented. If the unity power factor is desired, the power reference Q^* is set to zero.

After the outer control loop generates the current commands i_d^* and i_q^*, the inner current controllers should track these references, as shown in Figure 2.8.

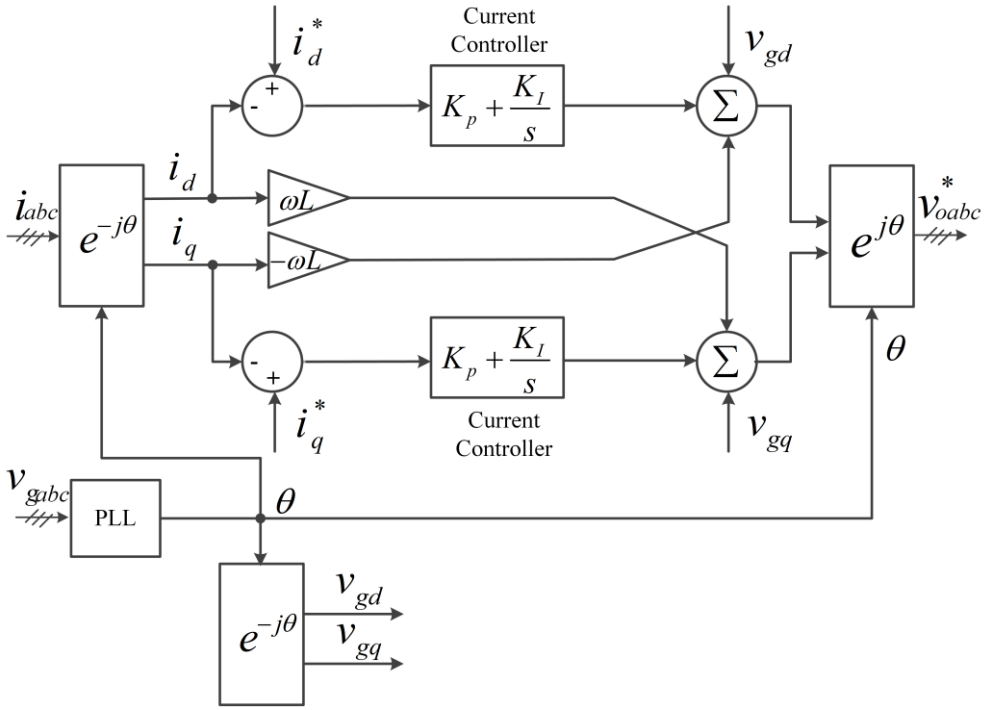

Figure 2.8. Inner control loop.

For the three-phase inverter shown in Figure 2.4, the relationship between the inverter output voltage v_{oabc} before the LC filter and the grid voltage v_{gabc} can be expressed as

$$\begin{bmatrix} \frac{di_a}{dt} \\ \frac{di_b}{dt} \\ \frac{di_c}{dt} \end{bmatrix} = \begin{bmatrix} -\frac{r}{L} & 0 & 0 \\ 0 & -\frac{r}{L} & 0 \\ 0 & 0 & -\frac{r}{L} \end{bmatrix} \begin{bmatrix} i_a \\ i_b \\ i_c \end{bmatrix} + \frac{1}{L} \begin{bmatrix} v_{oa} - v_{ga} \\ v_{ob} - v_{gb} \\ v_{oc} - v_{gc} \end{bmatrix} \tag{2.13}$$

where r and L are the equivalent series resistance and the inductance of the per-phase LC filter.

Application of the Park transformation to the above equations using θ from the PLL

module yields DC quantities in the synchronous rotating *d-q* reference frame:

$$\begin{cases} v_{od} = L\dfrac{di_d}{dt} + ri_d - \omega Li_q + v_{gd} \\ v_{oq} = L\dfrac{di_q}{dt} + ri_q - \omega Li_d + v_{gq} \end{cases} \tag{2.14}$$

It should be noted that these voltage equations are interdependent due to the cross-coupling terms ωLi_q and ωLi_d. Moreover, the grid voltage also has an impact on the control dynamics. Thus, one feed-forward term and one decoupling term are added to each PI controller for improved dynamic responses. The generated voltage reference is transformed as v_{oabc}^* using the inverse Park transformation, which is the input to a sinusoidal PWM module. The detailed inner control diagram is displayed in Figure 2.8.

2.2.4 Case Studies

Numerical simulations for the proposed grid-connected PV-BESS system in Fig. 2.4 are conducted in PSCAD. Since the rated output voltage of the simulated three-phase inverter is 4.16/2.4 kV, the DC-link voltage is designed as 10 kV for the inverter. Furthermore, the simulated PV array is rated 1 MW and comprised of STP 345S-24 PV modules. To meet the power and voltage requirements, 86 PV modules are connected in series per string and 34 strings in parallel. IC is selected as the MPPT algorithm, and the PV array is operated at unit power factor. The AC main grid is represented by an ideal voltage source, rated at 13.8/7.97 kV. Therefore, a wye-wye transformer is employed to match the voltages and provide galvanic isolation. The BESS is configured as two strings and each string contains 100 V-LFP48100 battery modules, amounting to 1.024 MWh and 5.12 kV. Since the 100 V-LFP48100 battery module has a C-rate of 0.2 at 25 °C, the

nominal power of the BESS is 0.2048 MW. In the simulations, the upper and lower SoC bounds of the BESS are set as 0.85 and 0.2 respectively. In addition, switching models of power converters are utilized to account for the inevitable harmonics in practice. The switching frequencies are set as 10 kHz for the boost converter and 5 kHz for the synchronous buck converter. At the start of the following simulations (i.e., before 0.2 sec), the DC-link capacitor is pre-charged by a paralleled 10-kV DC voltage source to avoid large power transients. The BESS control is activated at t = 1 sec.

2.2.4.1 Performance of the PV-BESS System When Charging. The BESS's SoC is set as 0.849 at the beginning of the simulation, while the solar radiation is initially 1000 W/m^2 and the cell temperature is 25 °C. Solar radiation rises to 1500 W/m^2 at t = 4.33 sec while the temperature is kept constant. Figure 2.9 illustrates the active and reactive power outputs of the inverter in an 8-sec simulation. The PV array puts out around 1 MW before the BESS starts to work in the charging mode at t = 1 sec. The charging power command to the synchronous buck converter is set as 0.1 MW to protect the BESS from high currents.

Since the SoC of the BESS reaches its upper limit of 0.85 at t = 5 sec as shown in Figure 2.10, the BESS control loop is deactivated afterwards, and all the active power generated by the PV array is delivered to the main grid. Figure 2.11 displays the three-phase inverter output voltages beyond the LC filter, while the frequency measured near the LC filter is given in Figure 2.12. The PV-BESS system has fast dynamic responses and low ripples in its outputs.

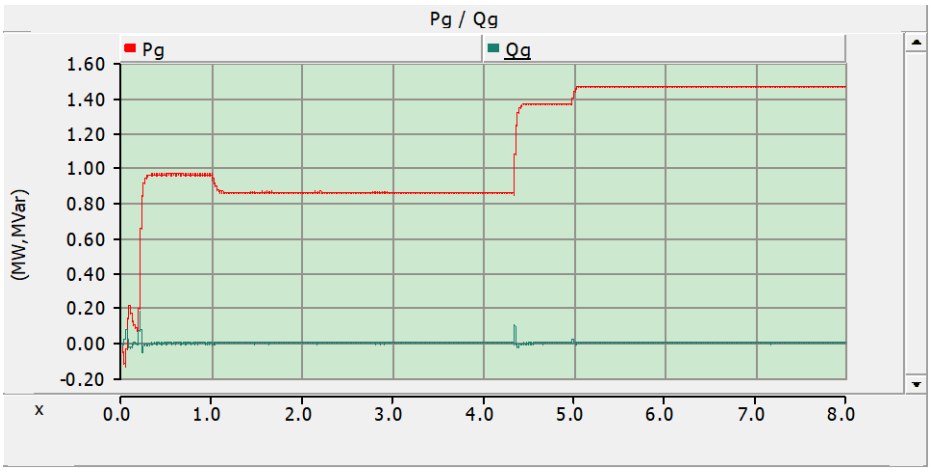

Figure 2.9. Inverter power outputs.

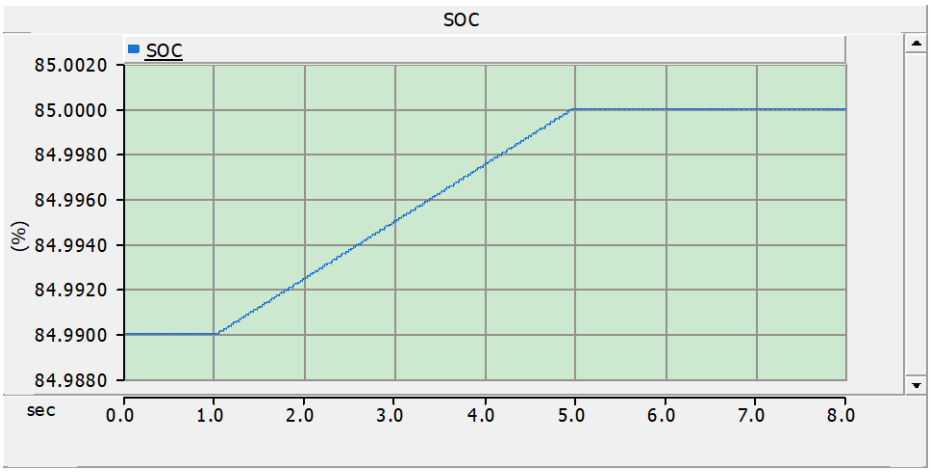

Figure 2.10. SoC of the BESS.

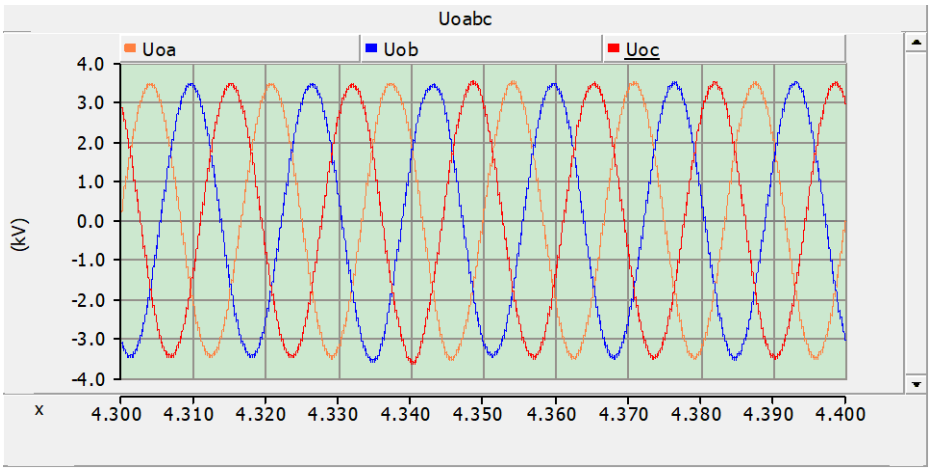

Figure 2.11. Zoomed-in view of the three-phase voltages beyond the LC filter.

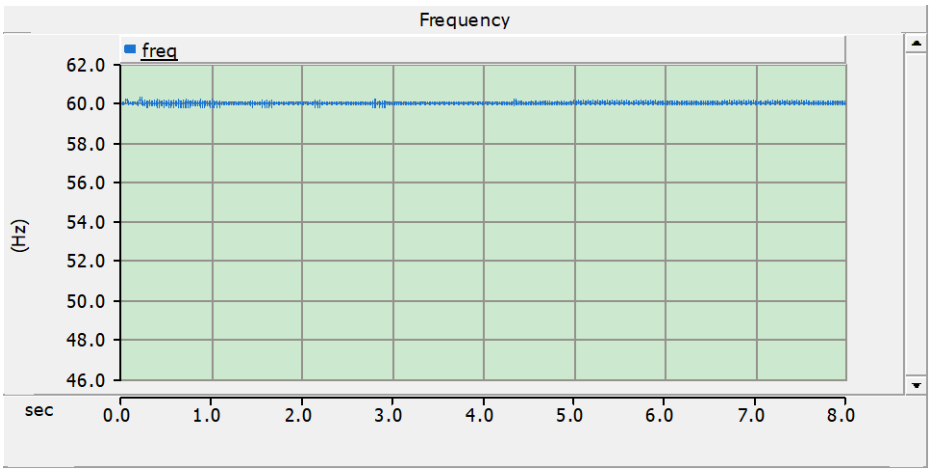

Figure 2.12. System frequency.

2.2.4.2 Performance of the PV-BESS System When Discharging. The dynamic performance of this grid-connected PV-BESS system during the discharging process is also of interest. This case considers a decrease in solar radiation in that it has a greater impact on the PV system's power output than the temperature. The operating temperature remains as 25 °C, while the solar irradiance is initially set as 1500 W/m^2. The SoC of the BESS is

pre-set at 0.8. At t = 1 sec, the BESS control starts to operate the synchronous buck converter in the charging mode because of sufficient solar power generation. Nevertheless, the solar radiation decreases to 833 W/m^2 at t = 1.68 sec when the cloud cover occurs. Then the BESS is controlled to feed the scheduled 0.1 MW to the main grid. The active and reactive powers fed into the AC grid are shown in Figure 2.13. It is worth noting that reactive power output is kept almost as zero due to good decoupling from active power. This dynamic process is also illustrated by the SoC curve in Figure 2.14.

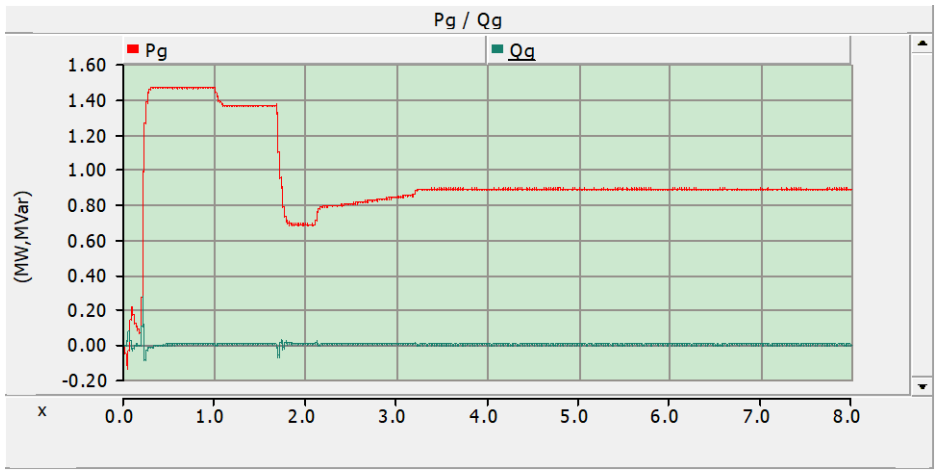

Figure 2.13. Inverter power outputs.

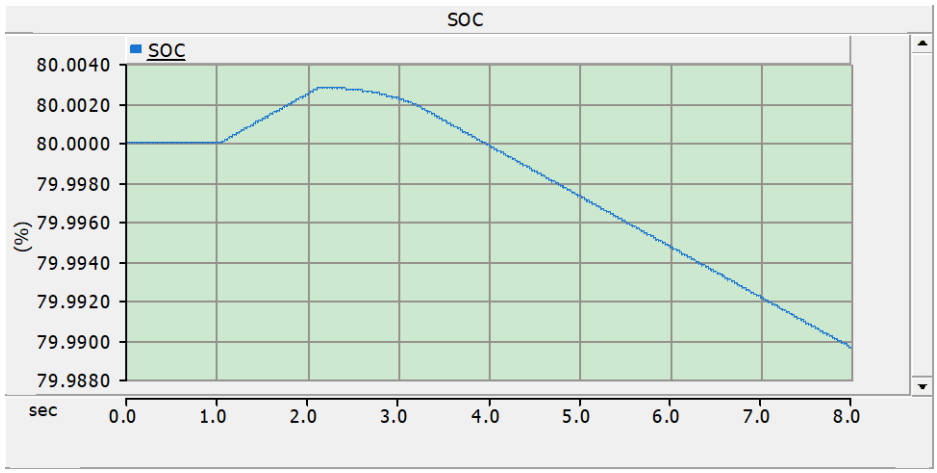

Figure 2.14. SoC of the BESS.

In Figure 2.15, it is observed that the three-phase output voltages of the inverter are almost sinusoidal with low harmonic content. Additionally, the frequency measured near the LC filter oscillates around 60 Hz with very small ripples, shown in Figure 2.16. The frequency support is completely dependent on the external AC grid, the same as in the case shown in Section 2.2.4.1..

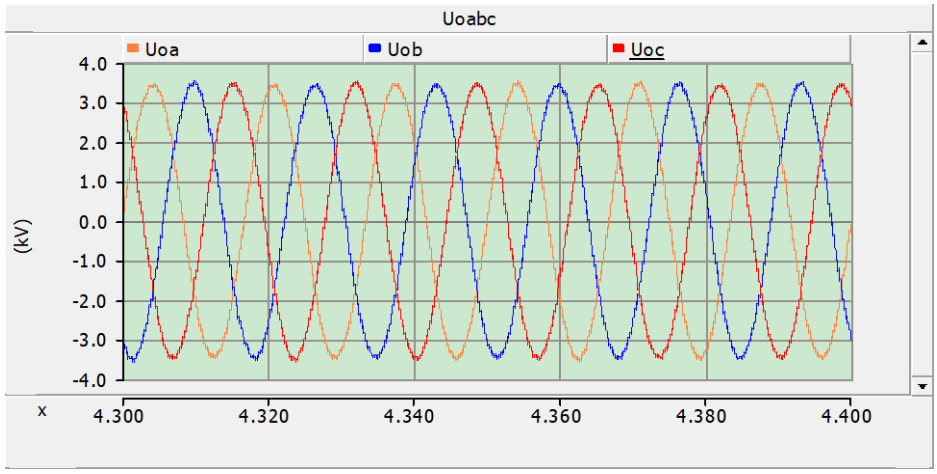

Figure 2.15. Zoomed-in view of the three-phase voltages beyond the LC filter.

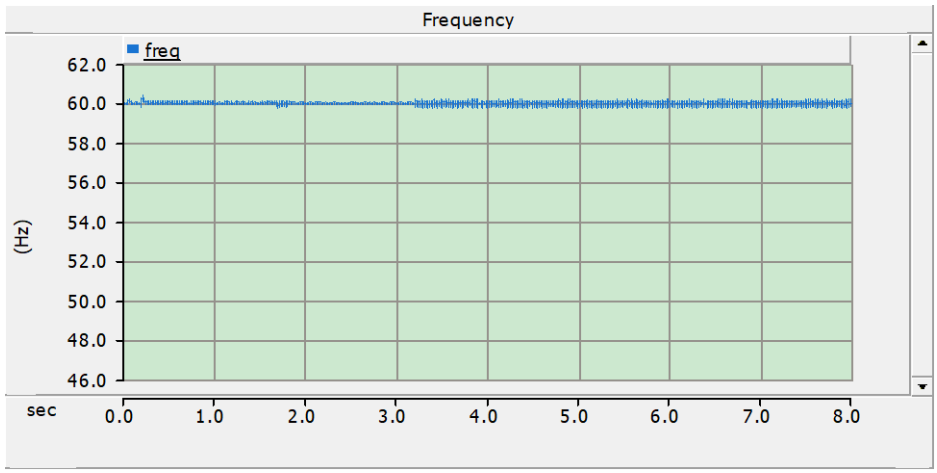

Figure 2.16. System frequency.

2.3 PV-VSG Modeling and Control

VSG technologies provide a promising solution for integrating power-electronics-converter-based RESs into the power systems with improved frequency and voltage stabilities, as the proportion of RESs continues to rise. The VSG mimics the dynamic characteristics of conventional SGs. Figure 2.17 shows a typical SG regulated by excitation and governor control systems. The speed governor varies prime mover output (torque or power) automatically for changes in system speed (frequency). Typical prime movers are diesel engines, gasoline engines, steam turbines, hydro-turbines, and gas turbines [104]. The excitation system provides the necessary field current to the SG's rotor winding and regulates the SG's stator terminal voltage.

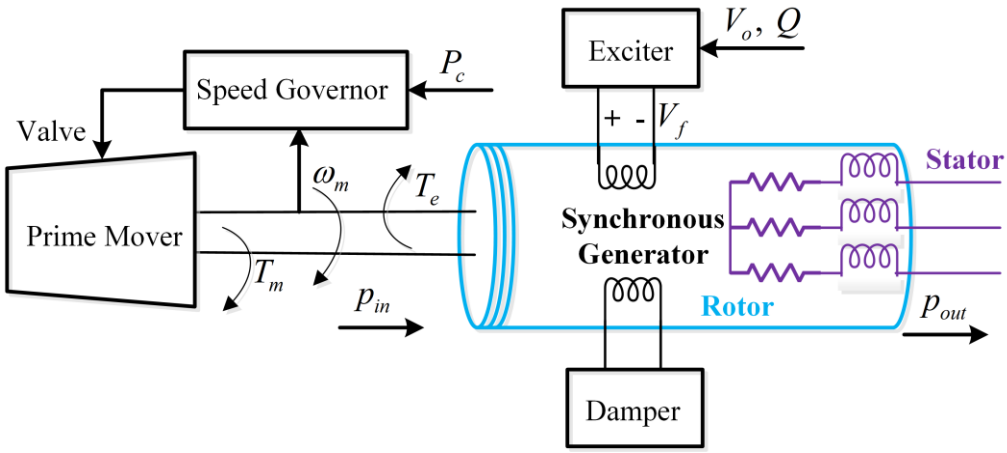

Figure 2.17. Schematic diagram of a SG and its control systems.

The swing equation of the SG based on rotor motion equation [105] is:

$$J\omega_m\dot{\omega}_m + D_d(\omega_m - \omega_s) = p_{in} - p_{out} \tag{2.15}$$

where J is the combined moment of inertia of the prime mover and SG rotor, ω_m is the rotor shaft velocity, and ω_s is the rotor synchronous speed. p_{in} is net shaft power input to the SG, while p_{out} is the electrical air-gap power corresponding to the counteracting electromagnetic torque T_e. D_d denotes the damping coefficient that accounts for the effect of damper winding. More specifically,

$$p_{in} = P_c - R_D(\omega_m - \omega_s) \tag{2.16}$$

where R_D is the speed droop and P_c is a control input to the speed governor, which can either be a constant or the output of automatic generation control (AGC) [104]. Since p_{in} is generated by the speed governor and prime mover which generally have a relatively large time constant, it reacts only to the frequency swings in the range of 0.3-3 Hz [106]. In

contrast, $J\omega_m\dot{\omega}_m$ is due to the inertia and responds to faster frequency swings, normally in the range of 3-30 Hz.

To emulate the electromechanical behaviors of the above SG system, a double-stage PV-VSG model is proposed. Figure 2.18 illustrates the topology and control diagram of the proposed PV-VSG. The front-end DC-DC boost converter is controlled to mimic the prime mover of a conventional SG, while the rear-end DC-AC inverter is controlled to mimic the SG. In the following subsections, the control modules relevant to the two stages are elaborated respectively.

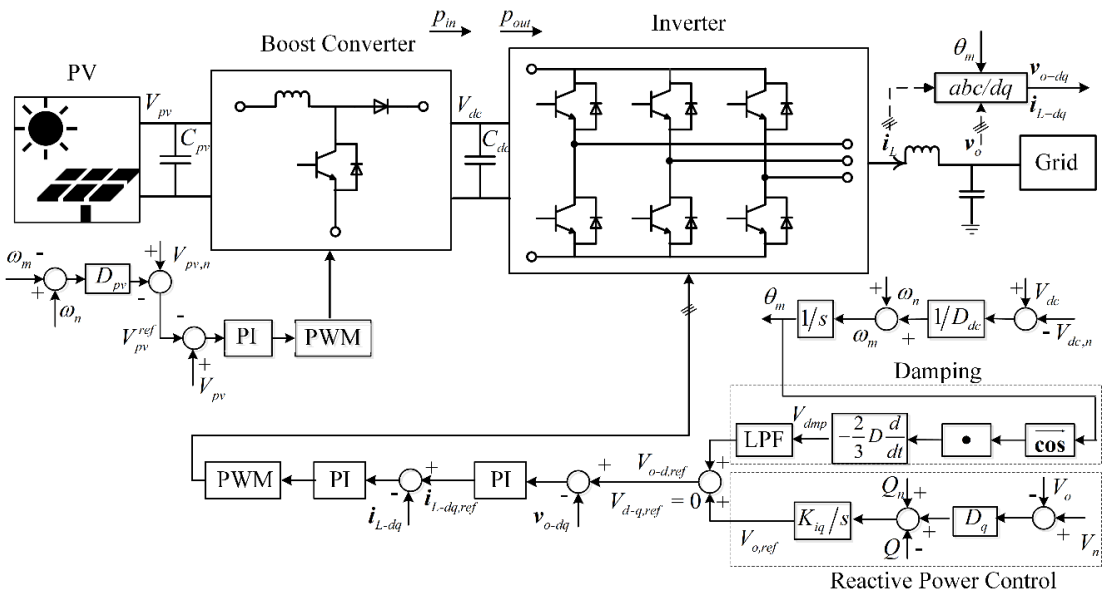

Figure 2.18. Control diagram of the proposed PV-VSG.

2.3.1 Front-End Control

To avoid over-modulation of the boost converter, the PV array is operated on the right side of the MPP based on the *P-V* characteristic curve which can be estimated via the

measured solar irradiance and PV cell temperature [107]. Thus, the following equation is introduced to resemble (2.16):

$$V_{pv}^{ref} = V_{pv,n} - D_{pv}(\omega_n - \omega_m) \tag{2.17}$$

where $V_{pv,n}$ matches the desired active power reserve (corresponding to P_c in Figure 2.17) to provide the speed governor and prime mover response, and D_{pv} is the droop coefficient. These two parameters can be readily determined from the estimated *P-V* characteristics curve. In addition, D_{pv} and $V_{pv,n}$ are periodically updated to keep track of the PV system's real-time operating conditions. ω_n is the nominal angular frequency, and ω_m is the virtual angular frequency generated in the rear end that will be introduced later. A PI controller is designed with a large time constant to mimic the slow response of the speed governor and prime mover. The duty cycle of the boost converter is adjusted via the PI controller so that V_{pv} closely tracks V_{pv}^{ref}. This negative feedback mechanism automatically balances the load if the available solar power is sufficient for active power reserve.

2.3.2 Rear-End Control

An analogy can be made between the combined moment of inertia J and the DC-link capacitor C_{dc} of the inverter in terms of power. If the damping effect is ignored for the time being, the swing equation is written as follows:

$$p_{in} - p_{out} = J\omega_m\dot{\omega}_m = C_{dc}V_{dc}\dot{V}_{dc} \tag{2.18}$$

Furthermore, a linear mapping is adopted between the DC-link voltage V_{dc} and ω_m:

$$\omega_m = \omega_n + \frac{1}{D_{dc}}(V_{dc} - V_{dc,n}) \tag{2.19}$$

where $V_{dc,n}$ is the nominal DC-link voltage, and D_{dc} is the droop coefficient.

Taking derivative of both sides of (2.19) and comparing with (2.18) yields

$$J = D_{dc}\frac{V_{dc,n}}{\omega_n}C_{dc} \tag{2.20}$$

Thus, proper selection of D_{dc} is permitted given a desired J. Moreover, this relationship indicates that J can be augmented when only a limited capacitance is available.

The reactive power controller in Figure 2.18 is similar to the automatic voltage regulator (AVR) [105] plus a reactive power-voltage droop controller. The reference output voltage magnitude is obtained by integration:

$$V_{o,ref} = K_{iq}\int\left[Q_n + D_q(V_n - V_o) - Q\right]dt \tag{2.21}$$

where Q and V_o are the measured/calculated output reactive power and the output voltage magnitude at the LC filter. Q_n and V_n are their nominal values; D_q is a droop coefficient, which is designed following [108].

As for the damping term in (2.15), it is not straightforward to apply since J has been represented by C. Alternatively, the damping method proposed in [109] is adopted. This method can flexibly improve the damping of responses without compromising the desired inertial response. Define $\overrightarrow{\mathbf{sin}}(\theta) := \left[\sin(\theta) \quad \sin\left(\theta - \frac{2\pi}{3}\right) \quad \sin\left(\theta + \frac{2\pi}{3}\right)\right]$ and $\overrightarrow{\mathbf{cos}}(\theta) := \left[\cos(\theta) \quad \cos\left(\theta - \frac{2\pi}{3}\right) \quad \cos\left(\theta + \frac{2\pi}{3}\right)\right]$. Assuming the actual output voltage

$\boldsymbol{v}_o = V_o\,\overrightarrow{\mathbf{sin}}(\theta_o)$, the derivative of the inner product readily yields the difference between ω_o and ω_m:

$$\frac{d}{dt}(\langle \boldsymbol{v}_o, \overrightarrow{\boldsymbol{cos}}(\theta_m)\rangle) = \frac{3}{2}V_o(\omega_o - \omega_m)cos(\theta_o - \theta_m) \tag{2.22}$$

Therefore, the damping term $V_{dmp} = -\frac{2}{3}D\frac{d}{dt}(\langle \boldsymbol{v}_o, \overrightarrow{\boldsymbol{cos}}(\theta_m)\rangle)$ is added to $V_{o,ref}$ to generate the modified reference voltage magnitude $V_{o-d,ref}$; D is the corresponding damping coefficient. A low-pass filter (LPF) is also employed because the derivative operation can amplify high-frequency noises. The inverter reference voltage is then generated via two sets of cascaded PI controllers working in the synchronous rotating *d-q* reference frame, which form the outer voltage control loop and the inner current control loop.

2.4 Coordinated Control of PV-VSG and CHP

The solar PV system can operate alone when the solar irradiance is sufficient, while the CHP unit provides frequency-responsive spinning reserves for the solar PV.

2.4.1 CHP Modeling and Control of the CHP Unit

Figure 2.19 displays a typical single-shaft GT-based CHP unit with its major components: a compressor, a combustor, and an expansion turbine (ET). The heated flow expanded in the ET drives the compressor and the generator (G), while the heat recovery steam generator (HRSG) recovers waste heat from the exhaust gases. The steam produced by the HRSG can be used for heating/cooling or to drive a steam turbine.

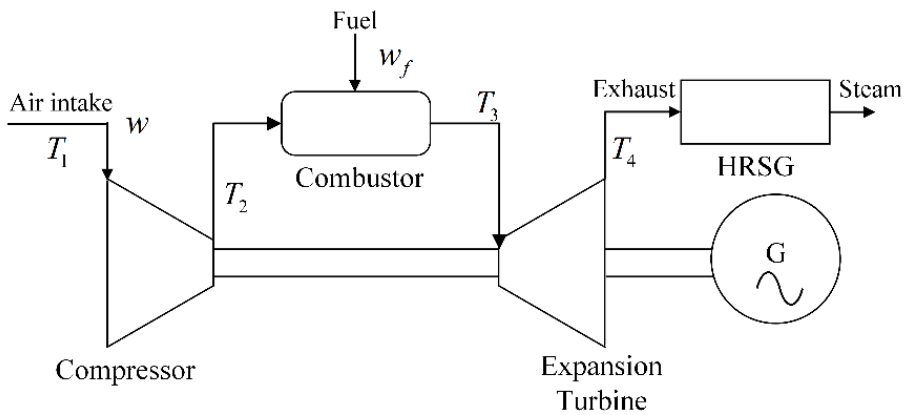

Figure 2.19. Single-shaft GT-based CHP unit.

2.4.1.1 Gas Turbine Thermodynamics. In essence, all GTs are based on the Brayton cycle [30]. The temperature-entropy diagram of the Brayton cycle is illustrated in Figure 2.20.

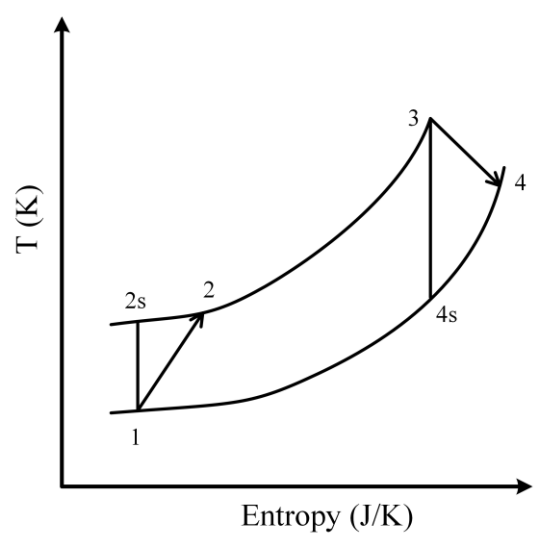

Figure 2.20. Brayton cycle temperature-entropy diagram.

Ambient air comes into contact with the compressor at Point 1 and is then

compressed in an irreversible process to Point 2. Input heat in the combustor increases the temperature to point 3 where the combustion product and compressor discharge air enter the ET and expand to Point 4. For simplicity, the processes 2-3 and 4-1 are assumed to be isobaric. While the processes in the compressor (i.e., 1-2) and the ET (i.e., 3-4) are irreversible and non-isentropic, they are assumed to be isentropic as 1-2s and 3-4s in order to approximate the compressor and ET irreversible adiabatic efficiencies η_c and η_t, respectively:

$$\eta_c = \frac{h_{2s} - h_1}{h_2 - h_1} \approx \frac{T_{2s} - T_1}{T_2 - T_1} \tag{2.23}$$

$$\eta_t = \frac{h_3 - h_4}{h_3 - h_{4s}} \approx \frac{T_3 - T_4}{T_3 - T_{4s}} \tag{2.24}$$

where h is the fluid mixture enthalpy (kJ/kg) and T is the absolute temperature in K.

Two intermediate variables are also defined:

$$x_c := \left(PR_n \cdot w_{pu}\right)^{\frac{\gamma_c - 1}{\gamma_c}} \tag{2.25}$$

$$x_h := \left(PR_n \cdot w_{pu}\right)^{\frac{\gamma_h - 1}{\gamma_h}} \tag{2.26}$$

where PR_n is the nominal compressor pressure ratio, and w_{pu} is the airflow rate (w) in per unit (pu). γ_c and γ_h are the cold-end and hot-end ratios of specific heats, respectively.

As an irreversible adiabatic process is assumed in the compressor, the compressor discharge temperature T_2 (K) can be calculated as:

$$T_2 = T_1\left(\frac{x_c - 1}{\eta_c} + 1\right) \tag{2.27}$$

where T_1 (K) is the ambient temperature.

Likewise, the ET exhaust temperature T_4 (K) is derived as:

$$T_4 = T_3\left[1 - \left(1 - \frac{1}{x_h}\right)\eta_t\right] \tag{2.28}$$

where T_3 (K) is the ET inlet temperature.

Assuming an isobaric process in the combustor and considering the heat absorption rate (kJ/s) lead to

$$T_3 = T_2 + \eta_{comb}\frac{H}{C_{ph}} \cdot \frac{w_{fn}}{w_n} \cdot \frac{w_{f,pu}}{w_{pu}} \tag{2.29}$$

where H is the lower heating value of the fuel, and η_{comb} is the combustor efficiency. w_{fn} and w_n are the nominal fuel flow and airflow rates (kg/s), respectively. C_{ph} stands for the specific heat of hot-end air at constant pressure.

It is also assumed that w_f is negligible compared with w [110]. The net mechanical power produced by the GT can be calculated as

$$P_{G,pu} = \frac{P_G}{P_{Gn}} = \frac{w_{pu} \cdot w_n \cdot \left[C_{ph} \cdot (T_3 - T_4) - C_{pc} \cdot (T_2 - T_1)\right]}{P_{Gn}} \tag{2.30}$$

where C_{pc} is the specific heat of cold-end air at constant pressure, and P_{Gn} is the nominal gross power output (kW).

Besides, the thermal power collected by the HRSG is

$$P_{ST,pu} = K \cdot w_{pu} \cdot w_n \cdot C_{ph} \cdot T_4 \tag{2.31}$$

where K is a system-specific constant coefficient.

2.4.1.2 Control Loops. The GT-based CHP dynamic model is proposed and simulated as shown in Figure 2.21. The speed governor (speed controller) is operated in standard droop mode for load sharing. It can also be in the isochronous mode to eliminate the error between the rotor speed ω_r and the speed reference ω_{ref}.

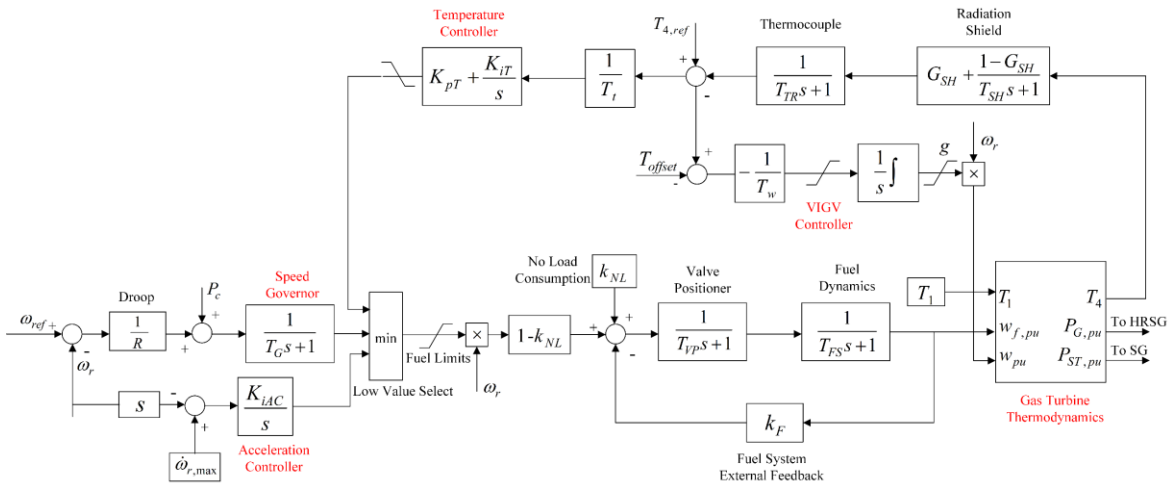

Figure 2.21. Dynamic model of the GT-based CHP.

The acceleration controller limits the acceleration of the generator rotor during the start up or for a sudden loss of load. This controller becomes secondary in normal operations. A PI-based temperature controller is employed to adjust the turbine temperature T_4 by reducing the fuel flow. If the measured T_4 exceeds the reference $T_{4,ref}$, the controller will come off the maximum limit and integrate down such that its output starts to act through the low value select block, whose output is $w_{f,pu}$. In practice, the position g of

variable inlet guide vanes (VIGVs) at the front of the compressor should be controlled to regulate the airflow drawn into the compressor when the GT is at part load or during start up. This way, T_4 can be maintained at an adequate level that benefits the downstream HRSG. In this dynamic model, T_4 is kept lower than $T_{4,ref}$ by considering an offset, e.g., 1% of the rated value. The VIGV controller modulates g, which in turn changes w_{pu} along with the rotor speed ω_r. The no-load consumption k_{NL} ensures satisfaction of the minimum fuel requirement for self-sustaining combustion, which is crucial for compressor operation. Also, the valve positioner and fuel system dynamics are approximated as first-order transfer functions. $k_F = 0$ if the GT operates on gas fuels.

2.4.2 Case Studies

To validate the effectiveness of the proposed PV-VSG and GT-based CHP models and demonstrate their coordinated control in an islanded campus microgrid, numerical simulations of a prototype campus microgrid as shown in Figure 2.22 are conducted in MATLAB/Simulink.

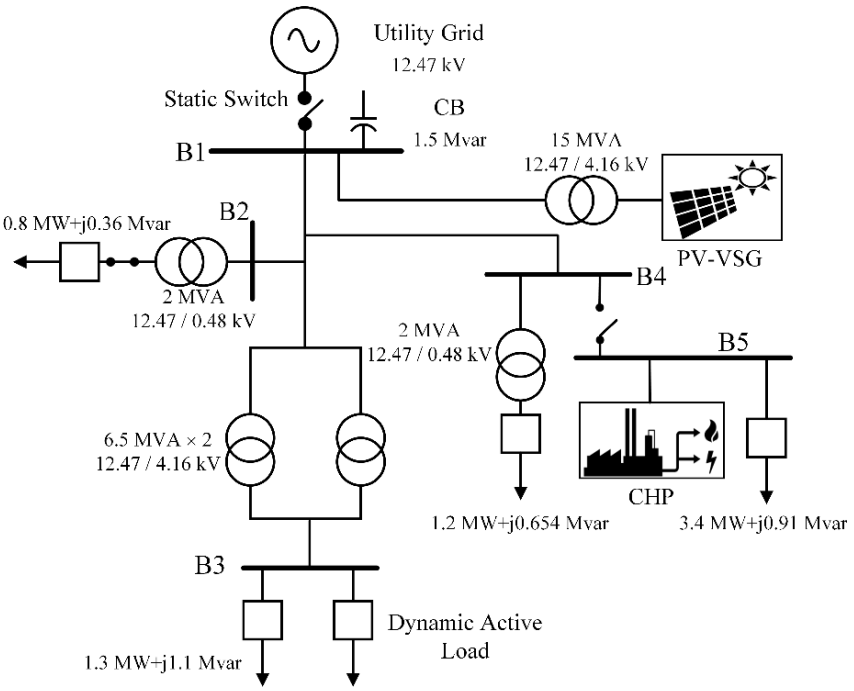

Figure 2.22. Single-line diagram of the simulated campus microgrid system.

During a utility power outage, the campus microgrid will operate in the islanded mode, i.e., the static switch at Bus 1 remains open. The capacitor bank (CB) is activated for reactive power support. During school days, the loads at Bus 4 and Bus 5 are identified as the critical loads, while the other loads are noncritical ones. It is also assumed that automatic underfrequency load shedding (UFLS) is in place. The 10-MW PV farm is controlled as a PV-VSG. The CHP module represents the 5-MVA Centaur 40 CHP model [111] and contains a salient-pole SG fitted with the generic IEEE DC1A exciter. Averaged models of the boost converter and the inverter are employed in the PV-VSG model for simulation speedup. The detailed control and system parameters are listed in Table 2.1.

Table 2.1

System and Control Parameters

Centaur 40 CHP Unit Parameters	Symbol	Value
Speed droop (pu)	R	0.04
Speed governor time constant (sec)	T_G	0.03
Acceleration controller gain	K_{iAC}	100
Maximum acceleration	$\dot{\omega}_{r,max}$	0.2
Fuel upper limit (pu)	$F_{d,max}$	1.5
Fuel lower limit (pu)	$F_{d,min}$	-0.13
No-load fuel consumption (pu)	k_{NL}	0.24
Valve positioner time constant (sec)	T_{VP}	0.04
Fuel system time constant (sec)	T_{FS}	0.18
Fuel system external feedback loop gain	k_F	0
Radiation shield gain	G_{SH}	0.85
Radiation shield time constant (sec)	T_{SH}	10.2
Thermocouple time constant (sec)	T_{TR}	1.2
Temperature controller constant (°C)	T_t	380
Temperature controller proportional	K_{pT}	3.4
Temperature controller integral	K_{iT}	1
Reference exhaust temperature (°C)	$T_{4,ref}$	465
VIGV controller constant (°C)	T_w	380
Gate position upper limit (pu)	g_{max}	1.0
Gate position lower limit (pu)	g_{min}	0.72

Centaur 40 CHP Unit Parameters	Symbol	Value
Nominal compressor pressure ratio	PR_n	10
Nominal airflow rate (kg/sec)	w_n	18.98
Nominal fuel flow rate (kg/sec)	w_{fn}	0.29
Hot-end ratio of specific heats	γ_h	1.33
Cold-end ratio of specific heats	γ_c	1.4
Specific heat of hot-end air at constant pressure (kJ/kg/K)	C_{ph}	1.1569
Specific heat of cold-end air at constant pressure (kJ/kg/K)	C_{pc}	1.0047
Compressor efficiency	η_c	0.86
Combustor efficiency	η_{comb}	0.99
Expansion turbine efficiency	η_t	0.89
Lower heating value of natural gas (kJ/kg)	H	47130
HRSG thermal power coefficient	K	0.0003
PV-VSG Parameters	**Symbol**	**Value**
DC-link nominal voltage (kV)	$V_{dc.n}$	10
Nominal angular frequency (rad/sec)	ω_n	377
DC-link capacitor (mF)	C_{dc}	30
Grid nominal voltage (line-to-line) (kV)	-	4.16
Inverter power rating (MVA)	-	10
Boost converter inductance (mH)	-	5
PV shunt capacitance (μF)	C_{pv}	500
LC filter inductance (mH)	-	5

Centaur 40 CHP Unit Parameters	Symbol	Value
LC filter capacitance (μF)	-	60
$\omega_m - V_{pv}$ droop	D_{pv}	67.4
$V_{dc} - \omega_m$ droop	D_{dc}	318
Damping coefficient	D	0.01
$V - Q$ droop	D_q	2944.2
Nominal reactive power (Mvar)	Q_n	1

The dynamic active load at Bus 3 is modeled to test the transient performance of the proposed PV-VSG under different loading conditions. Specifically, the dynamic active load experiences a step increase from 0 to 1.2 MW at t = 10.2 sec and then a step decrease to 0.8 MW at t = 18.7 sec. To further explore the effect of solar irradiance on the PV-VSG operation, a varying solar irradiance shown in Figure 2.23 is used throughout the simulation.

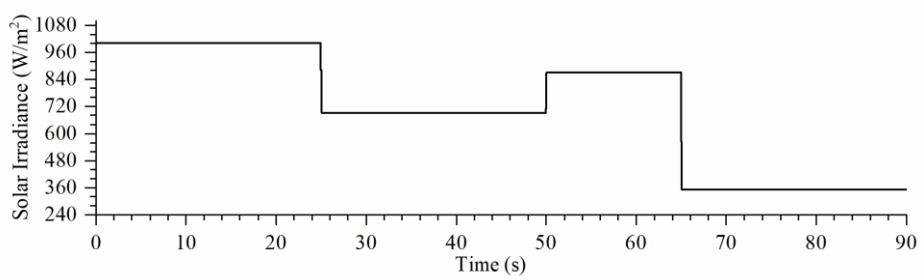

Figure 2.23. Solar irradiance curve.

In order to illustrate the coordinated control of the PV-VSG and the CHP, the simulation scenario is designed such that the CHP unit initially only supplies the local load

at Bus 5 and can enter the hot standby mode once dispatched. The rest of the campus is served by the PV farm with the assumption that the available solar power is initially adequate to provide active power reserve. However, since the grid frequency may drop due to plunged solar irradiance or increased campus loads, UFLS should prevent the frequency from falling below the minimum permissible value, e.g., 59.3 Hz. When the frequency stabilizes after some transients, the CHP unit will start to synchronize to deliver reliable power and also enhance system inertia. It should be noted that the design of a UFLS scheme is system-specific and beyond the scope of this paper. For simplification, the UFLS is set such that the load at Bus 2 will be shed when the system frequency reaches 59.7 Hz, and the dynamic active load will be shed once the frequency drops below 59.6 Hz. Other loads are shed in further steps when lower frequency thresholds are met. In addition, this protective relay setting is consistent before and after CHP synchronization. The ambient temperature is assumed to be 27.5 °C, and $V_{dc,n}$ is 10 kV. $V_{pv,n}$ is initially set as 5847 V, resulting in an active power reserve of around 5 MW. The total simulation time is 90 sec with a time step of 50 μs.

The DC-link voltage of PV-VSG and the angular frequencies of both DERs during the simulation are presented in Figure 2.24. As can be observed, with a constant solar irradiance in the first 25 seconds, the PV-VSG solely responds to the change in loads with a varied V_{dc}, which relates to a constantly identical waveform of ω_m due to the introduced linear transformation. It is also observed that a change in solar irradiance leads to a variation in V_{dc} and ω_m, e.g., at the transient right after t = 25 sec. However, the frequency does not change rapidly due to the inertia emulated by the capacitor. The CHP unit is called upon as hot standby at t = 20 sec. Pre-synchronization is initiated at t = 27.93 sec when

the system frequency stabilizes at 59.75 Hz after the solar irradiance decreases for the first time. CHP synchronizes to the rest of the grid at t = 31.06 sec for load sharing. Meanwhile, the governor speed reference ω_{ref} is adjusted from 1.008 pu to 1.014 pu and remains fixed afterwards. Owing to the CHP's participation in frequency regulation, the grid frequency recovers and settles at 59.928 Hz at t = 35.51 sec. As the solar irradiance goes up at t = 50 s, the PV power is adequate to supply the loads such that the DC-link capacitor is recharged, thus increasing both ω_m and V_{dc}. At t = 65 sec, the solar irradiance plummets from 870 to 350 W/m^2. The UFLS protective relays are automatically triggered at t = 65.37 sec and t = 65.69 sec to shed the load at Bus 2 and the dynamic active load, respectively. The grid frequency finally settles at 59.806 Hz (0.99677 pu).

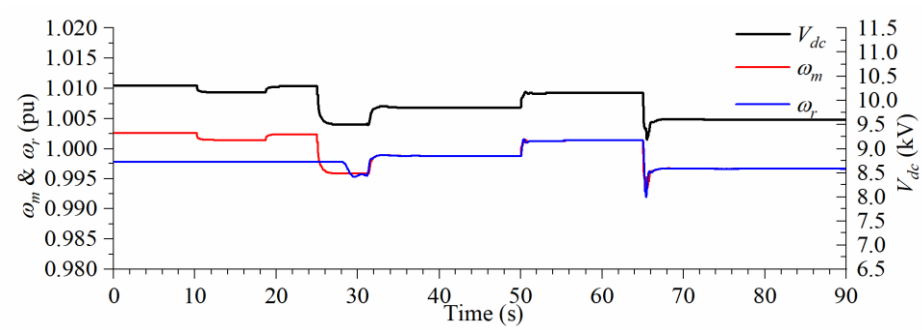

Figure 2.24. CHP and PV-VSG frequency responses and PV-VSG DC-link voltage.

Figure 2.25 displays the power outputs of the two DERs throughout the entire simulation. Before the CHP is synchronized, the PV-VSG is able to achieve automatic load balancing despite variations in the solar irradiance. This capability is ensured by sufficient active power reserve. After the CHP unit is synchronized to the microgrid, it begins to pick up part of the loads. Interestingly, the active power shared by the CHP and PV systems are

not in a fixed proportion at all times but affected by the varying solar irradiance. After the solar irradiance plunges at t = 65 sec, the CHP unit takes over too much active power and almost reaches its apparent power rating. Consequently, the reactive power capability of the CHP unit becomes very limited. It is also worth noting that the CHP unit alone cannot serve the entire electrical loads of the campus once the sun stops shining. Hence, uprating the existing CHP unit or installing additional CHP units would be favorable to the stable and reliable operation of the campus microgrid.

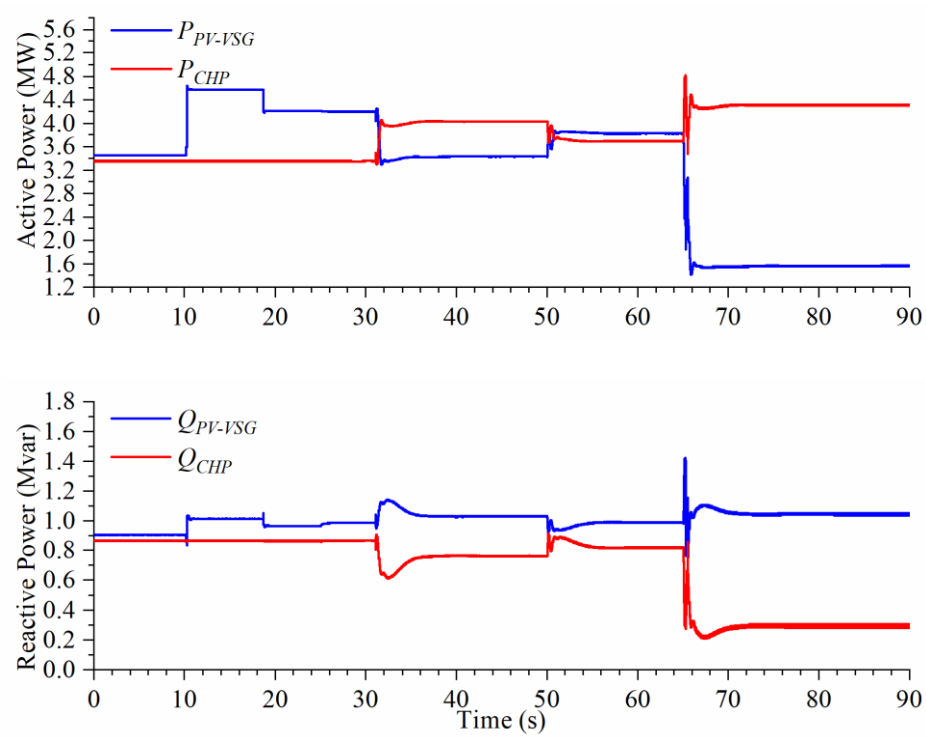

Figure 2.25. Active and reactive power outputs of CHP and PV-VSG.

The variables related to the thermodynamic equations of the CHP's gas turbine are illustrated in Figure 2.26.

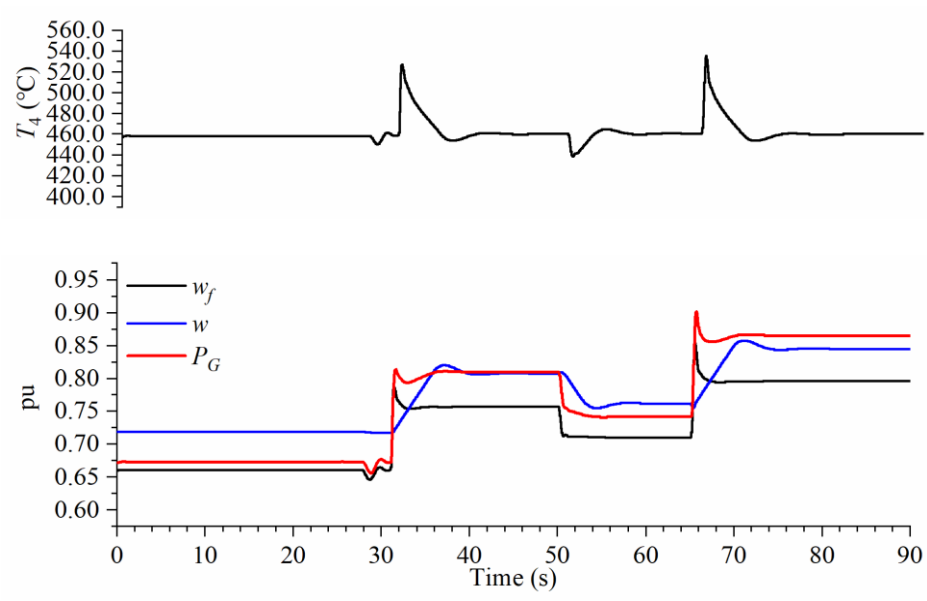

Figure 2.26. Illustration of the variables in the GT thermodynamic equations.

Prior to synchronization, the GT exhaust temperature is maintained close to the reference value 465 °C, albeit at part load. This is because the VIGV controller is in action, which regulates w to a relatively low level. Once the CHP is synchronized, the fuel flow rate rises so as to provide a higher mechanical power output. As T_4 surpasses the reference, w is controlled to reach a higher level so that T_4 is brought back near the reference again. It is also observed from Figure 2.26 that the temperature controller also acts by decreasing w_f, which is evidenced after the instants t = 31.06 sec and t = 65.69 sec. However, the VIGV control has a slower response than the fuel flow rate control. Besides, Figure 2.26 shows that the mechanical power output P_G varies almost linearly with w_f, which checks with the derived GT thermodynamic equations.

It has also been verified that the voltage magnitudes at all buses are maintained within the typical permissible bounds from 0.95 pu to 1.05 pu, when the campus microgrid

is in islanded mode as shown in Figure 2.27.

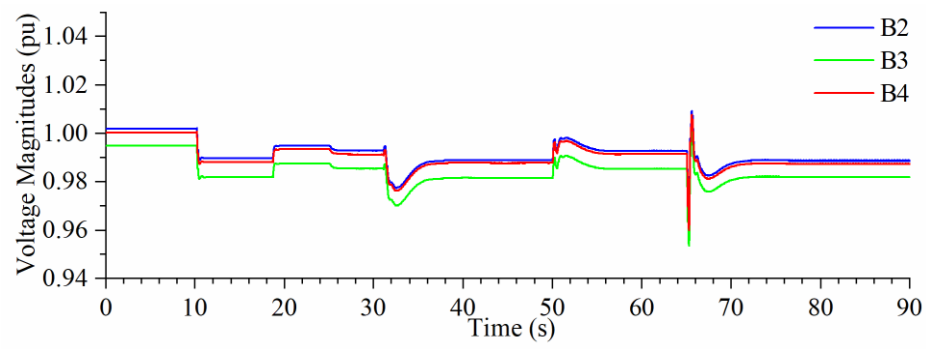

Figure 2.27. Voltage magnitudes at various buses.

2.5. Conclusion

In this chapter, PV system fundamentals and commonly used MPPT techniques have been reviewed. In addition, a campus microgrid coordinately supplied and controlled by the CHP and PV systems in islanded mode has been modeled with high precision. A double-stage PV-VSG control scheme has been proposed to study the integration of a 10-MW PV farm. This method utilizes the DC-link capacitor for inertia emulation and demonstrates satisfactory transient performance under varying operating conditions. Moreover, the feasibility and effectiveness of the coordinated control between the CHP and PV systems for stable operation of the islanded campus microgrid has been corroborated in extensive numerical simulations.

Chapter 3

Predictive Hierarchical Power Management of Islanded Microgrids

3.1 Introduction

This chapter presents an enhanced three-layer predictive hierarchical power management framework proposed for the secure and economic operation of islanded microgrids comprising SGs and PVs. The tertiary control is built upon the centralized semi-definite programming-based AC optimal power flow (AC-OPF) model from [112], which has been adapted to accommodate microgrid operations. The tertiary controller periodically sends power commands to the secondary control, aiming to ensure the economic operation of the microgrid. A centralized linear model MPC controller is proposed for the secondary control to mitigate the uncertainties caused by renewable generation and loads. With low computational complexity, the MPC controller can effectively regulate the microgrid system frequency and closely track reference signals from the tertiary controller. Besides, droop-based primary controllers are implemented to coordinate with the secondary MPC controller to balance the systems in real time. The specifics of the hierarchical power management framework, as well as the detailed system modeling and simulation are provided in the following subsections.

3.2 Outline of the Hierarchical Power Management Framework

Figure 3.1 illustrates the proposed three-level predictive hierarchical power management framework for islanded microgrids.

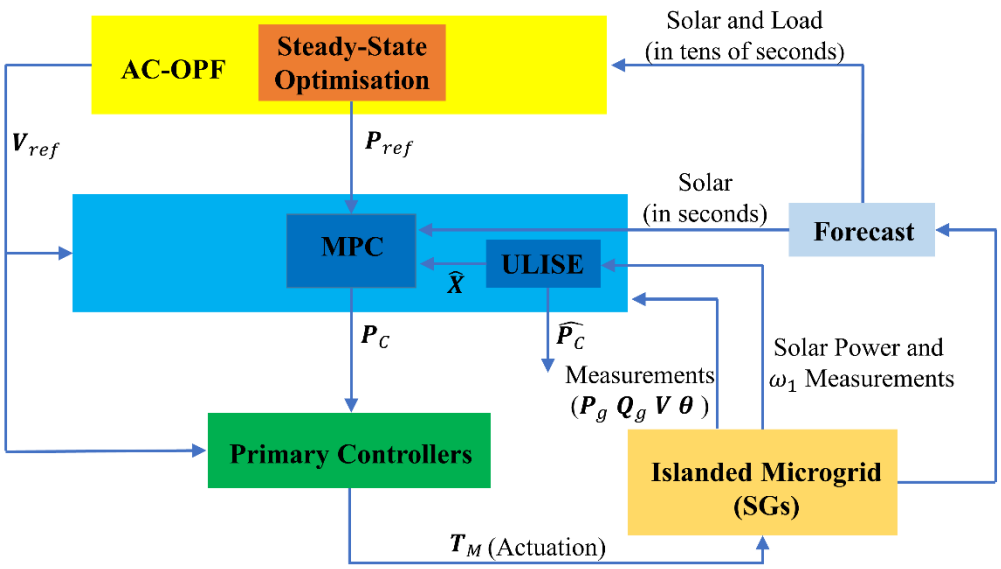

Figure 3.1. Overall block diagram of the hierarchical power management framework.

The AC-OPF is implemented as the tertiary controller to set the reference values for the secondary and the primary level controllers. Given the dynamics decoupling from the dynamical secondary control and also the fact that forecasting error goes down with a shortened time scale, the AC-OPF takes load and renewable forecasts in tens of seconds and executes in the same time frame. Generally, a microgrid with high renewable integration necessitates sufficient reactive power support, without which voltage instability may occur during system operation. Static var compensators (SVCs) or static synchronous compensators (STATCOMs) are used to underpin the reactive power compensation in our simulated system, with voltage references V_{ref} periodically derived from the AC-OPF module and applied to the SG excitation systems to regulate their terminal voltages.

The secondary control is implemented via a linear MPC controller responsible for system frequency regulation and active power control in the time frame of several seconds.

During each control time interval, MPC will generate an optimal control trajectory by solving an optimization problem over an extended time frame, whereas only the solution to the first control time interval will be used for actual control. The proposed MPC controller is built on a linearized system model (also known as prediction model) that is updated at run time to account for nonlinearity and time-varying system states. The proposed MPC controller makes sequential control decisions based on the system state estimation via a unified linear input-state estimator (ULISE) [113], while taking in renewable forecasts within a receding horizon. In addition, the proposed ULISE can simultaneously estimate the secondary control signals actually received by the primary controllers from MPC. Thus, whether the control signals sent from the secondary MPC controller are successfully received by the primary controller without being compromised can be effectively identified. This way, not only the system observability but also the situational awareness can be greatly enhanced. The primary controllers, consisting of the excitation and turbine-governor systems, receive the voltage references from the AC-OPF and power settings from the MPC, respectively.

3.3 Microgrid System Modeling

An islanded microgrid with dispatchable SGs and intermittent solar PVs is modeled based on a practical microgrid system. The PVs are operated in MPPT mode as detailed in Chapter 2. SGs, loads, and PV arrays connected to the same bus will be aggregated. The microgrid consists of a set of N_G aggregated SGs ($\boldsymbol{\mathcal{G}}$ represents this set), N_{PV} aggregated PV arrays ($\boldsymbol{\mathcal{R}}$), N_D aggregated loads ($\boldsymbol{\mathcal{D}}$), N_l lines ($\boldsymbol{\mathcal{L}}$), and N_b buses ($\boldsymbol{\mathcal{N}}$). The first N_G buses are the generator buses, while the rest are the load buses. The detailed nomenclature

is provided in Table 3.1.

Table 3.1

Nomenclature

A. Variables and Constants	
ω_s	Nominal synchronous velocity (rad/sec)
ω	Rotor angular velocity (rad/s)
δ	Rotor angle (rad)
T_M	Mechanical torque (pu)
H	Inertia constant (s)
D	Damping factor
T'_{do}	*D*-axis transient open-circuit time constant (s)
R_s	Stator resistance (pu)
X'_d	*D*-axis transient reactance (pu)
X_d, X_q	*D*-*q* axes synchronous reactances (pu)
E_{fd}, E'_q	Field winding and *q*-axis transient voltages (pu)
I_d, I_q	*D*-*q* axes stator currents (pu)
K_A	Combined gain of exciter and voltage regulator
T_A	Overall time constant (sec) of exciter and regulator
V_{ref}	Voltage reference to voltage regulator (pu)
T_{CH}	Overall time constant (sec) of turbine and governor
R_D	Droop gain

A. Variables and Constants	
P_C	Power change setting to governor (pu)
$V,\ \theta$	Bus voltage magnitude (pu) and angle (rad)
P_g, Q_g	Active and reactive powers (pu) of SG
P_D, Q_D	Aggregate active and reactive loads (pu)
P_{PV}, Q_{PV}	Active and reactive powers (pu) of PV array
P_{ref}	Economic dispatch set-point (pu) of SG
i, j	Index of Buses
θ	Bus angle (rad)
$\mathbf{Y}_b$	Bus admittance matrix
T_s, T_c	Model update period and control interval
N_p, N_c	Prediction horizon and control horizon
B. Symbols	
$(\cdot)^T$	Transpose
$\mathrm{trace}(\cdot)$	Trace
$(\cdot) \succeq 0$	Positive semi-definite matrix
$\mathrm{diag}(\cdot)$	Diagonal matrix
$\mathrm{var}(\cdot)$	Variance
$\mathbb{E}[\cdot]$	Expectation
$(\cdot)^\dagger$	Moore-Penrose pseudoinverse
$\widehat{(\cdot)}$	Estimate

3.3.1 Microgrid Component Modeling

3.3.1.1 SG Model. Given the trade-off between model accuracy and computation speed, the simplified third-order one-axis model (3.1-3.3) is used to represent the SG at bus *i* for its good dynamic decryption [104], assuming that the *d*-axis component of the internal voltage behind the transient reactance has vanished and that each SG is installed with a non-reheat steam turbine and a fast excitation system.

$$\dot{\delta}_i = \omega_i - \omega_{com} \tag{3.1}$$

$$\dot{\omega}_i = \frac{T_{Mi}}{M_i} - \frac{E'_{qi} I_{qi}}{M_i} - \frac{(X_{qi} - X'_{di})}{M_i} I_{di} I_{qi} - \frac{D_i(\omega_i - \omega_{com})}{M_i} \tag{3.2}$$

$$\dot{E'_{qi}} = -\frac{E'_{qi}}{T'_{doi}} - \frac{(X_{di} - X'_{di})}{T'_{doi}} I_{di} + \frac{E_{fdi}}{T'_{doi}} \tag{3.3}$$

where ω_{com} is the angular velocity of the common reference frame conventionally chosen as the nominal synchronous speed ω_s in a large system [114]. However, ω_{com} usually deviates from the nominal frequency in the context of islanded microgrids. M_i denotes the constant $\frac{2H_i}{\omega_s}$, and the time is in seconds. Since the governor dynamics usually dies out much faster than the turbine dynamics [115], the governor valve position is not considered as a state variable. Each SG is expressed in a *d*-*q* reference frame rotating with its own rotor.

The overall high-gain static excitation system model of the SG is:

$$\dot{E}_{fdi} = -\frac{E_{fdi}}{T_{Ai}} + \frac{K_{Ai}(V_{ref,i} - V_i)}{T_{Ai}} \tag{3.4}$$

The turbine-governor model of the SG is:

$$\dot{T}_{Mi} = -\frac{T_{Mi}}{T_{CHi}} + \frac{P_{Ci}}{T_{CHi}} - \frac{1}{R_{Di}T_{CHi}}\left(\frac{\omega_i}{\omega_s} - 1\right) \tag{3.5}$$

For the SG at bus i, its stator voltage equations are:

$$V_i \sin(\delta_i - \theta_i) + R_{si}I_{di} - X_{qi}I_{qi} = 0 \tag{3.6}$$

$$V_i \cos(\delta_i - \theta_i) + R_{si}I_{qi} + X'_{di}I_{di} - E'_{qi} = 0 \tag{3.7}$$

The active and reactive power outputs of the SG when the stator resistance is neglected are:

$$P_{gi} = X_{qi}I_{di}I_{qi} + I_{qi}\left(E'_{qi} - X'_{di}I_{di}\right) \tag{3.8}$$

$$Q_{gi} = -X_{qi}I_{qi}^2 + I_{di}(E'_{qi} - X'_{di}I_{di}) \tag{3.9}$$

3.3.1.2 PV Model. The PV array is modeled as a controlled AC current source operating with time-varying power generation at unity power factor.

3.3.1.3 Load Model. A static ZIP load (3.10- 3.11) is modeled:

$$P_{Di} = P_{Dni}(a_{1i}V_i^2 + a_{2i}V_i + a_{3i}) \tag{3.10}$$

$$Q_{Di} = Q_{Dni}(b_{1i}V_i^2 + b_{2i}V_i + b_{3i}) \tag{3.11}$$

where n stands for the nominal value of the aggregated load at bus i. Each load is comprised of constant impedance (Z), constant current (I), and constant power (P) components. The coefficients a_{1i} to a_{3i} and b_{1i} to b_{3i} define the proportions of each component.

3.3.1.4 Network Model. The nominal π model [116] is used for the microgrid network modeling, and the power balance for bus i is shown in (3.12- 3.13):

$$I_{di}V_i \sin(\delta_i - \theta_i) + I_{qi}V_i \cos(\delta_i - \theta_i) + P_{PVi} - P_{Di} = \sum_{j=1}^{N_b} V_i V_j Y_{ij} \cos\left(\theta_i - \theta_j - \alpha_{ij}\right) \tag{3.12}$$

$$I_{di}V_i\cos(\delta_i-\theta_i)-I_{qi}V_i\sin(\delta_i-\theta_i)+Q_{PVi}-Q_{Di}=\sum_{j=1}^{N_b}V_i\,V_jY_{ij}\sin\left(\theta_i-\theta_j-\alpha_{ij}\right) \tag{3.13}$$

where α_{ij} and Y_{ij} denote the angle and magnitude of the ij^{th} element of the bus admittance matrix $\mathbf{Y}_b$, respectively. The corresponding terms will be zero when a grid component is absent from the above two equations.

3.3.2 Linearization of the Microgrid System Model

Linearization of the above differential-algebraic equations (DAEs) that model the microgrid system lays the foundation for the design of the secondary MPC controller. Since the *d-q* coordinates of each SG should have a reference angle, all the SG and bus angles are defined relative to the rotor angle of the SG at bus 1 as:

$$\begin{aligned}\delta_i' &:= \delta_i-\delta_1 \qquad & i=1,\dots,N_G\\ \theta_i' &:= \theta_i-\delta_1 \qquad & i=1,\dots,N_b\end{aligned} \tag{3.14}$$

Vectors of state variables $\Delta\boldsymbol{X}$, output variables $\Delta\boldsymbol{Y}$ etc. are defined as below:

$$\begin{aligned}\Delta\boldsymbol{X} &:= [\Delta\delta_1',\Delta\omega_1,\Delta E_{q1}',\Delta E_{fd1},\Delta T_{M1},\dots,\Delta E_{fdN_G},\Delta T_{MN_G}],\\ \Delta\boldsymbol{Y} &:= [\Delta P_{g1},\Delta Q_{g1},\dots,\Delta P_{gN_G},\Delta Q_{gN_G}],\\ \Delta\boldsymbol{I}_g &:= [\Delta I_{d1},\Delta I_{q1},\dots,\Delta I_{dN_G},\Delta I_{qN_G}]^T,\\ \Delta\boldsymbol{V}_g &:= \left[\Delta\theta_1',\Delta V_1,\dots,\Delta\theta_{N_G}',\Delta V_{N_G}\right]^T,\\ \Delta\boldsymbol{V}_l &:= \left[\Delta\theta_{N_G+1}',\Delta V_{N_G+1},\dots,\Delta\theta_{N_b}',\Delta V_{N_b}\right]^T,\\ \Delta\boldsymbol{U}_c &:= [\Delta\boldsymbol{U}_1^T,\Delta\boldsymbol{U}_2^T]^T,\end{aligned} \tag{3.15}$$

where

$$\Delta\boldsymbol{U}_1 := \left[\Delta\omega_1,\Delta V_{ref1},\Delta V_{ref2},\dots,\Delta V_{refN_G}\right]^T,$$

$$\Delta \boldsymbol{U}_2 \coloneqq \left[\Delta P_{C1}, \Delta P_{C2}, \dots, \Delta P_{CN_G}\right]^T,$$
$$\Delta \boldsymbol{S}_{1PV} \coloneqq [\Delta P_{PV1}, \Delta Q_{PV1}, \dots, \Delta P_{PVN_G}, \Delta Q_{PVN_G}]^T,$$
$$\text{and } \Delta \boldsymbol{S}_{2PV} \coloneqq [\Delta P_{PVN_G+1}, \Delta Q_{PVN_G+1}, \dots, \Delta P_{PVN_b}, \Delta Q_{PVN_b}]^T.$$

Linearization of (3.1)- (3.5) leads to the compact form (3.16):

$$\Delta \dot{\boldsymbol{X}} = \boldsymbol{A}_1 \Delta \boldsymbol{X} + \boldsymbol{B}_1 \Delta \boldsymbol{I}_g + \boldsymbol{B}_2 \Delta \boldsymbol{V}_g + \boldsymbol{E}_1 \Delta \boldsymbol{U}_c \tag{3.16}$$

where $[\boldsymbol{A}_1]_{(5N_G \times 5N_G)}$, $[\boldsymbol{B}_1]_{(5N_G \times 2N_G)}$ and $[\boldsymbol{B}_2]_{(5N_G \times 2N_G)}$ are block diagonal matrices.

Linearizing (3.6- 3.7) yields the augmented form of (3.17):

$$\boldsymbol{C}_1 \Delta \boldsymbol{X} + \boldsymbol{D}_1 \Delta \boldsymbol{I}_g + \boldsymbol{D}_2 \Delta \boldsymbol{V}_g = \boldsymbol{0} \tag{3.17}$$

where $[\boldsymbol{C}_1]_{(2N_G \times 5N_G)}$, $[\boldsymbol{D}_1]_{(2N_G \times 2N_G)}$, and $[\boldsymbol{D}_2]_{(2N_G \times 2N_G)}$ are block diagonal matrices.

Linearizing the network equations (3.12- 3.13) of generator buses yields:

$$\boldsymbol{C}_2 \Delta \boldsymbol{X} + \boldsymbol{D}_3 \Delta \boldsymbol{I}_g + \boldsymbol{D}_4 \Delta \boldsymbol{V}_g + \boldsymbol{D}_5 \Delta \boldsymbol{V}_l + \boldsymbol{F}_1 \Delta \boldsymbol{S}_{1PV} = 0 \tag{3.18}$$

where $[\boldsymbol{C}_2]_{(2N_G \times 5N_G)}$ and $[\boldsymbol{D}_3]_{(2N_G \times 2N_G)}$ are block diagonal matrices, $[\boldsymbol{D}_4]_{(2N_G \times 2N_G)}$ and $[\boldsymbol{D}_5]_{(2N_G \times 2(N_b - N_G))}$ are full matrices, and $[\boldsymbol{F}_1]_{(2N_G \times 2N_G)}$ is a sparse incidence matrix with diagonal entries of 1 if a PV is present on the corresponding bus.

Likewise, for load buses, (3.12- 3.13) are linearized as:

$$\boldsymbol{D}_6 \Delta \boldsymbol{V}_g + \boldsymbol{D}_7 \Delta \boldsymbol{V}_l + \boldsymbol{F}_2 \Delta \boldsymbol{S}_{2PV} = 0 \tag{3.19}$$

where $[\boldsymbol{D}_6]_{(2(N_b - N_G) \times 2N_G)}$ and $[\boldsymbol{D}_7]_{(2(N_b - N_G) \times 2(N_b - N_G))}$ are full matrices, and $[\boldsymbol{F}_2]_{(2(N_b - N_G) \times 2(N_b - N_G))}$ is a sparse incidence matrix with entries either 0 or 1. ΔQ_{PV} at all

buses is 0 since PV is modeled at unity power factor.

$\Delta \boldsymbol{I}_g$ in (3.16) and (3.18) is eliminated via (3.17). Then $\boldsymbol{E}_1$ in (3.16) could be partitioned as $\boldsymbol{E}_{11}$ and $\boldsymbol{E}_{12}$ according to $\Delta \boldsymbol{U}_1$ and $\Delta \boldsymbol{U}_2$, and $\left[\Delta \boldsymbol{V}_g^T \quad \Delta \boldsymbol{V}_l^T\right]^T$ is further eliminated. After some algebra, $\boldsymbol{E}_{11}$ is contained in a new matrix $\boldsymbol{B}_{sys}$ and the linearized state equations could be represented as (3.20) based on (3.16- 3.19):

$$\Delta \dot{\boldsymbol{X}} = \boldsymbol{A}_{sys} \Delta \boldsymbol{X} + \boldsymbol{B}_{sys} \Delta \boldsymbol{S} + \boldsymbol{E}_{12} \Delta \boldsymbol{U}_2 \tag{3.20}$$

where $\Delta \boldsymbol{S} \coloneqq [\Delta \boldsymbol{U}_{\boldsymbol{1}}^T \quad \Delta \boldsymbol{S}_{PV}^T]^T$ and $\Delta \boldsymbol{S}_{PV} \coloneqq [\Delta \boldsymbol{S}_{1PV}^T \quad \Delta \boldsymbol{S}_{2PV}^T]^T$.

Similarly, after $\Delta \boldsymbol{I}_g$ is eliminated from the linearized form of (3.8- 3.9), the system output equations result:

$$\Delta \boldsymbol{Y} = \boldsymbol{C}_{sys} \Delta \boldsymbol{X} + \boldsymbol{D}_{sys} \Delta \boldsymbol{S} \tag{3.21}$$

The linear time-varying microgrid system modeled as (3.20) and (3.21) is discretized for digital control. In what follows, the subscripts are dropped, and the discretized system model is formulated as:

$$\Delta \boldsymbol{X}(k+1) = \boldsymbol{A} \Delta \boldsymbol{X}(k) + \boldsymbol{B} \Delta \boldsymbol{S}(k) + \boldsymbol{E} \Delta \boldsymbol{U}(k) \tag{3.22}$$

$$\Delta \boldsymbol{Y}(k) = \boldsymbol{C} \Delta \boldsymbol{X}(k) + \boldsymbol{D} \Delta \boldsymbol{S}(k) \tag{3.23}$$

where $\Delta \boldsymbol{S}(k)$ represents the vector of known inputs, and $\Delta \boldsymbol{U}(k)$ denotes the vector of unknown inputs at time instant *k*, which are also known as the manipulated inputs in MPC.

3.4 AC-OPF Problem Formulation – Tertiary Control

The AC-OPF problem seeks decision variable values that lead to an optimal operating point for an electrical power system in terms of a specified objective function

that can be minimum total generating cost, network losses, etc., subject to network equality constraints (power flow equations) and engineering inequality constraints such as physical limits on active/reactive power generations of distributed generators and power flows on the lines. Let $V_i = V_{di} + jV_{qi}$ represent the bus voltage phasors in rectangular coordinates, and s_{lm} represents the apparent power flow along the nominal π model line $(l, m) \in \boldsymbol{\mathcal{L}}$. In addition, the bus admittance matrix $\mathbf{Y}_b = \mathbf{G} + j\mathbf{B}$.

3.4.1 Classical AC-OPF Problem

A quadratic operating cost function is commonly adopted for each SG $i \in \boldsymbol{\mathcal{G}}$.

$$C_i(P_{gi}) := c_{i2} \cdot P_{gi}^2 + c_{i1} \cdot P_{gi} + c_{i0} \tag{3.24}$$

where c_{i2} $(\$/(\text{hour} \cdot \text{MW}^2))$, $c_{i1}(\$/(\text{hour} \cdot \text{MW}))$, and c_{i0} $(\$/\text{hour})$ are the quadratic, linear and constant cost coefficients, respectively. P_{gi} is the active power output in MW. The AC-OPF problem is formulated as follows:

$$\min_{P_g, Q_g, V_d, V_q, S} \sum_{i \in \boldsymbol{\mathcal{G}}} C_i(P_{gi}) \tag{3.25.1}$$

$$s.t. \quad P_{gi}^{min} \le P_{gi} \le P_{gi}^{max} \qquad \forall i \in \boldsymbol{\mathcal{G}} \tag{3.25.2}$$

$$Q_{gi}^{min} \le Q_{gi} \le Q_{gi}^{max} \qquad \forall i \in \boldsymbol{\mathcal{G}} \tag{3.25.3}$$

$$(V_i^{min})^2 \le V_{di}^2 + V_{qi}^2 \le (V_i^{max})^2 \quad \forall i \in \boldsymbol{\mathcal{N}} \tag{3.25.4}$$

$$|S_{lm}| \le S_{lm}^{max} \qquad \forall (l, m) \in \boldsymbol{\mathcal{L}} \tag{3.25.5}$$

$$P_{gi} - P_{Di} = V_{di} \sum_{j=1}^{N_b} (\mathbf{G}_{ji} V_{dj} - \mathbf{B}_{ji} V_{qj}) + V_{qi} \sum_{j=1}^{N_b} (\mathbf{B}_{ji} V_{dj} + \mathbf{G}_{ji} V_{qj}) \tag{3.25.6}$$

$$Q_{gi} - Q_{Di} = V_{di} \sum_{j=1}^{N_b} (-\mathbf{B}_{ji} V_{dj} - \mathbf{G}_{ji} V_{qj}) + V_{qi} \sum_{j=1}^{N_b} (\mathbf{G}_{ji} V_{dj} - \mathbf{B}_{ji} V_{qj}) \tag{3.25.7}$$

The above AC-OPF problem is non-convex due to the nonlinear power flow

equations (3.25.6) and (3.25.7) and is generally NP-hard.

3.4.2 SDP Relaxation of the AC-OPF Problem

Using SDP to solve nonlinear AC OPF problems provides several advantages, such as a guarantee of global optimality and fast computation. A formulation based on SDP will be presented, which derives from [112]. In addition, forecasted solar PV generation will be considered in this formulation. The classical AC-OPF problem is reformulated with bus voltages defined in rectangular coordinates as $\mathbf{V} = \left[V_{d1}, V_{d2}, \dots, V_{dN_b}, V_{q1}, V_{q2}, \dots, V_{qN_b}\right]^T$. Let $\boldsymbol{e}_i$ denote the ith standard basis vector in $\mathbb{R}^{N_b}$. Define the matrix $\boldsymbol{Y}_i = \boldsymbol{e}_i \cdot \boldsymbol{e}_i^T \cdot \mathbf{Y_b}$ and the matrix $\boldsymbol{Y}_{lm} = \left(y_{lm} + \frac{jb_{lm}}{2}\right)\boldsymbol{e}_l \cdot \boldsymbol{e}_l^T - y_{lm}\boldsymbol{e}_l \cdot \boldsymbol{e}_m^T$, where y_{lm} is the series admittance and b_{lm} is the total shunt susceptance of line $(l, m) \in \mathcal{L}$. The matrices that will be used in the SDP formulation are given as follows:

$$\mathbf{Y}_i = \frac{1}{2}\begin{bmatrix} \mathrm{Re}(\boldsymbol{Y}_i + \boldsymbol{Y}_i^T) & \mathrm{Im}(\boldsymbol{Y}_i^T - \boldsymbol{Y}_i) \\ \mathrm{Im}(\boldsymbol{Y}_i - \boldsymbol{Y}_i^T) & \mathrm{Re}(\boldsymbol{Y}_i + \boldsymbol{Y}_i^T) \end{bmatrix} \tag{3.26.1}$$

$$\overline{\mathbf{Y}}_i = -\frac{1}{2}\begin{bmatrix} \mathrm{Im}(\boldsymbol{Y}_i + \boldsymbol{Y}_i^T) & \mathrm{Re}(\boldsymbol{Y}_i - \boldsymbol{Y}_i^T) \\ \mathrm{Re}(\boldsymbol{Y}_i^T - \boldsymbol{Y}_i) & \mathrm{Im}(\boldsymbol{Y}_i + \boldsymbol{Y}_i^T) \end{bmatrix} \tag{3.26.2}$$

$$\mathbf{Y}_{lm} = \frac{1}{2}\begin{bmatrix} \mathrm{Re}(\boldsymbol{Y}_{lm} + \boldsymbol{Y}_{lm}^T) & \mathrm{Im}(\boldsymbol{Y}_{lm}^T - \boldsymbol{Y}_{lm}) \\ \mathrm{Im}(\boldsymbol{Y}_{lm} - \boldsymbol{Y}_{lm}^T) & \mathrm{Re}(\boldsymbol{Y}_{lm} + \boldsymbol{Y}_{lm}^T) \end{bmatrix} \tag{3.26.3}$$

$$\overline{\mathbf{Y}}_{lm} = -\frac{1}{2}\begin{bmatrix} \mathrm{Im}(\boldsymbol{Y}_{lm} + \boldsymbol{Y}_{lm}^T) & \mathrm{Re}(\boldsymbol{Y}_{lm} - \boldsymbol{Y}_{lm}^T) \\ \mathrm{Re}(\boldsymbol{Y}_{lm}^T - \boldsymbol{Y}_{lm}) & \mathrm{Im}(\boldsymbol{Y}_{lm} + \boldsymbol{Y}_{lm}^T) \end{bmatrix} \tag{3.26.4}$$

$$\mathbf{M}_i = \begin{bmatrix} \boldsymbol{e}_i \cdot \boldsymbol{e}_i^T & \mathbf{0} \\ \mathbf{0} & \boldsymbol{e}_i \cdot \boldsymbol{e}_i^T \end{bmatrix} \tag{3.26.5}$$

Admittance matrices in (3.26.1)- (3.26.2) are used to calculate power injections at each bus, admittance matrices in (3.26.3)- (3.26.4) are defined to calculate line power flows,

and matrix in (3.26.5) is used to obtain bus voltage magnitudes. Then define the rank one matrix $\mathbf{W} = \mathbf{V} \cdot \mathbf{V}^T$, which is equivalent to constraints $\mathbf{W} \succeq \mathbf{0}$ and $\text{rank}(\mathbf{W}) = 1$. This rank constraint leads to nonconvexity. Removing $\text{rank}(\mathbf{W}) = 1$ enables the semidefinite relaxation. The semidefinite relaxation has zero relaxation gap if the matrix $\mathbf{W}$ of a globally optimal solution has rank one. The relaxed SDP formulation of the ACOPF problem is shown as below:

$$\min_{\mathbf{W}} \sum_{i \in \mathcal{G}} \beta_i \tag{3.27.1}$$

$$s.t.\ P_{gi}^{min} - P_{Di} + P_{PVi} \leq \text{trace}(\mathbf{Y}_i \cdot \mathbf{W}) \leq P_{gi}^{max} - P_{Di} + P_{PVi} \quad \forall i \in \mathcal{N} \tag{3.27.2}$$

$$Q_{gi}^{min} - Q_{Di} \leq \text{trace}(\overline{\mathbf{Y}}_i \cdot \mathbf{W}) \leq Q_{gi}^{max} - Q_{Di} \quad \forall i \in \mathcal{N} \tag{3.27.3}$$

$$(V_i^{min})^2 \leq \text{trace}(\mathbf{M}_i \cdot \mathbf{W}) \leq (V_i^{max})^2 \quad \forall\, i \in \mathcal{N} \tag{3.27.4}$$

$$\begin{bmatrix} (s_{lm}^{max})^2 & -\text{trace}(\mathbf{Y}_{lm} \cdot \mathbf{W}) & -\text{trace}(\overline{\mathbf{Y}}_{lm} \cdot \mathbf{W}) \\ -\text{trace}(\mathbf{Y}_{lm} \cdot \mathbf{W}) & 1 & 0 \\ -\text{trace}(\overline{\mathbf{Y}}_{lm} \cdot \mathbf{W}) & 0 & 1 \end{bmatrix} \succeq 0 \ \ \forall (l,m) \in \mathcal{L} \tag{3.27.5}$$

$$\begin{bmatrix} \beta_i - c_{i1} \cdot [\text{trace}(\mathbf{Y}_i \cdot \mathbf{W}) + P_{Di} - P_{PVi}] - c_{i0} & -\sqrt{c_{i2}} \cdot [\text{trace}(\mathbf{Y}_i \cdot \mathbf{W}) + P_{Di} - P_{PVi}] \\ -\sqrt{c_{i2}} \cdot [\text{trace}(\mathbf{Y}_\text{i} \cdot \mathbf{W}) + P_{Di} - P_{PVi}] & 1 \end{bmatrix} \succeq 0 \quad \forall i \in \mathcal{G} \tag{3.27.6}$$

$$\mathbf{W} \succeq 0 \tag{3.27.7}$$

The objective function (3.27.1) seeks to minimize the total operating cost of the microgrid in islanded mode, representing the tertiary-level control objective; the scalar β_i is an auxiliary variable that converts the operating cost function for SG $i \in \mathcal{G}$ from (3.24) to (3.27.6) using the Schur complement formula. The constraints on the active and reactive power outputs of each SG are enforced as (3.27.2) and (3.27.3), respectively. Note that $\text{trace}(\mathbf{Y}_i \cdot \mathbf{W})$ equals the net active power injection at each bus, while $\text{trace}(\overline{\mathbf{Y}}_i \cdot \mathbf{W})$ is the

net reactive power injection. With a slight abuse of notation, P_{Di} and P_{PVi} represent the forecasted solar power load at bus i if they are present. Constraint (3.27.4) limits the bus voltage magnitudes, which corresponds to (3.25.4). The original apparent power flow limit (3.25.5) is converted as (3.27.5) using the Schur complement formula again so that the new constraint becomes quadratic with respect to $\mathbf{V}$. Constraint (3.27.7) facilitates semidefinite relaxation.

Only the solution to (3.27) satisfying $\text{rank}(\mathbf{W}) \leq 2$ can be recovered as the solution to the original AC-OPF problem. Otherwise, the solution is inexact but provides a lower bound on the objective value of the original AC-OPF problem. After periodically solving the AC-OPF problem on the tertiary level, the optimal active and power set-points and the terminal voltage references are derived, which will be dispatched to the centralized MPC controller and the local controllers accordingly for secondary and primary control.

3.5 MPC Problem Formulation - Secondary Control

3.5.1 Linear MPC Controller

Building on the linearized microgrid system model (3.22- 3.23), a linear centralized MPC controller formulated as (3.28) is designed to solve a multi-objective quadratic optimization problem over a prediction horizon. For an islanded microgrid, frequency regulation is of critical significance. Hence, the main goal of the secondary MPC controller is to minimize the accumulated frequency deviations not handled by primary controller, i.e., the first component of (3.28.1), while managing the generation dispatch of SGs following the active power set-points from tertiary controller, i.e., the second component of (3.28.1).

$$\min \sum_{k=1}^{N_p} \left[\Delta_s \boldsymbol{\omega}(t+k|t)^T \boldsymbol{G} \Delta_s \boldsymbol{\omega}(t+k|t) + \Delta_n \boldsymbol{P}_g(t+k|t)^T \boldsymbol{H} \Delta_n \boldsymbol{P}_g(t+k|t)\right] + \rho_\epsilon \epsilon^2 \tag{3.28.1}$$

$$s.t.\ \Delta \boldsymbol{X}(t+k|t) = \boldsymbol{A} \Delta \boldsymbol{X}(t+k-1|t) + \boldsymbol{B} \Delta \boldsymbol{S}(t+k-1|t) + \boldsymbol{E} \Delta \boldsymbol{U}(t+k|t) \tag{3.28.2}$$

$$\Delta \boldsymbol{Y}(t+k|t) = \boldsymbol{C} \Delta \boldsymbol{X}(t+k|t) + \boldsymbol{D} \Delta \boldsymbol{S}(t+k|t) \tag{3.28.3}$$

$$0.99\omega_s \leq \Delta\omega_i(t+k|t) + \omega_i(t) \leq 1.01\omega_s \tag{3.28.4}$$

$$U_i^{min} \leq \Delta U_i(t+k|t) + U_i(t) \leq U_i^{max} \tag{3.28.5}$$

$$Y_i^{min} - \epsilon \mathbf{1} \leq \Delta Y_i(t+k|t) + Y_i(t) \leq Y_i^{max} + \epsilon \mathbf{1} \tag{3.28.6}$$

where t refers to the current control time instant, and the duration of each control interval is T_c. k denotes the kth control interval; N_p is the prediction horizon, defined as the number of T_c the MPC executes in a forward-looking manner. N_c, a portion of N_p, is defined as the control horizon such that $\Delta \boldsymbol{U}(t+j) \equiv \Delta \boldsymbol{U}(t+N_c)$ for $j \in [N_c+1, N_p]$. The reason for introducing N_c is to reduce the number of control variables for a faster computational speed while avoiding potential numerical issues. $\Delta_s \boldsymbol{\omega} := [\Delta_s\omega_1, \Delta_s\omega_2 \ldots, \Delta_s\omega_m]^T/\omega_s$ is the normalized vector of the rotor speed deviations from ω_s, and $\Delta_n \boldsymbol{P}_g := [\Delta_n P_{g1}, \Delta_n P_{g2} \ldots, \Delta_n P_{gm}]^T$ refers to the vector of power output deviations from $\boldsymbol{P}_{ref}$. For predictions at control time instant $t+k$, $\Delta_s\omega_i(t+k|t) := \Delta\omega_i(t+k|t) + \omega_i(t) - \omega_s$ and $\Delta_n P_{gi}(t+k|t) := \Delta P_{gi}(t+k|t) + P_{gi}(t) - P_{ref,i}$. $\boldsymbol{G} \coloneqq diag(g_1, g_2, \ldots, g_m)$ and $\boldsymbol{H} \coloneqq diag(h_1, h_2, \ldots, h_m)$ are diagonal weighting matrices; weights in $\boldsymbol{G}$ are set greater than those in $\boldsymbol{H}$ since frequency regulation is more crucial for an islanded microgrid's secondary control. The first two constraints (3.28.2) and (3.28.3) represent the prediction model based on (3.22) and (3.23). The coefficient matrices $\boldsymbol{A}$, $\boldsymbol{B}$, $\boldsymbol{E}$, $\boldsymbol{C}$ and $\boldsymbol{D}$ are updated at each model update period T_s to adapt the prediction model to the varying system operating conditions and are assumed constant over the prediction horizon. The MPC is executed in every

control interval over the prediction horizon, based on the updated inputs including the system state, measurements, and the PV forecasts. The proposed ULISE works at a higher sampling rate to provide the MPC controller with system state estimations for each control interval, and the rotor speed ω_1 can be obtained using a simple frequency estimator based on a phasor demodulation principle [57]. Constraint (3.28.4) requires the rotor speeds to stay within the permissible bounds, i.e., ±1% ω_s , whereas (3.28.5) constrains the manipulated inputs. In (3.28.6), Y_i^{min} and Y_i^{max} are the vectors representing per unit active and reactive power limits for SG i. The non-negative slack variable ϵ is introduced to relax (3.28.6), as hard output constraints may cause infeasibility owing to unpredicted disturbances or model mismatch. **1** is a column vector of 1s with dimension 2, while the weight ρ_ϵ in the objective function penalizes the violation of this constraint. Micro-synchrophasors can be used to provide measurements of voltage magnitudes, phase angles, active and reactive powers, allowing us to derive an initial condition of the original nonlinear DAE system by referring to the dynamic circuit of the flux-decay model in [104] such that the numerical simulations can initially converge fast.

3.5.2 ULISE

To enhance the performance of the MPC controller, ULISE is proposed to simultaneously estimate the system states and the control signals actually received by primary controllers. This state estimator is built upon the unified filter for general linear discrete-time stochastic systems in [113]. Furthermore, integrating ULISE into the feedback loop of MPC can effectively reduce the controller's sensitivity to output disturbances. Moreover, different from the Kalman filter [59], which can only detect

inconsistency in sensor measurement readings through analytical redundancy approaches, the proposed ULISE can also detect whether control signals sent from the secondary MPC controller are compromised, and thus, the capability of the proposed MPC controller and even the system stability could be enhanced. The control signals received by the primary controllers are estimated and compared with the actual control signals calculated by the MPC, and a considerable deviation suggests the presence of anomalies. Mitigation schemes can be further explored to compensate for the error and thus to guarantee the MPC control performance. It should be emphasized that the proposed filter can generate a UMV estimate (that is, the estimate $\widehat{\boldsymbol{\theta}}$'s variance $var(\widehat{\boldsymbol{\theta}}) = \mathbb{E}\left[(\widehat{\boldsymbol{\theta}} - \mathbb{E}[\widehat{\boldsymbol{\theta}}])^T(\widehat{\boldsymbol{\theta}} - \mathbb{E}[\widehat{\boldsymbol{\theta}}])\right]$ is the smallest out of all unbiased estimates) only when strong detectability is satisfied [113].

For conciseness, the microgrid system model utilized by the ULISE within each model update period T_s is rewritten as:

$$\boldsymbol{X}_{k+1} = \boldsymbol{A}\boldsymbol{X}_k + \boldsymbol{B}\boldsymbol{S}_k + \boldsymbol{E}\boldsymbol{U}_k + \boldsymbol{w}_k \tag{3.29}$$

$$\boldsymbol{Y}_k = \boldsymbol{C}\boldsymbol{X}_k + \boldsymbol{D}\boldsymbol{S}_k + \boldsymbol{v}_k \tag{3.30}$$

Here k refers to the sampling instant of the unified filter. The process noise $\boldsymbol{w}_k \in \mathbb{R}^{5N_G}$ and the measurement noise $\boldsymbol{v}_k \in \mathbb{R}^{2N_G}$ are assumed to be mutually uncorrelated, zero-mean, white random signals with known bounded covariance matrices $\boldsymbol{Q}_k \coloneqq \mathbb{E}[\boldsymbol{w}_k \cdot \boldsymbol{w}_k^T] \succeq 0$ and $\boldsymbol{R}_k \coloneqq \mathbb{E}[\boldsymbol{v}_k \cdot \boldsymbol{v}_k^T] \succeq 0$. The initial state $\boldsymbol{X}_0$ has mean $\widehat{\boldsymbol{X}}_{0|0}$ and covariance $\boldsymbol{P}_{0|0}^{x}$, and is independent of $\boldsymbol{w}_k$ and $\boldsymbol{v}_k$ for all k. The ULISE, detailed in below Table 3.2, is recursively implemented in three steps: i) The "unknown input estimation" uses the current measurements and the state estimates to estimate the unknown inputs in the best linear unbiased sense; ii) the "time update" propagates the state estimates using the system

dynamics; and iii) the "measurement update" updates the state estimates based on the current measurements.

Table 3.2

ULISE Algorithm in the Case of No Direct Feedthrough

1:	Initialize: $\widehat{\boldsymbol{X}}_{0\|0}$, $\boldsymbol{P}^{x}_{0\|0}$ etc.
2:	**for** k = 1 to n_{itr} **do**
	▷ Unknown input estimation of $\boldsymbol{U}_{k-1}$
3:	$\widetilde{\boldsymbol{P}}_k = \boldsymbol{A}\boldsymbol{P}^{x}_{k-1\|k-1}\boldsymbol{A}^T + \boldsymbol{Q}_{k-1}$
4:	$\widetilde{\boldsymbol{R}}_k = \boldsymbol{C}\widetilde{\boldsymbol{P}}_k\boldsymbol{C}^T + \boldsymbol{R}_k$
5:	$\boldsymbol{P}^{d}_{k-1} = \left(\boldsymbol{E}^T\boldsymbol{C}^T\widetilde{\boldsymbol{R}}_k^{-1}\boldsymbol{C}\boldsymbol{E}\right)^{-1}$
6:	$\boldsymbol{M}_k = \boldsymbol{P}^{d}_{k-1}\boldsymbol{E}^T\boldsymbol{C}^T\widetilde{\boldsymbol{R}}_k^{-1}$
7:	$\widehat{\boldsymbol{X}}_{k\|k-1} = \boldsymbol{A}\widehat{\boldsymbol{X}}_{k-1\|k-1} + \boldsymbol{B}\boldsymbol{S}_{k-1}$
8:	$\widehat{\boldsymbol{U}}_{k-1} = \boldsymbol{M}_k\left(\boldsymbol{Y}_k - \boldsymbol{C}\widehat{\boldsymbol{X}}_{k\|k-1} - \boldsymbol{D}\boldsymbol{S}_k\right)$
	▷ Time update
9:	$\widehat{\boldsymbol{X}}^{*}_{k\|k} = \widehat{\boldsymbol{X}}_{k\|k-1} + \boldsymbol{E}\widehat{\boldsymbol{U}}_{k-1}$
10:	$\boldsymbol{P}^{*x}_{k\|k} = \boldsymbol{E}\boldsymbol{M}_k\boldsymbol{R}_k\boldsymbol{M}_k^T\boldsymbol{E}^T + (\boldsymbol{I} - \boldsymbol{E}\boldsymbol{M}_k\boldsymbol{C})\widetilde{\boldsymbol{P}}_k(\boldsymbol{I} - \boldsymbol{E}\boldsymbol{M}_k\boldsymbol{C})^T$
11:	$\widetilde{\boldsymbol{R}}^{*}_k = \boldsymbol{C}\boldsymbol{P}^{*x}_{k\|k}\boldsymbol{C}^T + \boldsymbol{R}_k - \boldsymbol{C}\boldsymbol{E}\boldsymbol{M}_k\boldsymbol{R}_k - \boldsymbol{R}_k\boldsymbol{M}_k^T\boldsymbol{E}^T\boldsymbol{C}^T$
	▷ Measurement update
12:	$\boldsymbol{K}_k = \boldsymbol{P}^{*x}_{k\|k}\boldsymbol{C}^T - \boldsymbol{E}\boldsymbol{M}_k\boldsymbol{R}_k$
13:	$\boldsymbol{L}_k = \boldsymbol{K}_k\widetilde{\boldsymbol{R}}_k^{*\dagger}$
14:	$\widehat{\boldsymbol{X}}_{k\|k} = \widehat{\boldsymbol{X}}^{*}_{k\|k} + \boldsymbol{L}_k\left(\boldsymbol{Y}_k - \boldsymbol{C}\widehat{\boldsymbol{X}}^{*}_{k\|k} - \boldsymbol{D}\boldsymbol{S}_k\right)$
15:	$\boldsymbol{P}^{x}_{k\|k} = \boldsymbol{P}^{*x}_{k\|k} + \boldsymbol{L}_k\widetilde{\boldsymbol{R}}^{*}_k\boldsymbol{L}_k^T - \boldsymbol{K}_k\boldsymbol{L}_k^T - \boldsymbol{L}_k\boldsymbol{K}_k^T$
16:	**end for**

Here, n_{itr} refers to the maximum number of iterations for each T_s. All coefficient matrices are updated every T_s, and the covariance matrices of process and measurement noises are assumed to be constant throughout the simulation. $\boldsymbol{P}_{k-1}^{d}$ is the covariance matrix of the optimal input error estimates, $\widehat{\boldsymbol{U}}_{k-1}$ is the unknown input estimates at time instant $k-1$, $\boldsymbol{M}_k$ is the filter gain matrix which is chosen to minimize the state and input error covariances, and $\boldsymbol{P}_{k|k}^{*x}$ represents the propagated state estimate error covariance matrix. $\boldsymbol{P}_{k|k}^{x}$ is the updated covariance matrix of state error. The estimated states $\widehat{\boldsymbol{X}}_{k|k}$ in the last iteration together with system measurements are used to update the coefficient matrices for the next T_s. In normal conditions, e.g., when no external manipulation is altered, $\widehat{\boldsymbol{U}}$ yielded in the first step should be close to zero during each T_s. It is noted that the case in our framework represents a special case of the general ULISE algorithm because there is no direct feedthrough, i.e., the term related to $\boldsymbol{U}_k$ is absent in (3.30) because the coefficient matrix of $\boldsymbol{U}_k$ is zero. In this regard, no transformation of the output equations and no decomposition of the unknown input vector are necessary. Further, the algorithm will reduce to the conventional Kalman filtering if both the coefficient matrices of $\boldsymbol{U}_k$ in (3.29) and (3.30) are empty.

3.6 Case Studies

3.6.1 Simulation Setup

Figure 3.2 illustrates the single-line diagram of a simulated microgrid built on a 13.2-kV practical distribution network. This 13-bus microgrid connects 11 entities on a dedicated ring. When disconnected from the main grid, these entities are powered by four on-site SGs. Two STATCOMs are installed at buses 2 and 10 for reactive power

compensation. Besides, a 2-MW PV farm is integrated into the microgrid at bus 11. The power factor of the ZIP loads ranges from 0.85 to 0.9 lagging, and the total active load is around 8.12 MW. The detailed system and control parameters are available in Tables 3.3-3.6, respectively. The system base power, voltage, and nominal frequency are 10 MVA, 13.2 kV, and 60 Hz, respectively. SGs are simulated using MATLAB/Simulink's existing modules. The components of $\boldsymbol{w}_k$ and $\boldsymbol{v}_k$ used in the unified filter are set to be Gaussian random variables with zero mean and standard deviation $\sigma = 10^{-2}$. The initial vector of system states is set as $\widehat{\boldsymbol{X}}_{0|0} = \boldsymbol{0}_{(5m\times 1)}$, while the covariance matrix of state error is initialized as $\boldsymbol{P}^{x}_{0|0} = \mathrm{diag}([10^{-1}, \dots, 10^{-1}]_{(5m\times 1)})$. The communication latency is neglected considering the microgrid does not span a large geographical area.

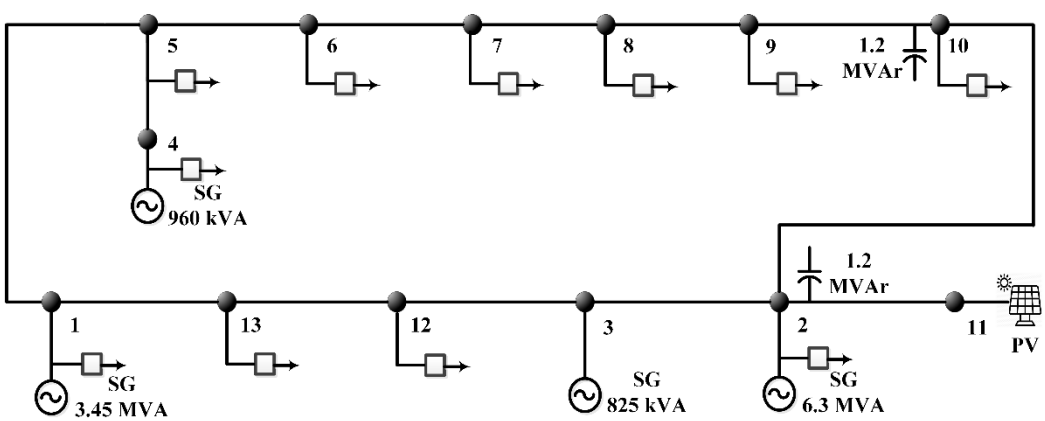

Figure 3.2. Single-line diagram of the islanded microgrid test system.

Table 3.3

Line Data for the 13-Bus Test System

From	To	r (pu)	x (pu)	b (pu)	s_{lm}^{max}(MVA)
1	5	0.00525	0.00649	0.003	5.7333
1	13	0.00330	0.00409	0.002	5.9043
2	3	0.01389	0.01718	0.007	5.6830
2	10	0.01190	0.01472	0.006	4.7878
2	11	0.01372	0.01697	0.007	0.5432
3	12	0.00064	0.00079	0.000	6.0149
4	5	0.00703	0.00869	0.003	0.3621
5	6	0.00703	0.00869	0.003	5.8439
6	7	0.00021	0.00026	0.000	6.0149
7	8	0.00567	0.00702	0.003	5.6830
8	9	0.00737	0.00911	0.004	5.0594
9	10	0.00919	0.01137	0.005	4.9286
12	13	0.00068	0.00084	0.000	5.9546

Table 3.4

Load Data for the 13-Bus Test System

Loads	P_{DN}	Q_{DN}	a_1	a_2	a_3	b_1	b_2	b_3
L1	3.6	2.13	0.4	-0.41	1.01	4.43	-7.98	4.56
L2	3.3	2	0.38	-0.39	1.01	4.4	-7.92	4.52
L4	0.084	0.05	1.21	-1.61	1.41	4.35	-7.08	3.72
L5	0.048	0.028	0.27	-0.33	1.06	5.48	-9.7	5.22
L6	0.144	0.086	0.3	-0.42	1.12	5.39	-9.4	5.03

Loads	P_{DN}	Q_{DN}	a_1	a_2	a_3	b_1	b_2	b_3
L7	0.054	0.031	0.55	0.24	0.21	0.55	-0.09	0.54
L8	0.504	0.299	0.76	-0.52	0.76	6.92	-11.75	5.83
L9	0.123	0.074	1.24	-1.62	1.38	4.31	-6.96	3.65
L10	0.142	0.0842	0.77	-0.84	1.07	8.09	-13.65	6.56
L12	0.048	0.0284	0.69	0.04	0.27	1.82	-2.24	1.43
L13	0.048	0.0285	0.28	-0.35	1.08	5.32	-8.9	4.59

Note. P_{DN} is in MW and Q_{DN} is in Mvar.

Table 3.5

SG Data for the 13-Bus Test System

DGs	SG1	SG2	SG3	SG4
Rating (MVA)	3.45	6.3	0.825	0.96
H (sec)	1.93	2.81	0.9	0.778
D	0.0023	0.0023	0.0015	0.0015
X_d (pu)	3.1	2.4	2.95	2.89
X_q (pu)	1.75	1.77	2.36	1.72
X'_d (pu)	0.316	0.27	0.14	0.25
T'_{do} (sec)	3.5	2.3	1.7	1.46
K_A	300	300	300	300
T_A (sec)	0.01	0.01	0.01	0.01
T_{CH} (sec)	0.4	0.4	0.2	0.2
R_D	0.05	0.05	0.05	0.05
C_2	18.7	18.5	18.6	18.9
C_1	62	64	63	62
C_0	9	9	10	10

Table 3.6

Control Parameters

MPC		PI	
$g_1 = 18.94$	$g_2 = 18.94$	$P_1 = 0.07$	$I_1 = 0.0032$
$g_3 = 16.3$	$g_4 = 16.3$	$P_2 = 0.07$	$I_2 = 0.0032$
$h_1 = 0.947$	$h_2 = 0.947$	$P_3 = 0.08$	$I_3 = 0.0045$
$h_3 = 0.815$	$h_4 = 0.815$	$P_4 = 0.08$	$I_4 = 0.0045$
$\rho_\epsilon = 10^6$			

All the simulations are carried out on a PC with an Intel Core i7 at 3.8 GHz (Quad-Core) and 64-GB RAM. The MPC controller is designed using the MPC Toolbox in MATLAB. When the controller detects infeasibility, the latest successful control outputs will be retained. Also, the controller will issue a time-out error and terminate the optimization problem if it is not solved within the prescribed control interval. The coordination period between the tertiary AC-OPF and the secondary MPC has an impact on the overall performance of the proposed hierarchical control framework. A greater coordination period could compromise the MPC's power tracking abilities, while a smaller coordination period could cause greater system frequency deviations at transients. Therefore, it is empirically set that the tertiary control executes AC-OPF and updates power set-points every 15 sec. The average computational overhead for obtaining an optimal solution to the AC-OPF of the 13-bus system is 0.542 sec. During each 15-sec interval, the secondary MPC controller keeps solving the receding optimization problem every T_c over the prediction horizon (N_p of T_c) until the new power references for the next 15 sec are

received from tertiary control. The choices of secondary control interval and prediction horizon are based on the tradeoff between performance and computational effort. In the following tests, $N_p = 5, N_c = 3$ and $T_c = 1$ sec are chosen. The average computation time per step for this setting is 0.307 sec. To better capture system dynamics while reducing computational overhead, the model update period T_s is set as 0.02 sec and the sampling time for the ULISE is 2 msec in the simulations.

To assist the MPC and AC-OPF executions, auto-regressive integrated moving average (ARIMA) models [117] are utilized to provide solar power predictions at different timescales. Specifically, as regards the secondary level, historical solar power outputs with a 1-sec sampling rate is used to train the corresponding ARIMA(p, d, q) model, where p denotes the order of auto-regressive (AR), d is the number of nonseasonal differences, and q means the order of moving average (MA). The sample autocorrelation coefficient (ACC) and partial autocorrelation coefficient (PACC) are calculated to determine the nonseasonal differencing before p and q are identified using properly transformed time series. The model orders are determined as (7, 1, 0) via time series analysis in R programming. This model is utilized at each control interval to predict over the prediction horizon using the last 7 (p) measurements of actual solar power outputs. It can be regularly trained with new data. As shown in Figure 3.3, a segment of the actual historical power output of the PV farm in 1-sec resolution is used for simulation purposes. The corresponding forecasted solar power generated by this ARIMA model is also given. The error metrics of root mean square error (RMSE) and mean absolute percentage error (MAPE) as defined in [117, 118] are leveraged to evaluate different datasets. With respect to the actual solar power curve, the forecasted curve has an RMSE of 0.0416 MW and a MAPE of 3.84%. Likewise, using

the 15-sec resolution historical solar power data, an ARIMA(3, 1, 1) model is used to forecast solar power of the next 15 sec for the AC-OPF module, and the RMSE and MAPE for the forecasts are found to be 0.1547 MW and 12.41%, respectively.

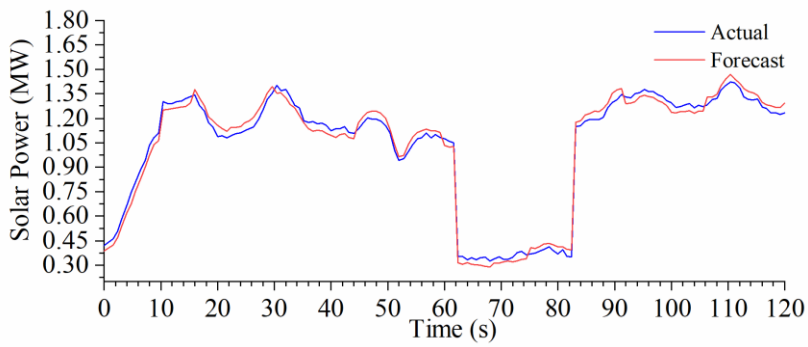

Figure 3.3. Solar power variation curves.

The total load and system net load (i.e, the total load minus the PV output) profiles for the simulations are illustrated in Figure 3.4.

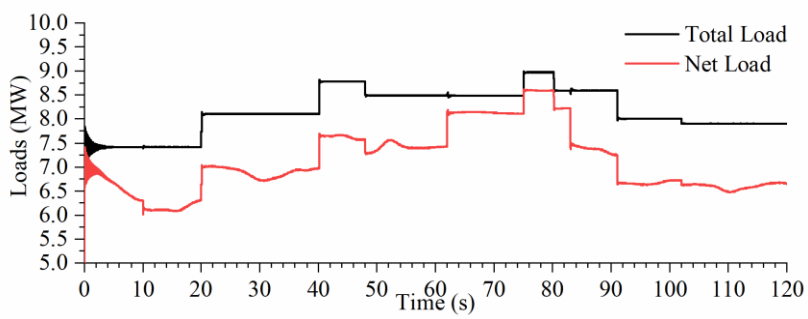

Figure 3.4. Actual total load and net load curves.

3.6.2 MPC Performance Evaluation

Case studies are conducted to evaluate the performance of the proposed MPC controller by comparing the transient response and the frequency regulation capacity of the proposed MPC controller with decentralized local PI controllers. In addition, the case where $T_c = 3$ sec is also studied to investigate the effect of control intervals on MPC performance. For the three cases, the AC-OPF and the primary droop controllers remain the same. The control parameters in the two methods are carefully tuned in the MPC Toolbox and the Control System Toolbox of MATLAB, respectively. For comparison purposes, the MPC controllers in the two cases utilize the same set of parameters and forecast PV power curve except for the difference in control intervals. As highly oscillatory responses may arise due to the windup of the integrator, which keeps integrating the tracking error even when the output saturates, clamping technique is adopted for PI [119] to combat the possible negative effects. The active power outputs of the SGs at buses 1 and 2 regulated by MPC and PI controllers are given in Figure 3.5 comparing with the references from the AC-OPF.

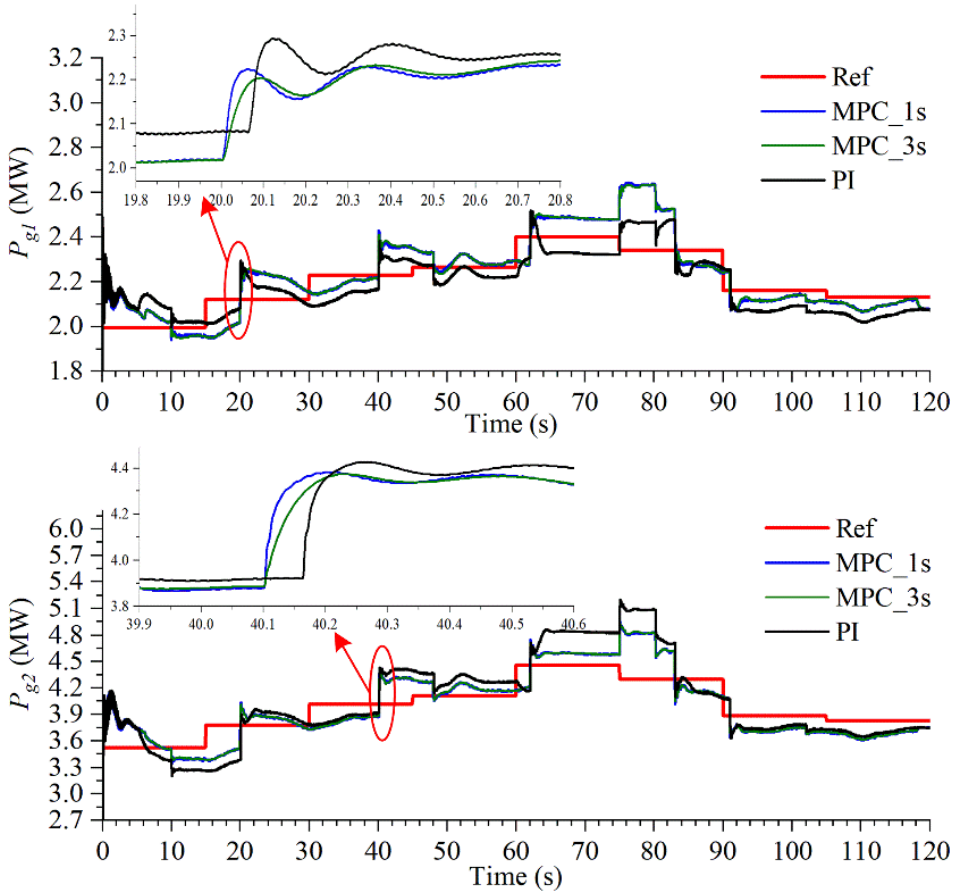

Figure 3.5. Power tracking for SGs at buses 1 and 2.

Figure 3.5 demonstrates that the MPC controller with $T_c = 3$ sec generates slightly smoother power outputs than the one with $T_c = 1$ sec due to less frequent power change settings and that they both achieve faster dynamic responses than the PI controller, as shown in the enlarged graphs. Both MPC and PI controllers closely track the reference power dispatch signals from AC-OPF with some tracking errors as a result of imperfect forecasting and controller performance. It is observed that the MPC controllers do not consistently outperform the PI controller. For instance, while the MPC controllers track the active power reference of SG at bus 2 from t = 45 sec to t = 60 sec better, the PI controller

beats the MPC controllers from t = 15 sec to t = 30 sec for the SG at bus 1. Thus, their power tracking capabilities are further compared in terms of total operating costs, which are determined by the quadratic cost function, as displayed in Figure 3.6. Using the mean bias error (MBE) metric, it is found that the proposed MPC method in the case of $T_c = 1$ sec and $T_c = 3$ sec results in cost savings of \$13.62/hour and \$12.37/hour, compared with PI control, respectively. The average operating cost difference between the MPC controller with $T_c = 1$ sec and the PI controller is very high (\$32.85/hour) when the system experiences the highest net load. This is because forecasting information is integrated into the MPC prediction model, allowing the MPC controllers to generate efficient control signals that can lead to more economic operation despite system uncertainties.

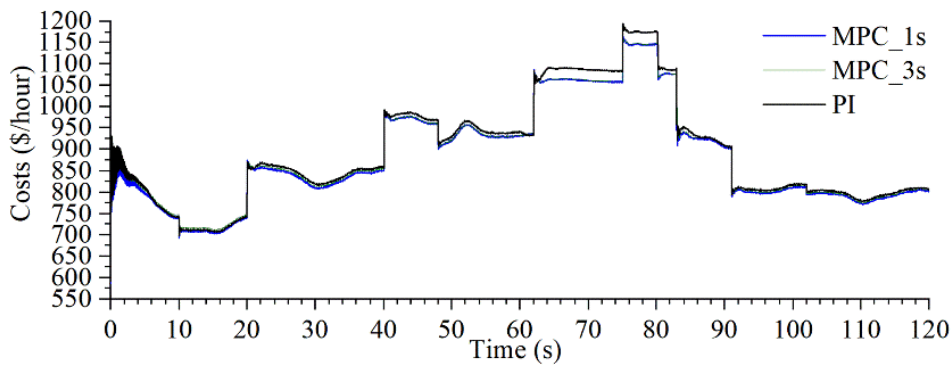

Figure 3.6. Total operating costs.

The microgrid frequencies measured at bus 6 are presented in Figure 3.7. In comparison with the PI controllers, the proposed MPC controller in two control interval settings is able to regulate the microgrid frequency well within the range of 59.4- 60.6 Hz and always maintain the microgrid frequency closer to the nominal frequency.

Quantitatively, the mean absolute errors (MAEs) of the frequencies with respect to 60 Hz for MPC with $T_c = 1$ sec and $T_c = 3$ sec, and PI controllers are 0.1027Hz, 0.1082Hz, and 0.1707Hz, respectively. The main reason for such performance improvement lies in the fact that frequency is rigorously constrained in the MPC problem. Additionally, smaller frequency fluctuations, particularly at transients, are observed from the zoomed-in graph when the MPC employs a smaller control interval, enabling the controller to react faster to mitigate the disturbances from solar PV and loads.

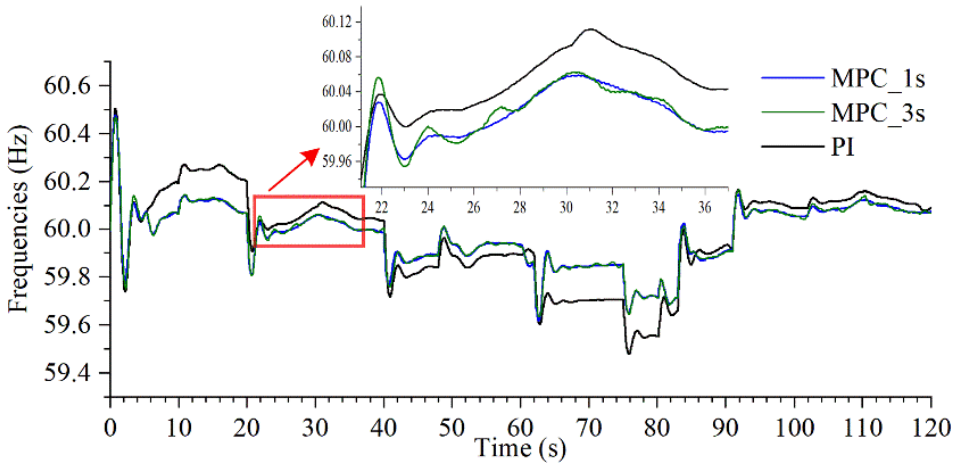

Figure 3.7. System frequencies measured at bus 6.

Other results related to the case of MPC with $T_c = 1$ sec are presented in the rest of this study since the MPC with $T_c = 3$ sec shows similar results. Voltage regulation of the simulated microgrid system is taken care of by the SGs' excitation systems and the STATCOMs. It is observed that voltages at all buses of the simulated microgrid system are well regulated within the typical permissible range of 0.95 pu to 1.05 pu. The sample bus

voltages are illustrated in Figure 3.8.

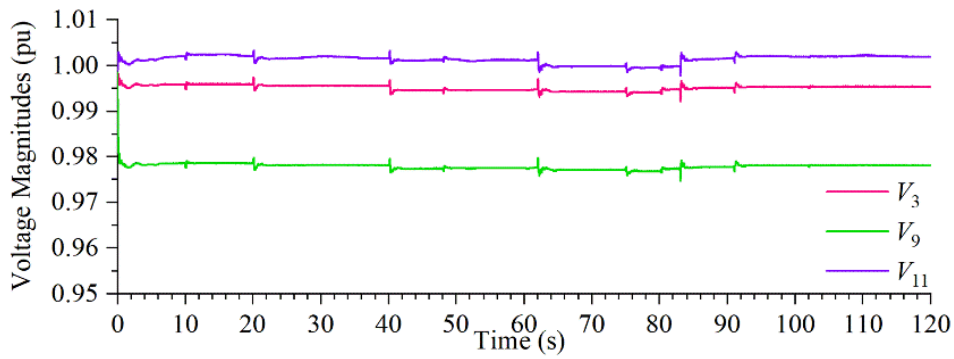

Figure 3.8. Voltage magnitudes at selected buses.

The MPC controller is dynamically executed, and eventually brings the system towards a new steady state following any transient, as evidenced in the above case studies. Figure 3.9 illustrates the power change settings (P_c), generated by the MPC controller every 1 sec and sent to the primary droop controllers. It is demonstrated that such control signals, during the transient states, are adjusted more aggressively as the operating conditions vary greatly, particularly when the PV plunges at $t = 62$ sec. Even at the steady states, adjustment is still being made as a result of the time-varying operating points. Throughout the entire simulation, no time-out error was experienced. However, some identical control signals over multiple consecutive time steps were observed at the transient states, indicating possible infeasibilities of MPC during these control intervals, which might be attributed to the large model mismatch at transients due to linear approximation.

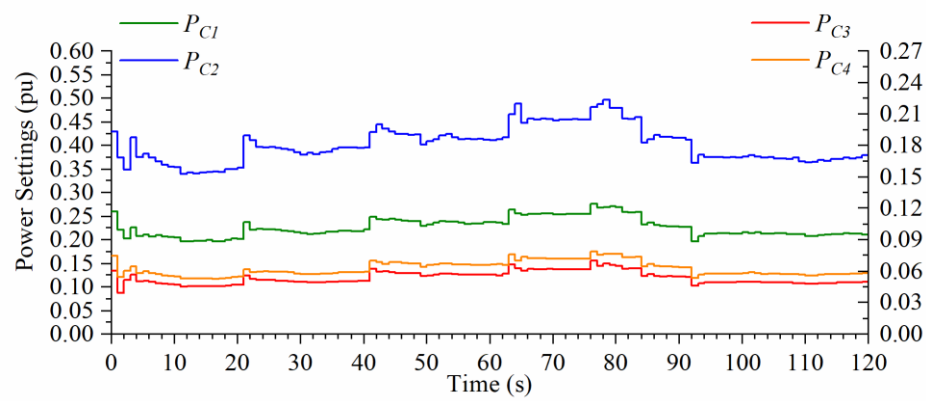

Figure 3.9. Power change settings to each SG.

3.6.3 State Estimation Evaluation

The performance of the proposed secondary MPC controller depends heavily on the state estimation accuracy. For SG 4, the estimated states $\delta', \omega, E_{fd}, T_M$ from the ULISE and their recorded actual signals are presented in Figure 3.10, which shows that the estimated system states using the proposed ULISE agree closely with the actual signals sampled from the numerical simulation.

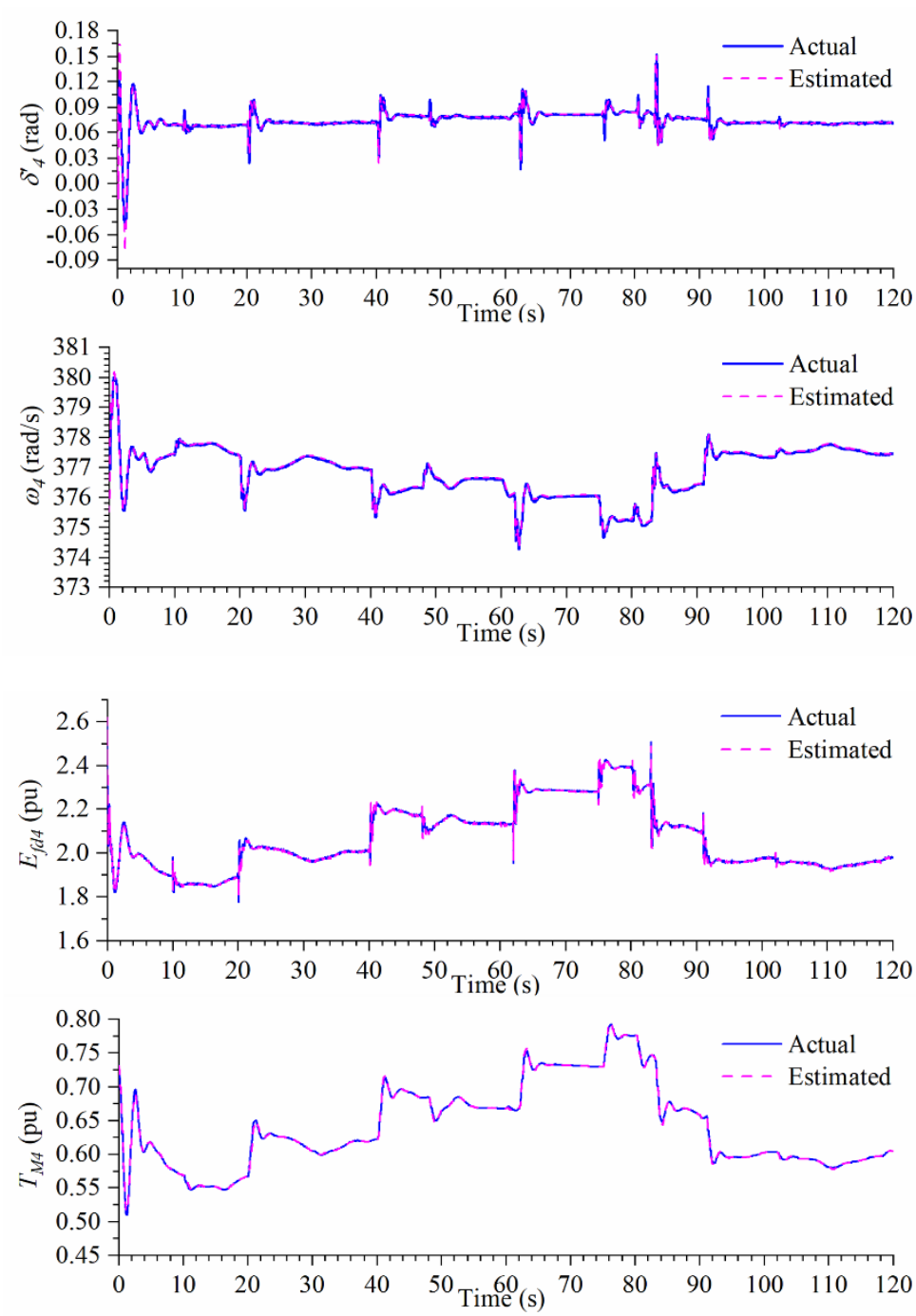

Figure 3.10. State estimation results for the SG at bus 4.

However, relatively large estimation errors are observed during the transients.

These errors are mainly attributed to the low-order approximation in the linear system model, as well as the simplified system component models used for state estimation. Nevertheless, these estimates converge to the real values accurately in only a few seconds. Furthermore, over the entire course of time-domain simulations, the strong detectability of the linearized microgrid system was constantly checked, without which unbiased state and input estimates cannot be obtained even in the absence of stochastic noise [113]. During the transient states, it was also noticed that there are a few cases where the strong detectability is not satisfied. That is, the ULISE generates sub-optimal estimates in these scenarios. This outcome is also likely due to the linear approximation of a nonlinear system.

3.6.4 Anomaly Detection Using the ULISE

To testify to the performance of the ULISE in detecting the system anomaly, a scenario where an attacker purposely alters the control signals sent to SGs' primary controllers to disrupt the dynamic performance of the control system is constructed. At t = 104.2 sec, a ramp signal with a slope of 0.01 is deliberately superimposed to P_C of SG at bus 4 over the communication link. As shown in Figure 3.11, ULISE estimates the received control signal, which is far away from the one calculated and sent by the MCP controller. The control signal is supposed to be fixed within the 104th second, while the estimate turns out to be a monotonically increasing signal. This function enables us to realize the existence of anomalies and to find alternative ways to enhance control. At t = 105.5 sec, a scenario was simulated where a mitigation scheme is initiated to tentatively disable all the communication links, and the local power settings are henceforth held identical as the values at that time instant. In other words, all SGs tentatively operate only in droop mode.

The curves in Figure 3.11 drop to zero after t = 105.5 sec, because the MPC controller and the ULISE are no longer operative. Other mitigation schemes such as resending the control signals via another communication channel could also be implemented.

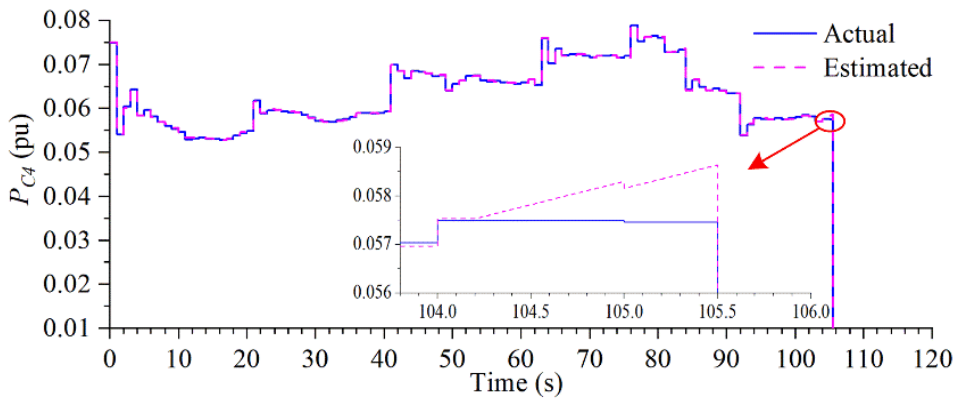

Figure 3.11. Power change setting of the SG at bus 4 under abnormal condition.

Figure 3.12 shows the rotor angular velocity and the active power output of SG at bus 4 with and without the anomaly. Since the MPC controller is no longer operational after t = 105.5 sec, the rotor angular velocity and the active power output tend to converge to new values dictated only by the speed-droop characteristics.

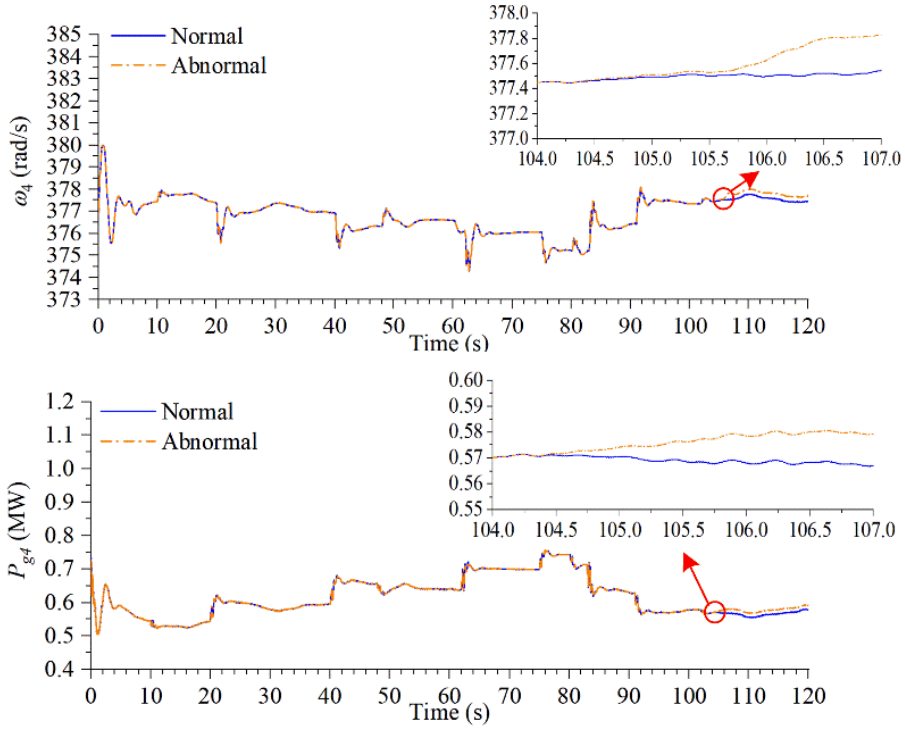

Figure 3.12. Rotor angular velocity and active power output of the SG at bus 4.

3.7 Conclusion

In this chapter, an enhanced predictive hierarchical power management framework for islanded microgrids has been proposed, implemented, and evaluated in a simulated distribution network. A centralized linear MPC secondary controller is designed for microgrid system frequency regulation and active power control. Simulation results have demonstrated its consistent control performance, amid system uncertainties due to renewable generations and loads. A ULISE in a UMV sense is proposed to simultaneously estimate the system states with high precision and the received control signals for enhanced MPC performance. Compared with the decentralized PI controllers with well-tuned

parameters, the proposed MPC controller not only brings superior frequency regulation capability but also reduces the microgrid system operating costs.

Chapter 4

Decentralized Control of DC Power Grids

4.1 Introduction

This chapter presents the modeling and decentralized coordinated control of a PV-BESS system for islanded DC power grids. PVs can switch between the *V-P* droop mode and the MPPT mode adaptively based on the measured DC bus voltages, reducing the impact on system operation. In addition, due to the converters' advantages over other DC-DC topologies, such as galvanic isolation, high power density, and high-power conversion efficiency, the bidirectional DAB DC-DC converters are used to interface BESSs with a nanogrid. The DAB's operating principle will be introduced briefly. A SoC-based droop control method for the BESSs is also proposed to prevent battery overcharging/discharging. The PVs and BESSs are coordinated in a communication-less manner to maintain load balancing and to regulate the common DC bus voltage with reduced control complexity.

4.2 Operating Principle of DAB Converters

The schematic diagram of a DAB DC-DC converter is shown in Figure 4.1. The electric circuit consists of two H-bridges and a high-frequency transformer. This transformer provides galvanic isolation and energy storage through the winding leakage inductances on both sides (which have been referred to and lumped as L_t on the primary winding in Figure 4.1). At times, resonant capacitors are also connected in parallel with each switch-diode pair to enable zero voltage switching (ZVS) for higher efficiency.

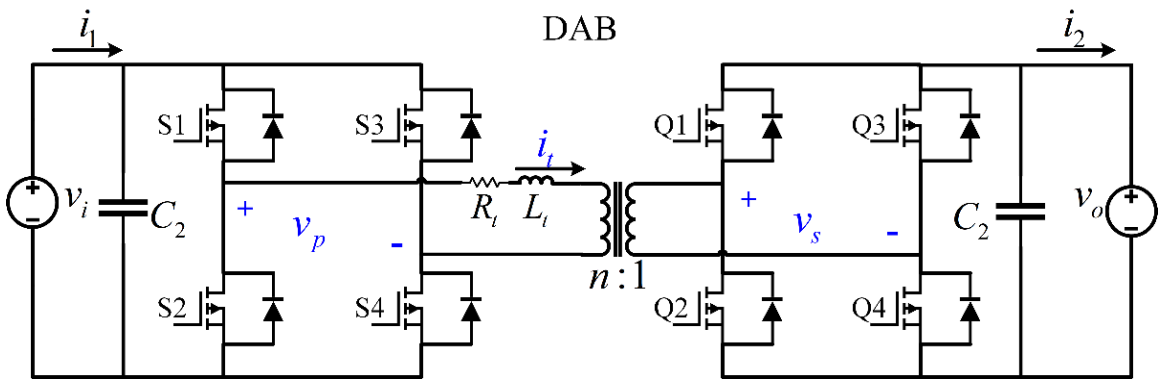

Figure 4.1. Topology of a DAB DC-DC converter.

The DAB converter can be controlled by the phase shift ϕ between the two H bridges, the duty cycles of switching devices, or the switching frequency. Among them, the phase-shift control is the most popular scheme for its simplicity [120]. Conventional phase-shift control can be further classified as single-phase-shift, extended-phase-shift, dual-phase-shift, and triple-phase-shift. The control flexibility increases with an increase in the control degrees of freedom, but at the cost of higher control complexity. In this work, the single-phase-shift scheme is chosen due to its simplicity and effectiveness [121]. Under this scheme, the control signals of the two H-bridges in Fig. 4.1 are square waves with a constant duty cycle of 50%. Specifically, switches S1 and S4 are simultaneously on only for the first half switching period, while S2 and S3 are on for the second half period. Therefore, the terminal voltage on the primary side of the transformer is

$$v_p(t) = s_1(t)v_i$$

$$s_1(t) = \begin{cases} 1, & 0 \le t < \frac{T_{sw}}{2} \\ -1, & \frac{T_{sw}}{2} \le t < T_{sw} \end{cases} \tag{4.1}$$

where T_{sw} is the switching period. Likewise, the terminal voltage on the secondary side:

$$v_s(t) = s_2(t)v_o$$
$$s_2(t) = \begin{cases} 1, & \frac{dT_{sw}}{2} \leq t < \frac{T_{sw}}{2} + \frac{dT_{sw}}{2} \\ -1, & \text{otherwise} \end{cases} \tag{4.2}$$

where d is defined as the phase shift ratio $\frac{\phi}{\pi}$ $(-1 \leq d \leq 1)$, and ϕ is the phase shift in radians.

Without loss of generally, it is assumed $v_i \geq nv_o$; n is the turns ratio of the high-frequency transformer. A pictorial illustration of the relevant waveforms during one switching period when the lumped leakage resistance R_t is ignored is provided in Figure 4.2. v_t is the voltage drop across L_t.

In light of the symmetry of the circuit configuration, the average transferred power $P = \int_0^{T_{sw}} v_p(t)\, i_t(t)$ is calculated as

$$P = \frac{n \cdot V_i \cdot V_o \cdot d}{2 \cdot f_{sw} \cdot L_t}(1 - d) \tag{4.3}$$

where V_i and V_o are the terminal voltage magnitudes on the primary and secondary windings, respectively. The same analysis applies to the case when the power is transmitted from the secondary side to the primary side. Hence, they are expressed in a unified way [122]:

$$P = \frac{n \cdot V_i \cdot V_o \cdot d}{2 \cdot f_{sw} \cdot L_t}(1 - |d|) \tag{4.4}$$

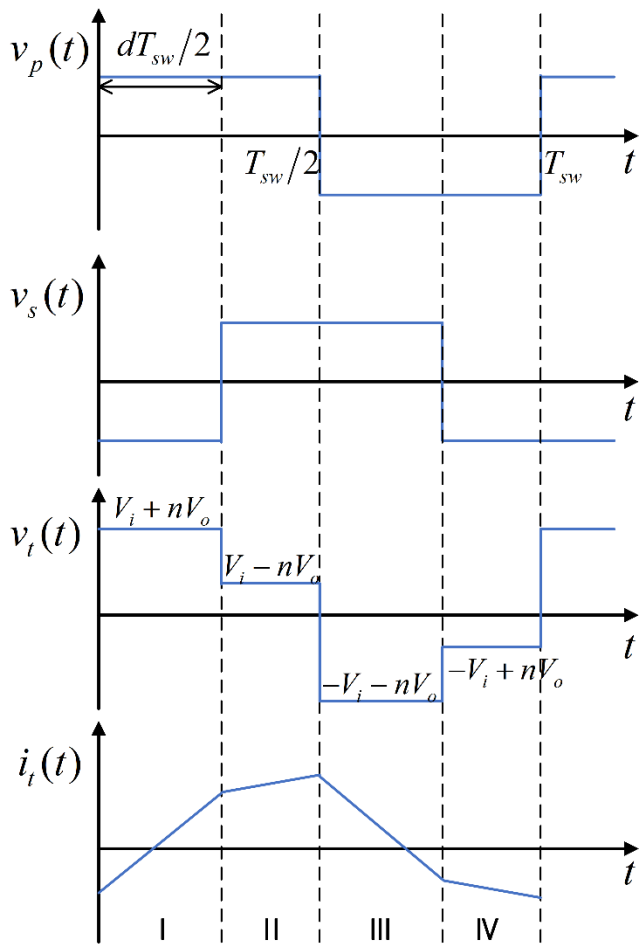

Figure 4.2. Waveforms in one switching cycle.

Eq. (4.4) shows the power to be transferred can be controlled by regulating the phase shift ratio or the phase shift. According to (4.4), the relationship between the transferred power and the phase shift ratio under the single-phase-shift scheme is plotted as Figure 4.3.

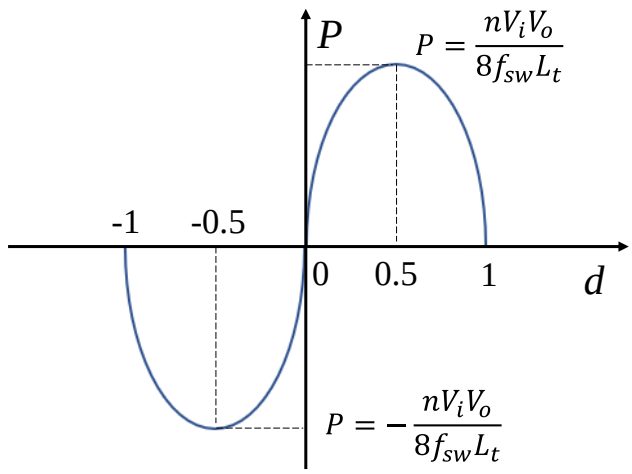

Figure 4.3. Power curve with respect to the phase shift ratio.

When the power is transmitted from the primary to the secondary side (i.e., $0 \leq d \leq 1$), the power reaches its peak at $d = 0.5$, corresponding to $\phi = \frac{\pi}{2}$. Furthermore, the reverse peak power is attained at $\phi = -\frac{\pi}{2}$.

4.3 Proposed Control Strategy

The concept of the DC bus voltage regulation is based on droop control. The illustrations of the *V-P* droop characteristics for the PV and BESS units are given in Figure 4.4.

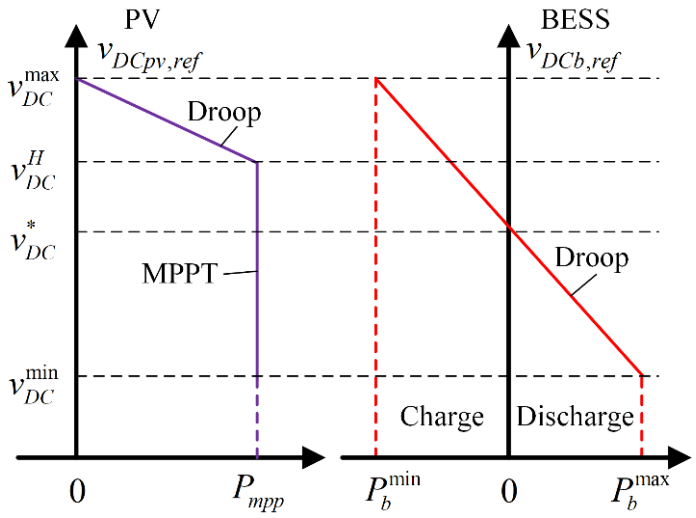

Figure 4.4. V-P droop curves of a PV unit and a BESS unit.

v_{DC}^{*} is the nominal voltage of the common DC bus, while $\left[v_{DC}^{\min}, v_{DC}^{\max}\right]$ is the permissible range of the common DC bus voltage. When the DC bus voltage is high enough (in the range from v_{DC}^{H} to $v_{DC}^{\max}$), the PV units are supposed to limit their power outputs and operate in the droop mode. Meanwhile, the batteries should absorb excess PV generation to bring down the DC bus voltage. Under this operating condition, PVs and BESSs maintain the power balance and regulate the common DC bus voltage together. However, when the DC bus voltage drops below v_{DC}^{H}, the PVs seamlessly transition to the MPPT mode for full utilization of the solar power at the maximum power point (MPP), i.e., P_{mpp}. Consequently, the BESSs become the only power sources to regulate the common DC bus voltage. It is also noted that, apart from the charging/discharging power limits $P_b^{\min}$ and $P_b^{\max}$, the batteries are subject to SoC limits. To preserve battery life, the information of SoCs is integrated into the BESS droop curves to mitigate overcharging and over-discharging issues. The decentralized control strategies proposed for the PVs and the

BESSs will be elaborated in the following subsections.

4.3.1 Adaptive Control of PVs

As shown in Figure 4.5, a DC-DC boost converter is employed to interface between the PV panel and the DC nanogrid. The cascade control structure consists of three control loops. The *V-P* droop characteristic curve in Figure 4.4 is realized in the outer control loop, which generates the DC bus voltage reference $v_{DCpv,ref}$. A first-order low-pass filter is also utilized to suppress fluctuation in solar power and to improve system stability. P_{pv} is filtered solar power. The voltage reference for a PV unit is given by:

$$v_{DCpv,ref} = v_{DC}^{max} - R_{d,pv}P_{pv} \tag{4.5}$$

The droop coefficient $R_{d,pv}$ is defined as:

$$R_{d,pv} = \frac{P_{mpp}}{v_{DC}^{max} - v_{DC}^{H}} \tag{4.6}$$

The intermediate DC bus voltage control loop then acts on $v_{DCpv,ref}$ and produces the PV voltage reference $v_{pv,ref}$ for the inner control loop via a proportional-integral (PI) controller with integral clamping and a mode switch block. The duty cycle *D* to the boost converter is generated in the inner voltage loop using another PI controller. In the proposed control scheme, the PV panel is regulated on the left side of the MPP of its *P-V* characteristic curve in Figure 4.6 to facilitate mode switch. The MPP can be readily estimated by combining off-line calculation of PV model parameters from specification sheets with real-time readings of temperature and solar irradiance sensors [107]. In addition, the mode switch block enables the seamless transition between MPPT and droop modes.

When the output of the intermediate control loop varies within the range specified by 0 and v_{mpp}, $v_{pv,ref}$ equals this output, and the PV unit works in the droop mode accordingly. However, the output will increase and $v_{pv,ref}$ will saturate at v_{mpp} once the DC bus voltage drops greatly, thus naturally making the PV unit operate in the MPPT mode.

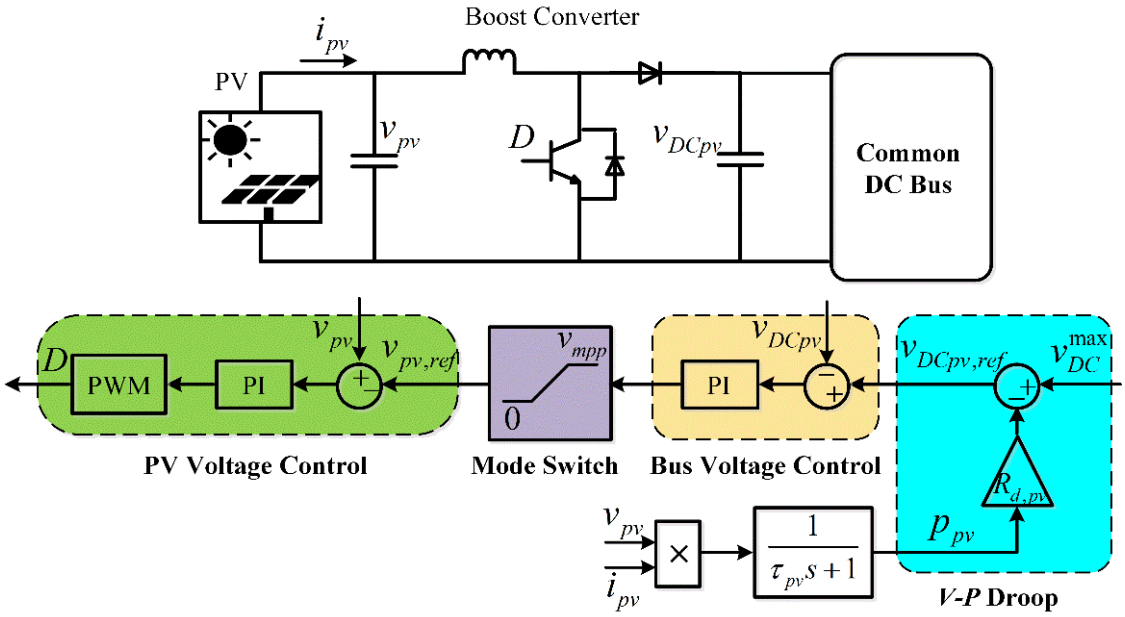

Figure 4.5. Control diagram of a PV unit.

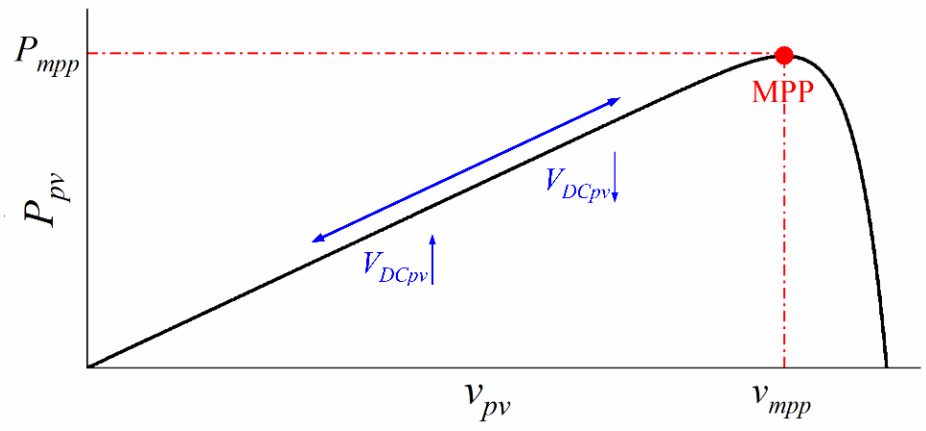

Figure 4.6. P-V characteristic curve of a PV panel.

4.3.2 Adaptive Droop Control of BESSs

Bidirectional DC-DC converters should be employed to meet the bidirectional power flow requirements of the BESSs. In Figure 4.7, a DAB converter connects a BESS unit to the common DC bus.

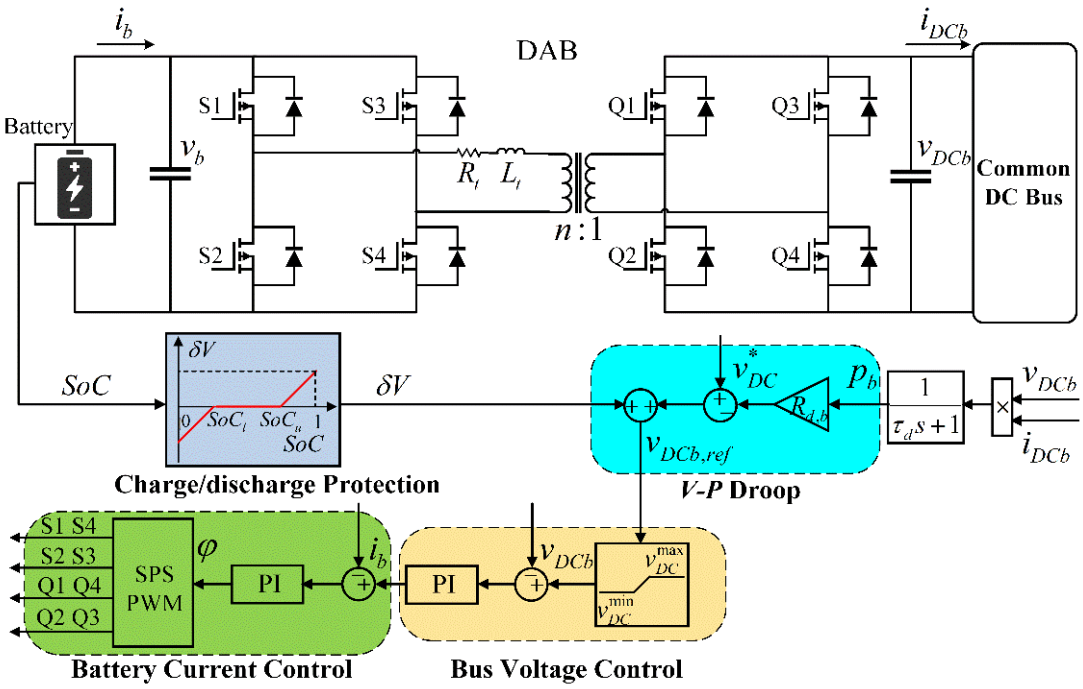

Figure 4.7. Control diagram of a BESS unit.

The proposed cascaded control structure consists of three control loops. The outer control loop implements the *V-P* droop characteristic shown in Figure 4.4 and also takes account of an additional voltage correction term δV:

$$v_{DCb,ref} = v_{DC}^{*} - R_{d,b}P_b + \delta V \tag{4.7}$$

where the droop coefficient $R_{d,b}$ is defined as:

$$R_{d,b} = \frac{v_{DC}^{max} - v_{DC}^{min}}{P_b^{max} - P_b^{min}} \tag{4.8}$$

The charge/discharge protection module provides the adjustment of δV to the DC bus voltage reference based on the real-time SoC estimate, which can be obtained using

several methods [123]. In this work, the commonly used the coulomb counting method is employed:

$$SoC(t_2) = SoC(t_1) - \frac{\eta}{C_b}\int_{t_1}^{t_2} i_b(\tau)d\tau \tag{4.9}$$

where $\mathrm{SoC}(t_1)$ and $\mathrm{SoC}(t_2)$ are the SoCs at time instants t_1 and t_2 respectively. C_b is the battery rated capacity, i_b is the discharging current, and η is the coulombic efficiency.

Then the modified voltage reference $v_{DCb,ref}$ to the intermediate bus voltage control loop is bounded between $v_{DC}^{\min}$ and $v_{DC}^{\max}$ for reliable operation. The phase shift between the control signals is generated in the inner battery current control loop via a PI controller.

It should be noted that the proposed SoC-based adaptive control is conveniently embedded into the BESS *V-P* droop curve by implementing the charge/discharge protection module shown in Figure 4.7. To identify the battery overcharge/over-discharge statuses, the researcher denotes the upper and lower thresholds of SoC as SoC_u and SoC_l, respectively. The protection mechanism is elaborated in the following:

$$\delta V = \begin{cases} R_l(SoC - SoC_l), & SoC \in [0, SoC_l) \\ 0, & SoC \in [SoC_l, SoC_u] \\ R_u(SoC - SoC_u), & SoC \in (SoC_u, 1] \end{cases} \tag{4.10}$$

where $R_l = \frac{v_{dc}^* - v_{dc}^{min}}{SoC_l}$ and $R_u = \frac{v_{dc}^{max} - v_{dc}^*}{1 - SoC_u}$.

When the SoC lies within the normal range $[SoC_l, SoC_u]$, charge/discharge protection is unnecessary; hence $\delta V = 0$. However, the SoC-based adaptive control is

enabled when the measured SoC falls outside of this range. The dynamic processes are illustrated in Figure 4.8. If the battery is discharging and the SoC decreases below SoC_l, the droop curve then dynamically shifts downwards by δV, lowering the DC bus voltage reference. Thus, the battery will decrease its discharging power along the translated droop curve until a new steady state is reached. Over-discharging is mitigated. The trajectory of the changing operating point is illustrated by the red arrows in the left subplot of Figure 4.8. Likewise, if the battery is charging and the SoC increases above SoC_u, the droop curve then shifts upwards by δV, as a way of alleviating the over-charging. In both cases, the battery power output is regulated by the modified voltage reference. Moreover, if there are multiple BESSs, their SoCs can tend towards a balance (i.e., similar SoC levels) over time, since the modified voltage reference of the BESS unit with a high SoC is higher and that of the BESS unit with a low SoC is also lower.

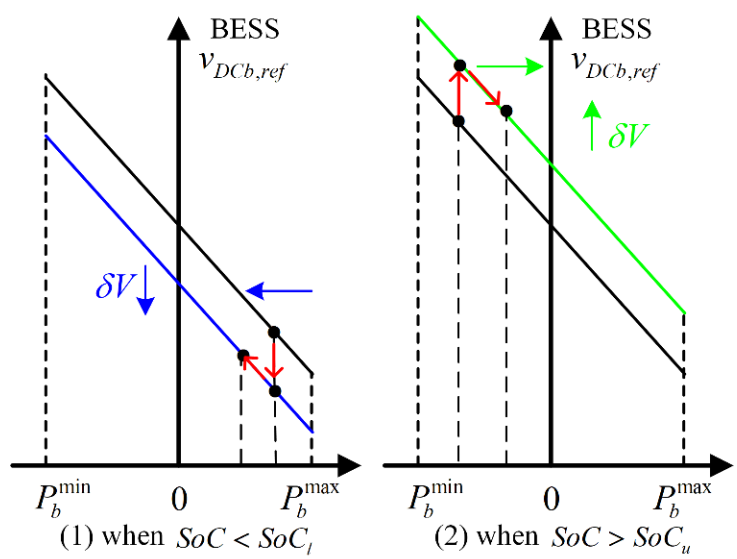

Figure 4.8. Curves of SoC-based droop control in the two cases.

The above proposed controls of PV units and BESS units are implemented at the local level. They are fully decentralized and only require the measurement of DC bus voltages, which ensures the plug-and-play function. Besides, at least one type of distributed generators is in place to stabilize the common DC bus voltage. Hence, system reliability can be improved and control complexity is also decreased.

4.4 Simulation Results

4.4.1 Simulation Setup

The dynamic performance of the proposed control strategy is validated using MATLAB/Simulink under varying DC loading and solar irradiance conditions. Figure 4.9 displays the islanded DC nanogrid test system, which consists of one PV panel, two BESSs, one static load, and one dynamic load.

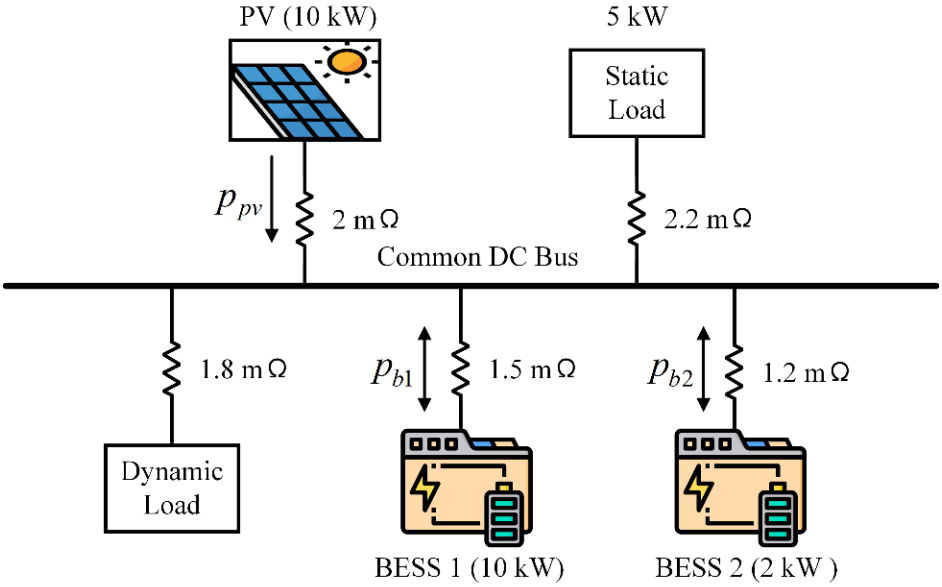

Figure 4.9. Topology of the islanded DC nanogrid test system.

In the test system, the nominal value (v_{DC}^{*}) of the common DC bus voltage is 380 V, while its permissible limits $v_{DC}^{\max}$ and $v_{DC}^{\min}$ are 405 V and 355 V, respectively. The high voltage value v_{DC}^{H} is 390 V. For simplicity, the coulombic efficiency of 100% is assumed for the BESS units. SoC_u is set as 0.8, while SoC_l is 0.3. Furthermore, the initial SoCs of BESS 1 and BESS 2 are set as 0.7995 and 0.3 respectively to demonstrate the effectiveness of the proposed charge/discharge protection mechanism. Since the battery dynamics are usually slow, the coefficients R_l and R_u used in (4.10) are also augmented by 400 times to strengthen the effectiveness for limited simulation time. For the PV unit, its cell temperature is assumed to be 25 °C throughout the simulation. Figure 4.10 shows the solar irradiance variation, while Figure 4.11 depicts the dynamic load change. Controller parameters were obtained from small-signal stability analysis and are provided in the Appendix along with other system parameters.

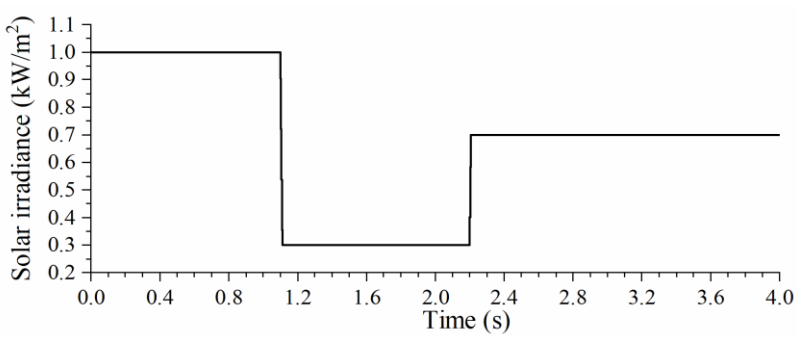

Figure 4.10. Solar irradiance curve.

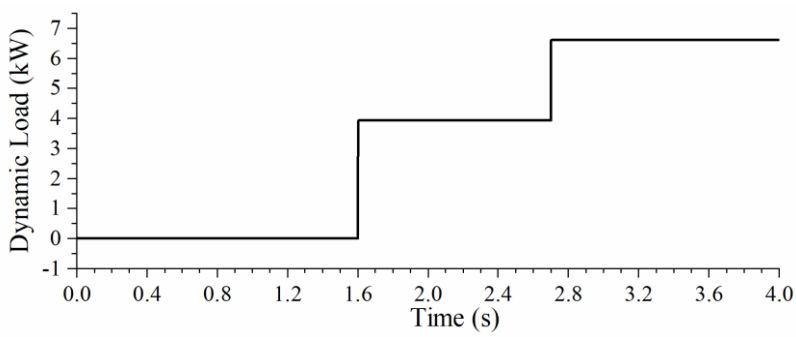

Figure 4.11. Dynamic load curve.

Table 4.1

Parameters of the BESS Units

Parameters	**BESS 1**	**BESS 2**
Battery nominal voltage	51.6 V	51.2 V
Battery's P_{bmax}	8 kW	1.5 kW
Battery's P_{bmin}	-8 kW	-1.5 kW
DAB rated power output	10 kW	2 kW
Transformer's R_t	2 mΩ	5 mΩ
Transformer's L_t	2.85 μH	14.25 uH
Transformer's turns ratio n	1/8	1/8
Switching frequency f_{sw}	10 kHz	10 kHz
Droop coefficient $R_{d,b}$	3.1 V/kW	16.7 V/kW
Low-pass filter time constant τ_d	0.001 sec	0.001 sec
Bus voltage controller	8.57 + 2760/s	4.52 + 1310/s
Battery current controller	11.9/s	59.6/s

Table 4.2

Parameters of the PV Unit

Parameters	PV
v_{mpp} in Standard Test Conditions	122.8 V
P_{mpp} in Standard Test Conditions	9.958 kW
Boost converter's inductance	2.5 mH
Boost converter's output capacitance	1 mF
Low-pass filter time constant τ_{pv}	0.002 sec
Bus voltage controller	0.21 + 107/s
PV voltage controller	0.69 + 50/s

4.4.2 Simulation Results

The DC bus voltages measured at the output terminals of the three distributed generators are presented in Figure 4.12. It can be observed that the voltages almost coincide and that they are well regulated within the permissible voltage range. Initially, the common DC bus voltage stays at around 391 V, slightly above v_{DC}^{H}. Hence, the PV unit limits its power output and generates 9.217 kW as opposed to 9.958 kW at MPPT, as shown in Figure 4.13. Since the common DC bus voltage is high enough, both BESSs operate in the charging mode.

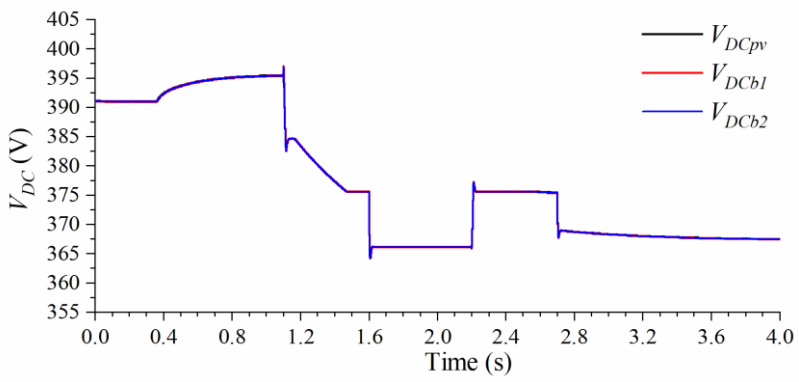

Figure 4.12. DC bus voltages of the BESS and PV units.

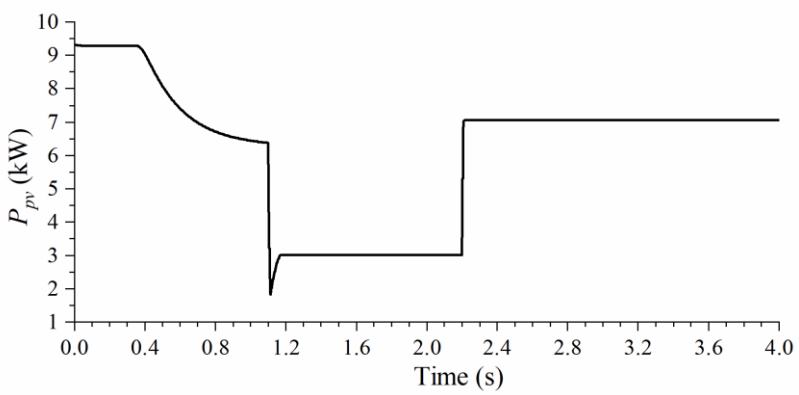

Figure 4.13. Power output of the PV unit.

Figure 4.14 illustrates the power outputs of the two BESSs over the simulation horizon, while Figure 4.15 presents their SoC levels.

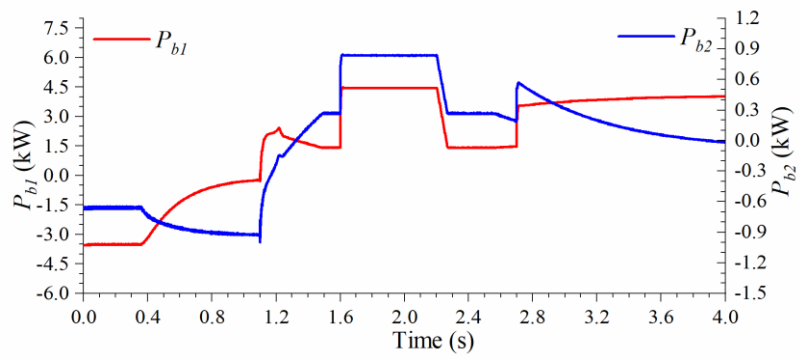

Figure 4.14. Power outputs and BESS 1 and BESS 2.

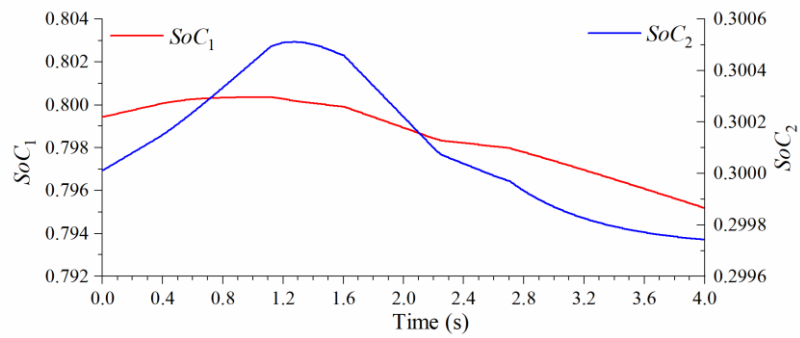

Figure 4.15. SoC levels of BESS 1 and BESS 2.

It can be observed from Fig. 4.14 that the actual active powers shared between the BESS units in the steady states are directly proportional to their battery power ratings. At the beginning, the BESS units are charged at constant powers, thereby absorbing excess solar power in the DC nanogrid. At t = 0.37 sec, the SoC of BESS 1 rises beyond 0.8. Therefore, the charge protection mechanism is triggered, and the voltage reference of BESS 1 is adaptively raised according to (4.10). As a consequence, BESS 1 decreases its charging

power and its SoC starts to experience a much slower increase. Meanwhile, BESS 2 begins to pick up more charging power and its SoC level is still within the normal range. Due to the increase in the DC bus voltage, the PV unit provides less power as per its *V-P* droop characteristic curve, as seen in Figure 4.13. However, the PV unit still participates in voltage regulation along with the BESSs.

The solar irradiance plunges at t = 1.1 sec. As the common DC bus voltage decreases significantly, the PV unit is forced to operate in the MPPT mode after a small transient and yields 3.016 kW at a new steady state. During this process, the two BESS units are discharging and put out more active power to compensate for the instantaneous power imbalance and also to regulate the common DC bus voltage. From t = 1.6 sec to t = 2.2 sec, the DC nanogrid experiences the highest net load (i.e., the total electrical demand minus the solar power generation), which is reflected by the largest decreasing rates of the BESSs' SoC levels. It should be noted that while the solar irradiance increases after t = 2.2 sec, the PV unit still operates in the MPPT mode, delivering the highest solar power available due to the low DC bus voltage. In the meantime, the two BESSs continue discharging to provide power support and voltage regulation. When t = 2.56 sec, the SoC of BESS 2 begins to reduce below 0.3, thus automatically triggering the discharge protection mechanism. As a result, the DC bus voltage reference of BESS 2 is lowered according to (4.10). BESS 2 then generates far less power and sees a slow-down of its SoC decline. On the other hand, BESS 1 still operates within the normal SoC range and fulfils virtually all the electrical demand afterwards. It is possible that both BESSs will hit the lower threshold of SoC and are thus no longer able to power the loads. In this extreme case, load shedding should be performed, which, however, is beyond the scope of this work.

The above simulation results exhibit good dynamic performance of the proposed coordinated control strategy, and the control system is stable. As the DAB topology facilitates the bidirectional power flow of the BESS units, the phase shifts generated by the inner battery current control loop are also presented in Figure 4.16.

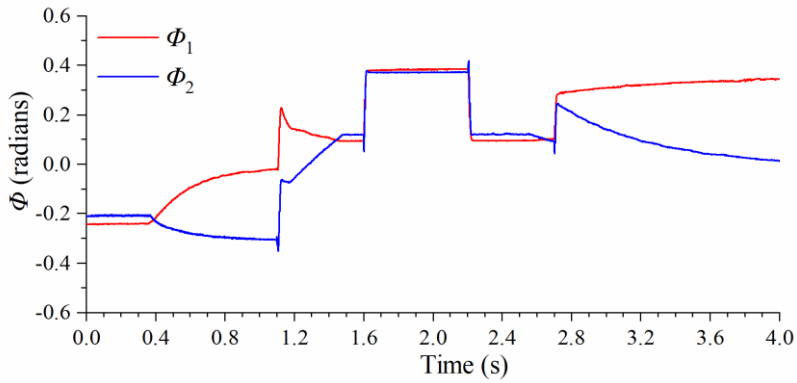

Figure 4.16. Phase shifts generated for BESS 1 and BESS 2.

The sign of the phase shift angles indicates whether the BESSs are in charging or discharging modes. A negative phase shift angle means the charging mode. It can be seen that smooth transitions are achieved between charging and discharging operation modes during the simulation. Interestingly, the curves of the phase shifts are similar to those of the power outputs shown in Figure 4.14. This is because the two BESS units operate with phase shifts far away from the extrema $\pm\frac{\pi}{2}$, which lie in an approximately linear region of the parabolic function (4.4).

4.5 Conclusion

A fully decentralized coordination strategy for controlling the PV-BESS systems in the islanded DC nanogrids has been presented in this chapter. The proposed control strategy relies only on the measurements of local DC bus voltages, thus demanding minimum communication capabilities. The PV unit is able to provide power and regulation support to the DC bus voltage by seamlessly switching between the MPPT mode and the droop mode. In addition, a SoC-based adaptive droop control method is proposed for the BESS units that are interfaced by DAB DC-DC converters to regulate the DC bus voltages. Overcharging and over-discharging protection has been achieved via the proposed SoC-related voltage control. Simulation results based on MATLAB/Simulink have demonstrated good dynamic performance and stability of the proposed coordinated control strategy.

Chapter 5

Data-Driven Transient Stability Evaluation of Active Distribution Networks Dominated by EV Supercharging Stations

5.1 Introduction

Globally, transportation is a major contributor to GHG emissions. In the United States, the transportation sector is responsible for 28% of the GHG emissions and has even overtaken the electric power sector as the nation's largest source of GHG emissions in 2020 [124]. Running on electricity from renewable energy (e.g., solar PV, wind) without direct tailpipe emissions, EVs are viewed as a game changer in terms of achieving carbon neutrality in the transportation sector, improving community air quality, and consequently mitigating the impacts on public health and climate change. The federal government of the United States, as well as many state governments, are actively promoting transportation electrification efforts. For example, New Jersey has set a bold goal of registering 330,000 EVs by 2025 and provided different incentive programs to promote the expansion of EV charging infrastructure [125]. Aside from government financial incentives, the emerging high-power charging technologies aimed at addressing the EV drivers' range anxiety are helping spur EV adoption. The charging power of a Level-3 (DC Fast) charger ranges between 50kW and 350kW, while that of the next-generation DC Ultra-Fast chargers can even reach at least 400kW [126]. However, it is anticipated that the massive influx of EV supercharging stations, which will replace the current gas stations, would strain the existing ADNs and introduce negative impedance characteristics. The transient frequency and/or voltage stabilities of emerging ADNs could be severely weakened. Thus, developing efficient TSE approaches is crucial to ensuring the system situational awareness and stable

operation. The ROAs, as a powerful TSE tool, allow the distribution system operator (DSO) to gain an understanding of the system operating status and to take appropriate control actions. Under this context, the first section of this chapter will present modeling of an emerging DC ADN with high penetration of EV charging loads. Afterwards, the Koopman operator theory will be introduced. Finally, the ROAs of the DC ADN of interest will be estimated using data-driven methods based on the Koopman operator theory. The DSO can manage charging requests based on the estimated ROAs to ensure stable ADN operation.

5.2 DC Active Distribution Network Modeling

In this subsection, a DC ADN is modeled, which has several advantages over its AC counterparts such as higher power conversion efficiencies and lower control complexities [127]. Hence, it becomes ideal for hosting EV supercharging stations. Figure 5.1 illustrates a DC ADN connected to an external AC grid. The modeled ADN comprises a BESS, a solar PV, and a few high-power EV chargers, which represent the key components of future supercharging stations. The rated common DC bus voltage (V_n) of the ADN is designed as 2 kV. The external AC grid and the BESS are responsible for DC voltage regulation and power balancing. Different types of PWM power converters are employed to interface these distributed assets to the common DC bus. The local controls of distributed assets are based on PI control. In what follows, the detailed modeling of each type of distributed assets will be provided.

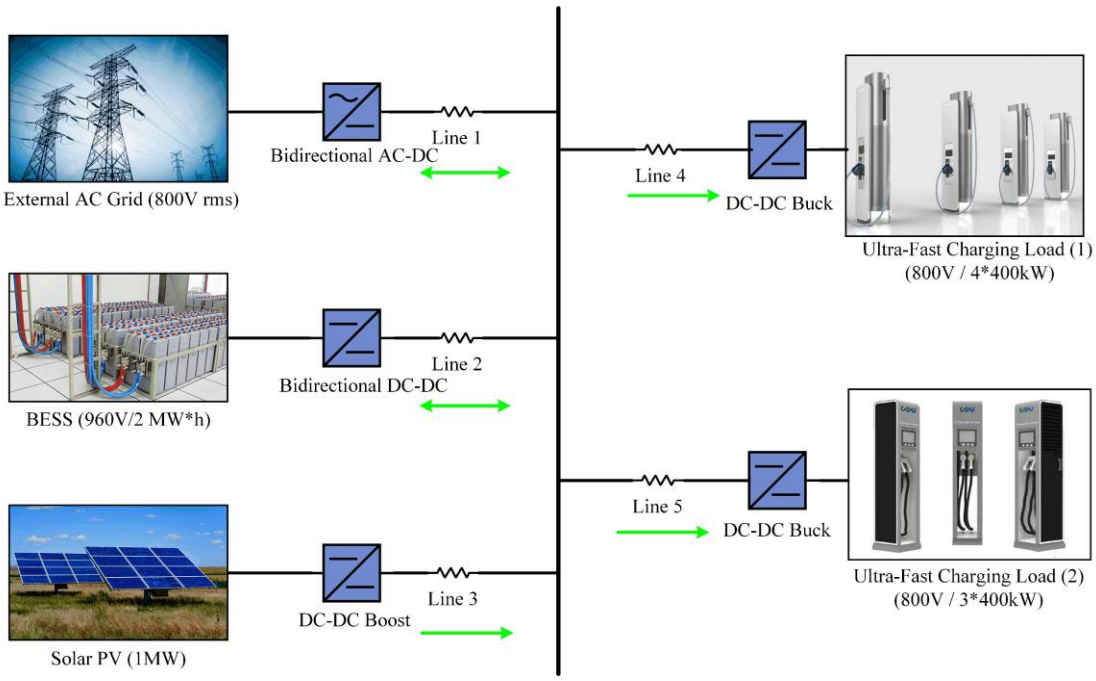

Figure 5.1. The tested DC active distribution network.

5.2.1 Solar PV

A solar PV array in the MPPT mode is interfaced to the DC ADN through a Boost converter, as shown in Figure 5.2.

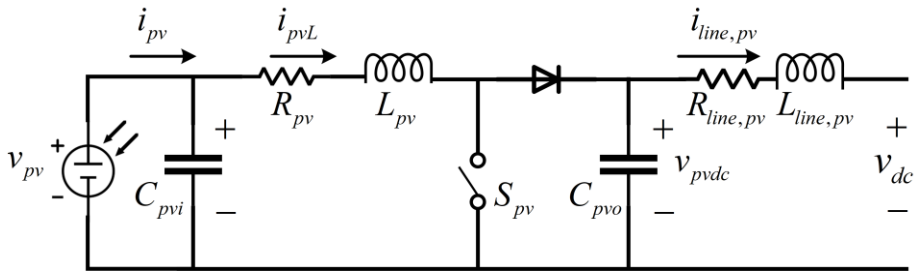

Figure 5.2. Solar PV interfaced by a Boost converter.

The state equations of the Boost converter are obtained:

$$\dot{v}_{pv} = \frac{i_{pv}(v_{pv})}{C_{pvi}} - \frac{i_{pvL}}{C_{pvi}} \tag{5.1}$$

$$\dot{i}_{pvL} = \frac{-R_{pv} \cdot i_{pvL}}{L_{pv}} + \frac{v_{pv}}{L_{pv}} - \frac{[1 - d_{pv}(v_{pv})] \cdot v_{pvdc}}{L_{pv}} \tag{5.2}$$

$$\dot{v}_{pvdc} = \frac{-i_{line,pv}}{C_{pvo}} + \frac{[1 - d_{pv}(v_{pv})] \cdot i_{pvL}}{C_{pvo}} \tag{5.3}$$

$$\dot{i}_{line,pv} = \frac{-R_{line,pv} \cdot i_{line,pv}}{L_{line,pv}} + \frac{v_{pvdc}}{L_{line,pv}} - \frac{v_{dc}}{L_{line,pv}} \tag{5.4}$$

where v_{pv} and i_{pv} are the equivalent output voltage and current of the solar PV, respectively. As v_{pv} and i_{pv} satisfy a transcendental equation [128], i_{pv} is considered as an implicit function of v_{pv}, denoted as $i_{pv}(v_{pv})$. C_{pvi} is the input capacitor, R_{pv} is the internal resistance of the inductor L_{pv}, and v_{pvdc} is the voltage of the DC-link capacitor C_{pvo}. v_{dc} is the common DC bus voltage. The P&O technique is employed for MPPT. $d_{pv}(v_{pv})$ denotes the duty cycle to the switch S_{pv}. It is generated by a local PI controller that regulates v_{pv} to the MPPT voltage [129]. In practice, a BESS can also be added in parallel with this solar PV to form a hybrid system such that the uncertainty in solar irradiance is greatly mitigated. As such, this work assumes small variations in solar irradiance for the modeled solar PV array.

5.2.2 BESS

In Figure 5.3, the bidirectional Buck-Boost converter connects a BESS to the common DC bus of the ADN. This BESS can help reduce peak demand charges and provide ancillary services for improved grid stability.

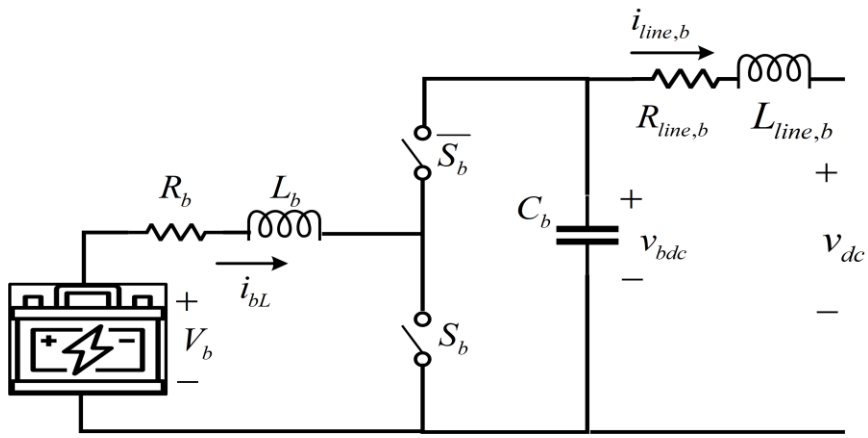

Figure 5.3. BESS interfaced by a bidirectional DC-DC converter.

The dynamics are represented by the following equations:

$$\dot{i_{bL}} = \frac{V_b}{L_b} - \frac{R_b \cdot i_{bL}}{L_b} - \frac{[1 - d_b(v_{bdc},\ i_{bL})] \cdot v_{bdc}}{L_b} \tag{5.5}$$

$$\dot{v}_{bdc} = \frac{-i_{line,b}}{C_b} + \frac{[1 - d_b(v_{bdc},\ i_{bL})] \cdot i_{bL}}{C_b} \tag{5.6}$$

$$\dot{i_{line,b}} = \frac{-R_{line,b} \cdot i_{line,b}}{L_{line,b}} + \frac{v_{bdc}}{L_{line,b}} - \frac{v_{dc}}{L_{line,b}} \tag{5.7}$$

where V_b is the BESS terminal voltage, i_{bL} is the inductor current, v_{bdc} is the voltage of the DC-link capacitor C_b, and $i_{line,b}$ is the output current. $R_{line,b}$ and $L_{line,b}$ are the line resistance and inductance. Since the BESS generally has a large energy capacity and small voltage variations, V_b can be considered as constant. A dual-loop PI control is implemented locally, where the outer loop regulates v_{bdc} to $(V_n - r_b i_{line,b})$ (r_b is the DC droop coefficient) and the inner loop regulates i_{bL}. $d_b(v_{bdc}, i_{bL})$ represents the duty cycle generated by the inner current loop. The upper and lower switches of the power converter are then driven in a complementary manner.

5.2.3 EV Charging Load

Various charging technologies [130] can be utilized to charge EVs, e.g., constant power (CP) mode, constant current (CC) mode, constant voltage (CV) mode, and their combinations. An EV is charged via a Buck converter, as depicted in Figure 5.4.

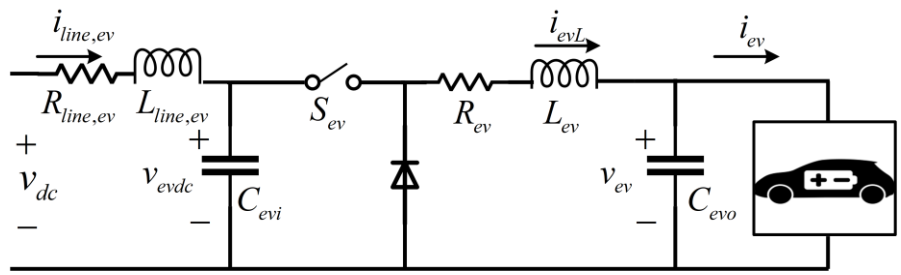

Figure 5.4. EV charged via a Buck converter.

The dynamical model is described as

$$\dot{i}_{line,ev} = \frac{-R_{line,ev} \cdot i_{line,ev}}{L_{line,ev}} + \frac{v_{dc}}{L_{line,ev}} - \frac{v_{evdc}}{L_{line,ev}} \tag{5.8}$$

$$\dot{v}_{evdc} = \frac{i_{line.ev}}{C_{evi}} - \frac{d_{ev}(v_{ev}, i_{evL}) \cdot i_{evL}}{C_{evi}} \tag{5.9}$$

$$\dot{i}_{evL} = \frac{-R_{ev} \cdot i_{evL}}{L_{ev}} - \frac{v_{ev}}{L_{ev}} + \frac{d_{ev}(v_{ev}, i_{evL}) \cdot v_{evdc}}{L_{ev}} \tag{5.10}$$

$$\dot{v}_{ev} = \frac{i_{evL}}{C_{evo}} - \frac{i_{ev}(v_{ev})}{C_{evo}} \tag{5.11}$$

where C_{evi} is the input DC-link capacitor, v_{evdc} is its voltage, i_{evL} is the inductor current, i_{ev} is the charging current, and v_{ev} is the EV battery terminal voltage. Depending on the charging mode, the local controller executes single-loop or dual-loop PI control to generate

the duty cycle d_{ev} for the switch S_{ev}. As v_{ev} and i_{ev} are solely related to each other in the generic battery model [131], i_{ev} is considered as an implicit function of v_{ev}, i.e., $i_{ev}(v_{ev})$.

5.2.4 Grid-Interface Bidirectional AC-DC Converter

The grid-interface converter is implemented using a voltage source converter (VSC) topology. In Figure 5.5, v_{ga}, v_{gb} and v_{gc} are the three-phase AC grid voltages, which are assumed to be balanced. L_g is the inductance of the filter on each phase, and R_g is its internal resistance. In addition, v_{gdc} is the voltage of the DC-link capacitor C_g. The external AC grid can absorb and release DC power to assist in the DC ADN operation.

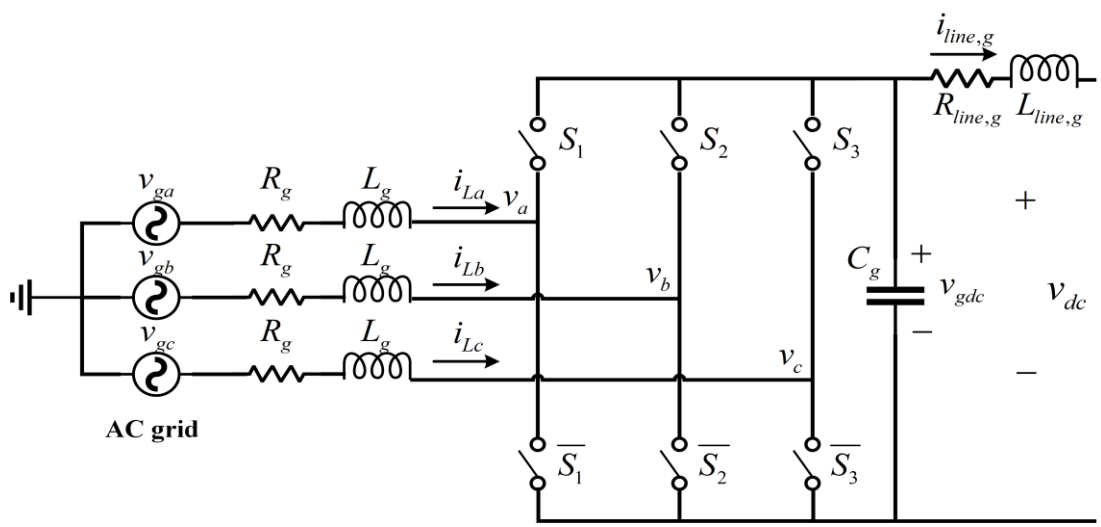

Figure 5.5. AC grid interfaced to the ADN via an AC-DC converter.

In the synchronously rotating *d-q* reference frame, the state equations related to the inductor filters are given:

$$\dot{i_{Ld}} = \omega \cdot i_{Lq} - \frac{R_g \cdot i_{Ld}}{L_g} + \frac{v_{gd}}{L_g} - \frac{m_d(v_{gdc}, i_{Ld}) \cdot v_{gdc}}{2L_g} \tag{5.12}$$

$$\dot{i_{Lq}} = -\omega \cdot i_{Ld} - \frac{R_g \cdot i_{Lq}}{L_g} + \frac{v_{gq}}{L_g} - \frac{m_q(i_{Lq}) \cdot v_{gdc}}{2L_g} \tag{5.13}$$

where v_{gd} and v_{gq} are the grid voltages on the *d*-*q* axes. i_{Ld} and i_{Lq} are the *d*-*q*-axes currents flowing through the inductor filters, while ω is the measured angular frequency of the AC grid. Besides, the dual-loop PI control [132] is implemented. In the outer voltage control loop, v_{gdc} is regulated to its rated value V_n, which provides the *d*-axis current reference. Since no reactive power is delivered, the *q*-axis current reference is set as zero. The inner current control loop tracks the current references and generates the *d*-*q*-axes duty cycles $m_d(v_{gdc}, i_{Ld})$ and $m_q(i_{Lq})$. The dynamics of the DC link can be expressed based on the power balance between the AC and DC sides. In addition, the line current at the output terminal is obtained.

$$\dot{v}_{gdc} = \frac{3(v_{gd} \cdot i_{Ld} + v_{gq} \cdot i_{Lq})}{2C_g \cdot v_{gdc}} - \frac{i_{line,g}}{C_g} \tag{5.14}$$

$$\dot{i_{line,g}} = \frac{-R_{line,g} \cdot i_{line,g}}{L_{line,g}} + \frac{v_{gdc}}{L_{line,g}} - \frac{v_{dc}}{L_{line,g}} \tag{5.15}$$

The dynamics of the AC grid can be represented by the following equations for an equivalent SG [104]:

$$\dot{\omega} = \frac{1}{J}[T_m - \frac{3}{2\omega}(v_{gd} \cdot i_{Ld} + v_{gq} \cdot i_{Lq})] \tag{5.16}$$

$$\dot{T}_m = -\frac{T_m}{\tau_{pm}} + \frac{P_c}{\tau_{pm}} - \frac{1}{r_D \cdot \tau_{pm}} \cdot (\frac{\omega}{\omega_s} - 1) \tag{5.17}$$

where ω is the angular frequency, J is the total moment of inertia of the AC grid, and T_m is the mechanical torque provided by the prime mover. Moreover, τ_{pm} is the time constant of the prime mover, while r_D is the speed droop coefficient. ω_s is the rated angular frequency. P_c is the power change setting typically dispatched by the DSO; in this study, it is determined by a PI controller acting on the error between ω_s and ω.

Because the SG stator terminal voltages are also the grid voltages, v_{gd} and v_{gq} in the above equations can be further expressed as

$$v_{gd} = -R_a \cdot i_{Ld} + \omega \cdot L_{aq} \cdot i_{Lq} + v_{sd} \tag{5.18}$$

$$v_{gq} = -R_a \cdot i_{Lq} - \omega \cdot L_{ad} \cdot i_{Ld} + v_{sq} \tag{5.19}$$

where R_a, L_{ad}, and L_{aq} are the resistance and d-q-axes inductances of the SG stator, respectively. v_{sd} and v_{sq} are the voltages induced on the stator by the excitation system. Since voltage regulation can have fast dynamics, v_{gd} and v_{gq} are considered as constant during the transients.

Without loss of generality, it is assumed that there are n_{pv} solar PVs, n_b BESSs, n_{ev} EV loads in the DC ADN connected to the external AC grid. Therefore, the common DC bus voltage is

$$v_{dc} = \frac{1}{a}\left(\frac{v_{gdc}}{Z_{line,g}} + \sum_{i=1}^{n_{pv}} \frac{v_{pvdc,i}}{Z_{line,pvi}} + \sum_{i=1}^{n_b} \frac{v_{bdc,i}}{R_{line,bi}} + \sum_{i=1}^{n_{ev}} \frac{v_{evdc,i}}{Z_{line,evi}}\right) \tag{5.20}$$

where $a := \frac{1}{Z_{line,g}} + \sum_{i=1}^{n_{pv}} \frac{1}{Z_{line,pvi}} + \sum_{i=1}^{n_b} \frac{1}{Z_{line,bi}} + \sum_{i=1}^{n_{ev}} \frac{1}{Z_{line,evi}}$. Z_{line} denotes a line impedance.

From the above discussions, the overall DC ADN is a nonlinear dynamical system expressed as

$$\dot{\boldsymbol{x}} = \boldsymbol{f}_{adn}(\boldsymbol{x}) \tag{5.21}$$

where the state vector $\boldsymbol{x} := \left[\boldsymbol{x}_{pv}, \boldsymbol{x}_b, \boldsymbol{x}_{ev}, \boldsymbol{x}_{gic}\right]^T$. Specifically,

$\boldsymbol{x}_{pv} := \left[v_{pv,1}, i_{pvL,1}, v_{pvdc,1}, i_{line,pv,1}, \ \dots \ , v_{pv,n_{pv}}, i_{pvL,n_{pv}}, v_{pvdc,n_{pv}}, i_{line,pv,n_{pv}}\right], ,$

$\boldsymbol{x}_b := \left[i_{bL,1}, v_{bdc,1}, i_{line,b,1}, \ \dots \ , i_{bL,n_b}, v_{bdc,n_b}, i_{line,b,n_b}\right], ,$

$\boldsymbol{x}_{ev} := \left[i_{line,ev,1}, v_{evdc,1}, i_{evL,1}, v_{ev,1}, \ \dots \ , i_{line,ev,n_{ev}}, v_{evdc,n_{ev}}, i_{evL,n_{ev}}, v_{ev,n_{ev}}\right],$

and $\boldsymbol{x}_{gic} := \left[i_{Ld}, i_{Lq}, v_{gdc}, i_{line,g}, \omega, T_m\right]$.

Remark 5.1: A priori knowledge of the nominal model parameters of (5.21) is not necessary for a data-driven method. Even if these parameters are available, the actual system is likely to experience deviations from them during operations. Besides, detailed knowledge of the underlying control algorithms is not needed as long as they are related to the system states. However, information on the model structure can reveal the physics of the dynamical system and is thus conducive to collecting data for Koopman operator approximation. Furthermore, knowledge of the normal operating ranges of the ADN dynamic states, which can be estimated empirically or from historical datasets, is helpful in implementing the proposed data-driven ROA estimation approach, as will be presented in later sections.

5.3 Preliminaries of the Koopman Operator Theory

5.3.1 Koopman Operator and Its Data-driven Approximation Using EDMD

Consider a general dynamical system of the following form:

$$\dot{\boldsymbol{x}}(t) = \boldsymbol{f}(\boldsymbol{x}(t)) \tag{5.22}$$

where $\boldsymbol{x}$ evolves in a state space $\boldsymbol{\mathcal{X}} \subset \boldsymbol{\mathcal{R}}^p$. Let $\boldsymbol{F}(\boldsymbol{x}, t)$ be the flow of the continuous-time system (5.22) starting from an initial state $\boldsymbol{x}_0$ when $t \geq 0$, and $g : \boldsymbol{\mathcal{X}} \to \boldsymbol{\mathcal{C}}$ be a measurable function referred to as the observable or the basis function. All observables constitute a (Banach) space of observables $\boldsymbol{\mathcal{F}}$. The Koopman operator $\boldsymbol{K}^t : \boldsymbol{\mathcal{F}} \to \boldsymbol{\mathcal{F}}$ for (5.22) advances an observable based on the evolution of the trajectories in $\boldsymbol{\mathcal{X}}$ such that

$$(\boldsymbol{K}^t g\ )(\boldsymbol{x}) = g \circ \boldsymbol{F}(\boldsymbol{x}, t) \tag{5.23}$$

where $\circ$ represents the pointwise function composition. Since the Koopman operator is linear over its observables, it can be characterized by eigen-decomposition. In general, an eigenfunction $\varphi \in \boldsymbol{\mathcal{F}}$ and its eigenvalue $\lambda \in \boldsymbol{\mathcal{C}}$ satisfy

$$\boldsymbol{K}^t \varphi(\boldsymbol{x}) = exp(\lambda t)\varphi(\boldsymbol{x}) \tag{5.24}$$

$$\frac{d\varphi(\boldsymbol{x}(t))}{dt} = \lambda\varphi(\boldsymbol{x}(t)) \tag{5.25}$$

Additionally, the Koopman operator embeds the finite-dimensional nonlinear dynamics (5.22) to an infinite-dimensional function space, so it is more practical to derive matrix representation of the Koopman operator projected onto a finite-dimensional subspace. The data-driven methods to approximate the spectral properties of this operator

include dynamic mode decomposition (DMD) [133], EDMD [98], generalized Laplace averages [134], deep neural networks (DNNs) [135], etc. Among them, EDMD is most widely applied because it uses an extended basis to capture nonlinearities and only needs one-step iteration. More details on the Koopman operator theory and its data-driven methods can be found in [136].

Let $\boldsymbol{\mathcal{F}}_N \subset \boldsymbol{\mathcal{F}}$ be an N-dimensional Koopman invariant subspace, i.e., $\boldsymbol{K}^t\, g \in \boldsymbol{\mathcal{F}}_N$ for any $g \in \boldsymbol{\mathcal{F}}_N$. When EDMD is applied to (5.22), the basis functions are functions of the states, denoted as $\psi_i(\boldsymbol{x}) \in \boldsymbol{\mathcal{F}}_N$, $i = 1, 2, \ldots, N$. Assuming $(M+1)$ snapshots of data are available from the DC ADN (5.21) at uniform time intervals Δt, the EDMD constructs a finite-dimensional approximation $\widetilde{\boldsymbol{K}}$ of the Koopman operator by solving the following least-squares problem:

$$\min_{\widetilde{\boldsymbol{K}} \in \boldsymbol{R}^{N\times N}} \|\boldsymbol{\psi}(\boldsymbol{Y}) - \widetilde{\boldsymbol{K}} \cdot \boldsymbol{\psi}(\boldsymbol{X})\|_F^2 = \min_{\widetilde{\boldsymbol{K}} \in \boldsymbol{R}^{N\times N}} \sum_{k=1}^{M} \|\boldsymbol{\psi}(\boldsymbol{x}_{k+1}) - \widetilde{\boldsymbol{K}} \cdot \boldsymbol{\psi}(\boldsymbol{x}_k)\|_2^2 \tag{5.26}$$

where $\|\cdot\|_F$ refers to the Frobenius norm of a matrix and $\|\cdot\|_2$ is the 2-norm of a vector. $\boldsymbol{\psi}(\boldsymbol{Y}) := [\boldsymbol{\psi}(\boldsymbol{x}_2), \ldots, \boldsymbol{\psi}(\boldsymbol{x}_{M+1})]$, $\boldsymbol{\psi}(\boldsymbol{X}) := [\boldsymbol{\psi}(\boldsymbol{x}_1), \ldots, \boldsymbol{\psi}(\boldsymbol{x}_M)]$, and $\boldsymbol{\psi}(\boldsymbol{x}_k) := [\psi_1(\boldsymbol{x}_k), \ldots, \psi_N(\boldsymbol{x}_k)]^T$ at time instant k.

The closed-form solution can be readily obtained as

$$\widetilde{\boldsymbol{K}} = \boldsymbol{A} \cdot \boldsymbol{U}^{\dagger} \tag{5.27}$$

where † denotes the Moore–Penrose pseudoinverse, $\boldsymbol{A} := \boldsymbol{\psi}(\boldsymbol{Y}) \cdot \boldsymbol{\psi}(\boldsymbol{X})^T$ and $\boldsymbol{U} := \boldsymbol{\psi}(\boldsymbol{X}) \cdot \boldsymbol{\psi}(\boldsymbol{X})^T$. The basis functions are customized and can have various choices. This study will use monomials as the basis functions, for comparison with the SOSP that generally shows

less conservativeness than other model-based methods. Once $\widetilde{\boldsymbol{K}}$ is obtained, the Koopman eigenfunction φ_i corresponding to an eigenpair $(\mu_i, \boldsymbol{v}_i)$ of $\widetilde{\boldsymbol{K}}^T$ is obtained as

$$\varphi_i(\boldsymbol{x}) = \boldsymbol{v}_i^T \cdot \boldsymbol{\psi}(\boldsymbol{x}) \tag{5.28}$$

Generally, the eigenvalues λ_i of the continuous-time system are mapped to the equivalent discrete-time system as $e^{\lambda_i \Delta t}$ [137]. Therefore, the eigenvalue of $\boldsymbol{K}^t$ corresponding to φ_i is $\lambda_i = \frac{log\mu_i}{\Delta t}$.

5.3.2 Stable Koopman Operator

Because $\widetilde{\boldsymbol{K}}$ is used to numerically approximate $\boldsymbol{K}^t$ via the EDMD, there will obviously be errors accumulated over a given time span. The actual value of the basis function at certain time step *k* can be expressed as its approximated value plus an error $\mathcal{E}_k$:

$$\boldsymbol{\psi}(\boldsymbol{x}_k) = \widetilde{\boldsymbol{K}} \cdot \boldsymbol{\psi}(\boldsymbol{x}_{k-1}) + \mathcal{E}_k \tag{5.29}$$

Likewise,

$$\boldsymbol{\psi}(\boldsymbol{x}_{k-1}) = \widetilde{\boldsymbol{K}} \cdot \boldsymbol{\psi}(\boldsymbol{x}_{k-2}) + \mathcal{E}_{k-1} \tag{5.30}$$

Iteratively, a generalized expression at time step *k* is obtained:

$$\boldsymbol{\psi}(\boldsymbol{x}_k) = \widetilde{\boldsymbol{K}}^k \cdot \boldsymbol{\psi}(\boldsymbol{x}_0) + \sum_{i=0}^{k-1} \widetilde{\boldsymbol{K}}^i \cdot \mathcal{E}_{k-i} \tag{5.31}$$

It follows that the accumulated error $\sum_{i=0}^{k-1} \widetilde{\boldsymbol{K}}^i \cdot \mathcal{E}_{k-i}$ can be bounded based on the norm properties:

$$\left\|\sum_{i=0}^{k-1} \widetilde{\boldsymbol{K}}^i \cdot \varepsilon_{k-i}\right\| \leq \sum_{i=0}^{k-1}\left\|\widetilde{\boldsymbol{K}}^i \cdot \varepsilon_{k-i}\right\| \leq \sum_{i=0}^{k-1}\left\|\widetilde{\boldsymbol{K}}^i \cdot \varepsilon_{k-i}\right\| \leq$$
$$\sum_{i=0}^{k-1}\left\|\widetilde{\boldsymbol{K}}^i\right\| \cdot \|\varepsilon_{k-i}\| \leq \sum_{i=0}^{k-1}\left\|\widetilde{\boldsymbol{K}}^i\right\| \cdot \|\varepsilon_{k-i}\| \leq \sum_{i=0}^{k-1}\left\|\widetilde{\boldsymbol{K}}\right\|^i \cdot \|\varepsilon_{k-i}\| \tag{5.32}$$

If $\|\varepsilon_i\| \leq e_{max}$ for any i, then

$$\left\|\sum_{i=0}^{k-1} \widetilde{\boldsymbol{K}}^i \cdot \varepsilon_{k-i}\right\| \leq e_{max} \cdot \sum_{i=0}^{k-1}\left\|\widetilde{\boldsymbol{K}}\right\|^i \tag{5.33}$$

Inequality (5.33) shows that the accumulated error could be enlarged exponentially if the learned Koopman operator $\widetilde{\boldsymbol{K}}$ is unstable. Inspired by [138] and [139], the SOC algorithm is applied to learn a stable Koopman operator in light of its superior numerical stability over longer horizons. Specifically, the matrix $\widetilde{\boldsymbol{K}}$ is stable if and only if it can be expressed as $\widetilde{\boldsymbol{K}} = \boldsymbol{S}^{-1} \cdot \boldsymbol{O} \cdot \boldsymbol{C} \cdot \boldsymbol{S}$, where $\boldsymbol{S}$ is positive definite, $\boldsymbol{O}$ is orthogonal, and $\boldsymbol{C}$ is positive semidefinite contraction (i.e., the singular values of $\boldsymbol{C}$ are less than or equal to 1). Hence, the following optimization problem is solved rather than (5.26) that is in the EDMD:

$$\inf_{\widetilde{\boldsymbol{K}}} \|\boldsymbol{\psi}(\boldsymbol{Y}) - \widetilde{\boldsymbol{K}} \cdot \boldsymbol{\psi}(\boldsymbol{X})\|_F^2 = \inf_{\boldsymbol{S},\boldsymbol{O},\boldsymbol{C}} \|\boldsymbol{\psi}(\boldsymbol{Y}) - \boldsymbol{S}^{-1} \cdot \boldsymbol{O} \cdot \boldsymbol{C} \cdot \boldsymbol{S} \cdot \boldsymbol{\psi}(\boldsymbol{X})\|_F^2 \tag{5.34}$$

This way, the stability constraint is naturally imposed on $\widetilde{\boldsymbol{K}}$. Define $f(\boldsymbol{S},\boldsymbol{O},\boldsymbol{C}) := \|\boldsymbol{\psi}(\boldsymbol{Y}) - \boldsymbol{S}^{-1} \cdot \boldsymbol{O} \cdot \boldsymbol{C} \cdot \boldsymbol{S} \cdot \boldsymbol{\psi}(\boldsymbol{X})\|_F^2$. Then, it can be solved using the gradient descent algorithm. The gradients with respect to the matrices $\boldsymbol{S}$, $\boldsymbol{O}$, and $\boldsymbol{C}$, originally derived in [138], are reproduced as the following compact form:

$$\nabla_{\boldsymbol{S}} f(\boldsymbol{S},\boldsymbol{O},\boldsymbol{C}) = \boldsymbol{S}^{-T}(\boldsymbol{W} \cdot \boldsymbol{E}^T - \boldsymbol{E}^T \cdot \boldsymbol{W}) \tag{5.35}$$
$$\nabla_{\boldsymbol{O}} f(\boldsymbol{S},\boldsymbol{O},\boldsymbol{C}) = -\boldsymbol{S}^{-T} \cdot \boldsymbol{W} \cdot \boldsymbol{S}^T \cdot \boldsymbol{C}^T \tag{5.36}$$
$$\nabla_{\boldsymbol{C}} f(\boldsymbol{S},\boldsymbol{O},\boldsymbol{C}) = -\boldsymbol{O}^T \cdot \boldsymbol{S}^{-T} \cdot \boldsymbol{W} \cdot \boldsymbol{S}^T \tag{5.37}$$

where $\boldsymbol{E} = \boldsymbol{S}^{-1} \cdot \boldsymbol{O} \cdot \boldsymbol{C} \cdot \boldsymbol{S}$ and $\boldsymbol{W} = [\boldsymbol{\psi}(\boldsymbol{Y}) - \boldsymbol{E} \cdot \boldsymbol{\psi}(\boldsymbol{X})] \cdot \boldsymbol{\psi}(\boldsymbol{X})^T$. Afterwards, (5.28) is utilized to derive the Koopman eigenfunctions.

Remark 2: Under the Koopman operator framework, the Koopman eigenfunctions can be leveraged to construct Lyapunov functions in a systematic way with strict stability guarantees [136]. In the following section, the Koopman eigenfunctions will be used to constitute a linear space of Lyapunov candidate functions, and the union of sublevel sets of the decided Lyapunov functions will provide an inner approximation to the actual ROA.

5.4. Proposed Data-Driven ROA Estimation Method

The details of the proposed data-driven ROA estimation are elaborated in Fig. 5.6. First, the ADN operation data will be collected/simulated for the SOC algorithm to approximate the Koopman eigenfunctions as explained in Section 5.3; second, the Lyapunov candidate functions are linearly parameterized using the learned Koopman eigenfunctions; third, polytope constraints are formed; and fourth, a tight inner estimation to the actual ROA is obtained via sampling and linear programming (LP).

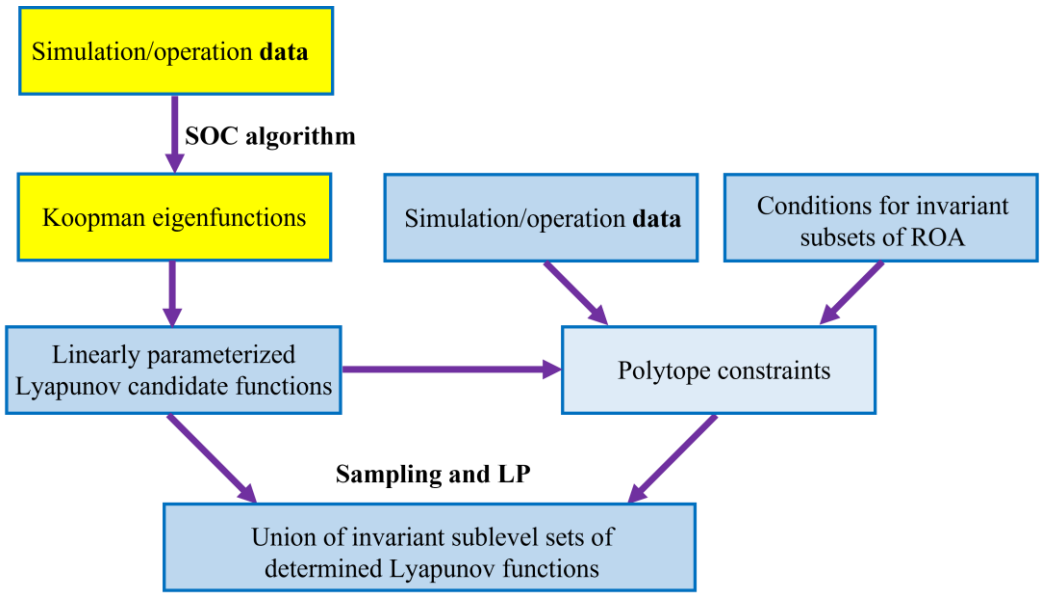

Figure 5.6. Flowchart of proposed data-driven ROA estimation.

When an equilibrium state $\boldsymbol{x}^*$ of the dynamical system (5.22) is nonzero, any system state $\boldsymbol{x}$ can be translated to $\boldsymbol{x}$ -$\boldsymbol{x}^*$. Therefore, $\boldsymbol{x}^*$ is assumed as the origin for simplicity. If the origin is asymptotically stable but not globally attractive, it is desirable to know which trajectories will converge to it as time approaches infinity. The ROA of the system equilibrium state $\boldsymbol{x}^* = \mathbf{0}$ for (5.22) is mathematically defined as a set $ROA_{\boldsymbol{x}^*=\mathbf{0}} := \left\{\boldsymbol{x} \in \boldsymbol{\mathcal{R}}^p : \lim_{t\to\infty} \boldsymbol{F}(\boldsymbol{x}, t) = \mathbf{0}\right\}$. Furthermore, the γ-sublevel set $\boldsymbol{\Omega}_{V,\gamma}$ of a Lyapunov function $V(\boldsymbol{x})$ with a positive γ is defined as $\boldsymbol{\Omega}_{V,\gamma} = \{\boldsymbol{x} \in \boldsymbol{\mathcal{R}}^p : V(\boldsymbol{x}) \leq \gamma\}$, which can practically characterize the forward invariant subsets of the actual ROA [76]. If the following conditions are satisfied:

1) $\boldsymbol{\Omega}_{V,\gamma}$ is bounded;
2) $V(\mathbf{0}) = 0$ and $V(\boldsymbol{x}) > 0$ for all $\boldsymbol{x} \in \boldsymbol{\mathcal{R}}^p$;

$$3)\quad \boldsymbol{\Omega}_{V,\gamma} \setminus \{\mathbf{0}\} \subset \left\{\boldsymbol{x} \in \mathcal{R}^p : \dot{V}(\boldsymbol{x}) = \frac{\partial V(\boldsymbol{x})}{\partial \boldsymbol{x}} \cdot \boldsymbol{f}(\boldsymbol{x}) < 0\right\} \tag{5.38}$$

then the flow $\boldsymbol{F}(\boldsymbol{x}, t)$ of (5.22) exists and $\boldsymbol{F}(\boldsymbol{x}, t) \in \boldsymbol{\Omega}_{V,\gamma}$ holds for all $\boldsymbol{x} \in \boldsymbol{\Omega}_{V,\gamma}$ and $t \geq 0$. In addition, $\lim_{t\to\infty} \boldsymbol{F}(\boldsymbol{x}, t) = \mathbf{0}$. Accordingly, $\boldsymbol{\Omega}_{V,\gamma}$ is an invariant subset of $ROA_{\boldsymbol{x}^*=\mathbf{0}}$.

Under the assumption that large amounts of system historical operation data or high-fidelity simulation data are available, our goal is to estimate the ROA of the DC ADN (5.21) in a data-driven fashion. Fig. 5.7 illustrates how to apply the conditions in (5.38) to various trajectory data to find a Lyapunov function and its γ-sublevel set.

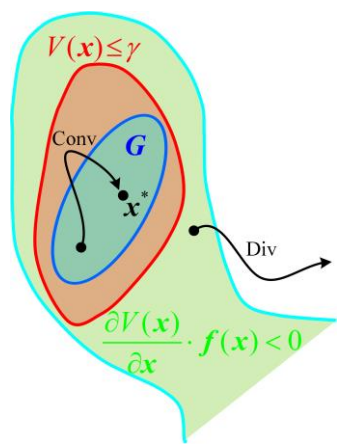

Figure 5.7. Illustration diagram of ROA inner estimation.

Suppose there exists a Lyapunov function $V(\boldsymbol{x})$ to certify that a set $\boldsymbol{G}$ lies inside the ROA. As is observed from Fig. 5.7, $V(\boldsymbol{x}) \leq \gamma$ and $\dot{V}(\boldsymbol{x}) < 0$ should hold for a convergent trajectory starting from $\boldsymbol{G}$, while $V(\boldsymbol{x}) > \gamma$ is satisfied for a divergent trajectory starting from $\boldsymbol{G}$'s complement $\boldsymbol{G}^c$. Also, $\boldsymbol{G}$ will not be within the ROA if at least one trajectory

eventually diverges with initial conditions in $\boldsymbol{G}$. Thus, a smaller region of $\boldsymbol{G}$ should be chosen.

Conventionally, it is computationally intensive or even intractable for those optimization-based methods such as the SOSP to calculate the maximum ROA, when dealing with many decision variables due to the high dimension of an ADN, not to mention the lifted space $\boldsymbol{\mathcal{F}}_N$. To address this issue, it is proposed to reduce the number of decision variables for ROA estimation via linearly parameterizing an arbitrary Lyapunov candidate function using the Koopman eigenfunctions from Section 5.3. Specifically, a set of Koopman eigenfunctions φ_i $(i = 1, 2, \dots, N_\phi)$ with a sufficiently large negative real part $\mathrm{Re}[\lambda_i]$ are selected to construct the basis $\boldsymbol{\phi}_i(\boldsymbol{x})$ of the linear space for Lyapunov candidate functions, as such eigenfunctions can capture the stability properties of the underlying dynamical system [94]. Further, if the basis is chosen as $\boldsymbol{\phi}_i(\boldsymbol{x}) \coloneqq \varphi_i(\boldsymbol{x}) \cdot \bar{\varphi}_i(\boldsymbol{x}) = |\varphi_i(\boldsymbol{x})|^2$ (the overbar denotes complex conjugation), then $\boldsymbol{\phi}_i(\boldsymbol{x}) \geq 0$ and $\dot{\boldsymbol{\phi}}_i(\boldsymbol{x}) = 2 \cdot \mathrm{Re}[\lambda_i] \cdot |\varphi_i(\boldsymbol{x})|^2 = 2 \cdot \mathrm{Re}[\lambda_i] \cdot \boldsymbol{\phi}_i(\boldsymbol{x}) \leq 0$ hold for $i = 1, 2, \dots, N_\phi$. It follows from the following proof that the family of sets $\boldsymbol{\mathcal{V}}_\gamma = \left\{\boldsymbol{x} \in \boldsymbol{\mathcal{R}}^p : \sum_{i=1}^{N_\phi} \alpha_i \cdot \boldsymbol{\phi}_i(\boldsymbol{x}) \leq \gamma\right\}$ with $\alpha_i > 0$ are forward invariant.

Prove that the family of sets $\boldsymbol{\mathcal{V}}_\gamma = \left\{\boldsymbol{x} \in \boldsymbol{\mathcal{R}}^p : \sum_{i=1}^{N_\phi} \alpha_i \cdot \boldsymbol{\phi}_i(\boldsymbol{x}) \leq \gamma\right\}$ with $\alpha_i > 0$ are forward invariant.

<u>Proof:</u>

According to the spectral property of the Koopman operator in [136], an eigenfunction $\varphi(\boldsymbol{x})$ and its corresponding eigenvalue $\lambda \in \boldsymbol{\mathcal{C}}$ of the Koopman operator $\boldsymbol{K}^t$ satisfies

$$\boldsymbol{K}^t \varphi(\boldsymbol{x}) = e^{\lambda t} \cdot \varphi(\boldsymbol{x})$$

$$\frac{d\varphi(\boldsymbol{x})}{dt} = \lambda \cdot \varphi(\boldsymbol{x})$$

For each $\phi_i(\boldsymbol{x}) \coloneqq \varphi_i(\boldsymbol{x}) \cdot \bar{\varphi}_i(\boldsymbol{x}) = |\varphi_i(\boldsymbol{x})|^2$ $(i = 1, 2, \dots, N_\phi)$,

$$\dot{\phi}_i(\boldsymbol{x}) = \frac{d\phi_i(\boldsymbol{x})}{dt} = \frac{d\varphi_i(\boldsymbol{x})}{dt} \cdot \bar{\varphi}_i(\boldsymbol{x}) + \varphi_i(\boldsymbol{x}) \cdot \frac{d\bar{\varphi}_i(\boldsymbol{x})}{dt}$$

Note $\frac{d\bar{\varphi}_i(\boldsymbol{x})}{dt} = \overline{\frac{d\varphi_i(\boldsymbol{x})}{dt}} = \overline{\lambda_i \cdot \varphi_i(\boldsymbol{x})} = \bar{\lambda}_i \cdot \overline{\varphi_i(\boldsymbol{x})}$, thus

$$\dot{\phi}_i(\boldsymbol{x}) = \left(\lambda_i + \bar{\lambda}_i\right) \cdot |\varphi_i(\boldsymbol{x})|^2 = 2 \cdot \mathrm{Re}[\lambda_i] \cdot \phi_i(\boldsymbol{x})$$

Since the Koopman eigenfunctions are approximated using the SoC algorithm, there are approximation errors $\mathrm{e}_i(\boldsymbol{x})$'s. With a mild assumption that the errors are bounded such that $|\mathrm{e}_i(\boldsymbol{x})| \leq \zeta_i \cdot \phi_i^2(\boldsymbol{x}) + \eta_i$ for some positive constants ζ_i and η_i,

$$\dot{\phi}_i(\boldsymbol{x}) = 2 \cdot \mathrm{Re}[\lambda_i] \cdot \phi_i(\boldsymbol{x}) + \mathrm{e}_i(\boldsymbol{x}) \leq 2 \cdot \mathrm{Re}[\lambda_i] \cdot \phi_i(\boldsymbol{x}) + |\mathrm{e}_i(\boldsymbol{x})|$$

$$= \zeta_i \cdot \phi_i^2(\boldsymbol{x}) + 2 \cdot \mathrm{Re}[\lambda_i] \cdot \phi_i(\boldsymbol{x}) + \eta_i$$

If $\dot{\phi}_i(\boldsymbol{x}) \leq 0$ always holds for certain interval $(\underline{\gamma_i}, \overline{\gamma_i}) \subset \boldsymbol{\mathcal{R}}_{>0}$, the minimum of the above quadratic function of $\phi_i(\boldsymbol{x})$ should be negative, which leads to the condition $(\mathrm{Re}[\lambda_i])^2 > \zeta_i \cdot \eta_i$. It also implies that the $\overline{\gamma_i}$-sublevel set of $\phi_i(\boldsymbol{x})$ is forward invariant.

Further, define $\gamma \coloneqq \min_i(\alpha_i \cdot \overline{\gamma_i})$ for $\alpha_i > 0$ ($i = 1, 2, \dots, N_\phi$). From $\sum_{i=1}^{N_\phi} \alpha_i \cdot \phi_i(\boldsymbol{x}) \leq \gamma$,

$$\alpha_i \cdot \phi_i(\boldsymbol{x}) \leq \gamma = \min_i(\alpha_i \cdot \overline{\gamma_i})$$

Thus, $\phi_i(\boldsymbol{x}) \leq \overline{\gamma_i}$ holds for $i = 1, 2, \dots, N_\phi$.

Now, define $\beta \coloneqq 2 \cdot \min_i |\mathrm{Re}[\lambda_i]|$. Then,

$$\sum_{i=1}^{N_\phi} \alpha_i \cdot \dot{\phi}_i(\boldsymbol{x}) \leq \sum_{i=1}^{N_\phi} \alpha_i \cdot (2 \cdot \mathrm{Re}[\lambda_i]) \cdot \phi_i(\boldsymbol{x}) + \sum_{i=1}^{N_\phi} \alpha_i \cdot [\zeta_i \cdot \phi_i^2(\boldsymbol{x}) + \eta_i]$$

$$\leq \sum_{i=1}^{N_\phi} \alpha_i \cdot (-\beta) \cdot \phi_i(\boldsymbol{x}) + \sum_{i=1}^{N_\phi} \alpha_i \cdot (\zeta_i \cdot \overline{\gamma_i}^2 + \eta_i)$$

Therefore, if $\gamma \cdot \beta \geq \sum_{i=1}^{N_\phi} \alpha_i \cdot (\zeta_i \cdot \overline{\gamma_i}^2 + \eta_i)$,

$$\sum_{i=1}^{N_\phi} \alpha_i \cdot \dot{\phi}_i(\boldsymbol{x}) \leq \sum_{i=1}^{N_\phi} \alpha_i \cdot (-\beta) \cdot \phi_i(\boldsymbol{x}) + \gamma \cdot \beta = \beta \cdot [\gamma - \sum_{i=1}^{N_\phi} \alpha_i \cdot \phi_i(\boldsymbol{x})]$$

This suggests that the γ-sublevel set of $\sum_{i=1}^{N_\phi} \alpha_i \cdot \phi_i(\boldsymbol{x})$ is forward invariant. It should also be noted that the condition $\gamma \cdot \beta \geq \sum_{i=1}^{N_\phi} \alpha_i \cdot (\zeta_i \cdot \overline{\gamma_i}^2 + \eta_i)$ can be easily met if β is large enough, which translates to that all λ_i's ($i = 1, 2, \dots, N_\phi$) have a sufficiently large negative real part.

Q.E.D.

Consider a Lyapunov candidate function as $V(\boldsymbol{x}) = \sum_{i=1}^{N_\phi} \alpha_i \cdot \phi_i(\boldsymbol{x})$, where the coefficients α_i are to be determined. When the conditions discussed in (5.38) and observed

in Fig. 5.7 are strictly imposed on the trajectory data, they could be naturally translated into constraints on α_i in an LP problem. It should also be noted that the above constructed Lyapunov candidate function will lead to stronger expressive power and thus a less conservative ROA approximation when higher-degree monomials are adopted for $\psi_i(\boldsymbol{x})$, compared to the conventional quadratic Lyapunov functions used in the T-S multi-modeling.

To seek a Lyapunov function whose γ-sublevel set is forward invariant, numerous trajectory data need to be sampled initially from a prechosen set $\boldsymbol{G}$. In practice, $\boldsymbol{G}$ for an ADN is related to the allowable operating ranges of each dynamic state variable. For instance, the typical frequency of islanded microgrids lies between 59.3 and 60.5 Hz, while the DC common bus voltage is $\pm 5\%$ of the rated value. However, $\boldsymbol{G}$ should be shrunk accordingly once divergent trajectories beginning from $\boldsymbol{G}$ are detected. Based on the condition $\boldsymbol{\mathcal{V}}_\gamma \setminus \{\boldsymbol{0}\} \subset \{\boldsymbol{x} \in \boldsymbol{\mathcal{R}}^p : \dot{V}(\boldsymbol{x}) < 0\}$, there should be $\dot{V}(\boldsymbol{x}) \leq \beta \cdot [\gamma - V(\boldsymbol{x})]$ for the convergent trajectory data with initial conditions in $\boldsymbol{G}$, where β is a positive constant and can be initially set as twice the minimum of $|\mathrm{Re}[\lambda_i]|$. Thus, on a convergent trajectory $[\boldsymbol{x}_0, \boldsymbol{x}_1, \dots, \boldsymbol{x}_T]$ with $(T+1)$ time steps, any data point $\boldsymbol{x}_k$ should satisfy 1) $\sum_{i=1}^{N_\phi} \alpha_i \cdot \phi_i(\boldsymbol{x}_k) \leq \gamma$; 2) $\sum_{i=1}^{N_\phi} \alpha_i \cdot \dot{\phi}_i(\boldsymbol{x}_k) + \beta \cdot \left[\sum_{i=1}^{N_\phi} \alpha_i \cdot \phi_i(\boldsymbol{x}_k) - \gamma\right] \leq 0$. In compact matrix form, the constraints are

$$\boldsymbol{\Phi} \cdot \boldsymbol{\alpha} \leq \boldsymbol{0} \tag{5.39.1}$$

$$(\boldsymbol{\Phi}_{dot} + \beta \cdot \boldsymbol{\Phi}) \cdot \boldsymbol{\alpha} \leq \boldsymbol{0} \tag{5.39.2}$$

$$\boldsymbol{\alpha} \geq \boldsymbol{\delta} \tag{5.39.3}$$

$$\boldsymbol{\alpha}[1{:}N_\phi] \leq \boldsymbol{1} \tag{5.39.4}$$

$$[1 \quad 1 \ldots \quad 1 \quad 0] \cdot \boldsymbol{\alpha} \geq 1 \tag{5.39.5}$$

where $\boldsymbol{\Phi} := \begin{bmatrix} \phi_1(\boldsymbol{x}_0) & \phi_2(\boldsymbol{x}_0) & \cdots & \phi_{N_\phi}(\boldsymbol{x}_0) & -1 \\ \vdots & & \ddots & \vdots & \\ \phi_1(\boldsymbol{x}_T) & \phi_2(\boldsymbol{x}_T) & \cdots & \phi_{N_\phi}(\boldsymbol{x}_T) & -1 \end{bmatrix}$, $\boldsymbol{\Phi}_{dot} := \begin{bmatrix} \dot{\phi}_1(\boldsymbol{x}_0) & \dot{\phi}_2(\boldsymbol{x}_0) & \cdots & \dot{\phi}_{N_\phi}(\boldsymbol{x}_0) & 0 \\ \vdots & & \ddots & \vdots & \\ \dot{\phi}_1(\boldsymbol{x}_T) & \dot{\phi}_2(\boldsymbol{x}_T) & \cdots & \dot{\phi}_{N_\phi}(\boldsymbol{x}_T) & 0 \end{bmatrix}$, and $\boldsymbol{\alpha} := \begin{bmatrix} \alpha_1 & \alpha_2 \ldots & \alpha_{N_\phi} & \gamma \end{bmatrix}^T$. $\boldsymbol{\delta}$ is a vector with all fixed small positive constants δ for tightness.

However, a divergent trajectory starting from the complement of $\boldsymbol{G}$ should obey

$$\boldsymbol{\Phi} \cdot \boldsymbol{\alpha} \geq \boldsymbol{\delta} \tag{5.39.6}$$

Each row of the above constraints defines a half-space in $\boldsymbol{\mathcal{R}}^{N_\phi+1}$ and the intersection of these half-spaces defines a feasible polytope [140]. As more trajectories are considered, the feasible polytope will be iteratively refined with a monotonic decrease in volumes. Theoretically, it will converge to a certain convex polytope $\boldsymbol{\mathcal{P}}$ as the number of iterations approaches infinity. The detailed ROA estimation algorithm is presented as follows:

Table 5.1

Proposed ROA Estimation Algorithm

Stage 1: Construct a feasible polytope $\boldsymbol{\mathcal{P}}$ using data
Initialize: $\boldsymbol{G}$, $\boldsymbol{A}_c$, $\boldsymbol{A}_d$, ρ, β, and δ

Stage 1: Construct a feasible polytope $\boldsymbol{\mathcal{P}}$ using data	
Generate K_{max} simulation trajectories:	
1	$k = 0$, $K_c = 0$, and $K_d = 0$
2	while $k < K_{max}$:
3	sample a random initial state $\boldsymbol{x}_{0k}$ from $\boldsymbol{G}$
4	if a trajectory from $\boldsymbol{x}_{0k}$ converges:
5	save this trajectory in $\boldsymbol{A}_c$, and $K_c += 1$
6	else:
7	save this trajectory in $\boldsymbol{A}_d$, and $K_d += 1$
8	$k += 1$
Apply constraints (5.39.1~ 5.39.6) to simulated trajectories:	
9	$\boldsymbol{\mathcal{P}} = \{\boldsymbol{\alpha} \in \boldsymbol{\mathcal{R}}^{N_\phi+1}: (5.39.3) - (5.39.5)\}$
10	for $i = 1{:}K_c$:
11	form polytope $\boldsymbol{\mathcal{P}}_i$ based on (5.39.1), (5.39.2) using $\boldsymbol{A}_c(i)$
12	$\boldsymbol{\mathcal{P}}_i \longleftarrow \boldsymbol{\mathcal{P}} \cap \boldsymbol{\mathcal{P}}_i$
13	if *is_empty*($\boldsymbol{\mathcal{P}}_i$):
14	$\beta \longleftarrow \rho \cdot \beta$
15	go to Line 10
16	$\boldsymbol{\mathcal{P}} \longleftarrow \boldsymbol{\mathcal{P}}_i$
17	for $i = 1{:}K_d$:
18	use $\boldsymbol{x}_{0i}$ of $\boldsymbol{A}_d(i)$ as a new vertex and project as $\boldsymbol{G}_i$
19	$\boldsymbol{G} \longleftarrow \boldsymbol{G}_i$
20	form polytope $\boldsymbol{\mathcal{P}}_i$ based on (5.39.6) using $\boldsymbol{A}_d(i)$
21	$\boldsymbol{\mathcal{P}} \longleftarrow \boldsymbol{\mathcal{P}} \cap \boldsymbol{\mathcal{P}}_i$
Stage 2: Determine $\boldsymbol{\mathcal{V}}_\gamma$ via sampling and linear optimization	
Initialize: $\boldsymbol{\mathcal{V}}_\gamma = \emptyset$	
22	$j = 0$

Stage 2: Determine $\boldsymbol{\mathcal{V}}_\gamma$ via sampling and linear optimization	
23	while $j < N_{max}$:
24	sample $\boldsymbol{x}_j$ from $\boldsymbol{G}$
25	solve: $\max_{\boldsymbol{\alpha}} \sum_{i=1}^{N_\phi} \alpha_i \cdot \phi_i(\boldsymbol{x}_j) - \gamma$
26	$s.t.\ \boldsymbol{\alpha} \subseteq \boldsymbol{\mathcal{P}}$
27	$\boldsymbol{\mathcal{V}}_{\gamma,j} = \left\{\boldsymbol{x} \in \boldsymbol{\mathcal{R}}^p : \sum_{i=1}^{N_\phi} \alpha_i \cdot \phi_i(\boldsymbol{x}) \leq \max\{\gamma + obj_{max}, \gamma\}\right\}$
28	$\boldsymbol{\mathcal{V}}_\gamma \longleftarrow \boldsymbol{\mathcal{V}}_\gamma \cup \boldsymbol{\mathcal{V}}_{\gamma,j}$
29	$j = j + 1$

The proposed ROA estimation algorithm consists of two stages, given the already learned Koopman eigenfunctions from Section 5.3. In Stage 1, numerical simulations are conducted to generate trajectory data when historical operation data of the ADN are not readily available. If runtime is of concern, a time limit can be set rather than K_{max}. Then the actual number of collected trajectory data will be simulated in this stage. During this process, the K_c convergent and K_d divergent trajectories are stored in arrays $\boldsymbol{A}_c$ and $\boldsymbol{A}_d$, respectively. In Line 14, the preset β is amplified by a constant parameter ρ once the intersection of intermediate polytopes becomes empty. As is shown in Line 18, the disqualified initial state is used as a new vertex, whose projections on the coordinate axis of each state attain $\boldsymbol{G}_i$. A tight polytope $\boldsymbol{\mathcal{P}}$ is finally obtained in Line 21. In Stage 2, a set of $\boldsymbol{x}$'s are sampled from the refined $\boldsymbol{G}$ and LP problems are solved on each $\boldsymbol{x}$ to derive the invariant sub-level sets $\boldsymbol{\mathcal{V}}_\gamma$ (in Line 27) of each Lyapunov candidate function; obj_{max} represents the maximum of the objective function in Line 25. Theoretically, for a sufficiently large number of samples N_{max}, $\boldsymbol{\mathcal{V}}_\gamma$ will converge and cover the largest sub-

level set of a single Lyapunov function that is based on the SOSP [85]. Furthermore, the proposed ROA estimation can be even closer to the actual one if obj_{max} is positive. It is also noteworthy that different sampling techniques can lead to different convergence rates. The efficient high-dimensional sampling method named the Dikin Walk [141] can be adopted to generate uniform random samples for Lines 3 and 24. Lastly, both stages in the proposed algorithm are highly parallelizable and parallel computing can be leveraged for speedup in simulation and optimization.

5.5. Case Studies

To verify the effectiveness of the proposed data-driven approach for ROA estimation, numerical simulations of the DC ADN shown in Fig. 5.1 are conducted in MATLAB/Simulink with a fixed step size of 50 μs. Averaged modeling [142] for the PWM power converters is implemented. In addition, Python interacts with Simulink for data collection and computations. The experiment platform is a high-performance server with an AMD EPYC 7B13 CPU (64 cores) and 512-GB RAM.

The EV battery models in the simulations have low initial state of charge (SoC) values and are only charged in the CP mode for simplicity. Also, an EV's arrival and departure times are assumed to follow the truncated normal distributions suggested by [143]. In Fig. 5.1, each simulated charging load represents one charger with variable numbers of charging ports. For instance, the Ultra-Fast Charging Load (2) represents three charging ports, with possible charging power levels of 0 kW (idle), 400 kW (for 1 EV), 800 kW (for 2 EVs), or 1200 kW (for 3 EVs). The duration of each level of charging power can be determined by the overlapping of EVs' arrival and departure times. In the preset $\boldsymbol{G}$,

ω is $0.995\omega_s \sim 1.005\omega_s$, T_m is from 0 to 1.1 times the rated value, the DC-link voltages are $0.95V_n \sim 1.05V_n$, the unidirectional inductor currents are from 0 to 1.2 times the rated values, and the range of bidirectional inductor currents is ±1.2 times the rated values. Besides, an EV battery terminal voltage corresponds to the SoC range of 10%~60%. Firstly, simulated system operation data are used to learn the Koopman eigenfunctions via the SOC algorithm executed in Python. 100 different trajectories are collected with random initial states within $\boldsymbol{G}$. Each trajectory lasts for 20 sec and is sampled with $\Delta t = 0.01$ sec. The probability distribution parameters used during each trajectory collection are presented in Table 5.2. During operations, the SOC algorithm is executed offline regularly using the most recent state measurements to maintain high precision of the learned Koopman eigenfunctions. Communication latency is ignored during the simulations because the ADNs under consideration usually do not span a large geographic area.

Table 5.2

Statistical Distribution of EV Charging Behavior

	Distribution	Boundaries
Arrival time (sec)	$\mathcal{N}(3, 1^2)$	$[0, 6]$
Departure time (sec)	$\mathcal{N}(15, 1^2)$	$[13, 18]$

There is always a trade-off between computational cost and expressivity in designing the Lyapunov candidate function when selecting the monomial basis for the SOC algorithm. This study chooses the monomials in $\boldsymbol{x}$ of degree up to 4. As the number of

states of the simulated DC ADN is 21, there are 12649 (N) monomial functions in the basis when the special monomial "1" is removed. It takes on average 791.18 sec for the SOC algorithm to obtain the Koopman eigenfunctions based on the concatenated trajectory data. 5368 (N_ϕ) out of 12649 Koopman eigenfunctions are retained after taking $|\mathrm{Re}[\lambda_i]| > \frac{1}{3} \cdot \max|\mathrm{Re}[\lambda_i]|$ to ensure large enough negative real parts, as mentioned in the above proof. β is determined as 0.0561, ρ is set as 1.07, and δ is $2 \cdot 10^{-16}$.

An extreme scenario is considered, where all EV chargers are in use. At some point, the only two idled EV charging ports at the Ultra-Fast Charging Load (1) request connection to the DC ADN, equivalent to increasing the power level from 800 kW to 1600 kW. To ensure transient stability, the DSO wishes to manage this request by estimating the ROA. Suppose the equilibrium points before and after enabling these charging ports are $\boldsymbol{x}_0$ =[889.8V, 556.2A, 1959.1V, 252.0A 667.5A, **1965.5**V, 344.6A, **411.5**A, **1947.3**V, 925.2A, 864.7V, 617.4A, 1948.1V, 1373.7A, 873.6V, 884.6A, -0.31A, 2000.0V, 432.3A, **377.0**rad/sec, 2620.2N·m]^T and $\boldsymbol{x}_{eq}$ = [891.5V, 555.6A, 1932.6V, 255.8A, 1038.7, **1946.4**V, 536.3A, **837.7**A, **1915.9**V, 1834.2A, 872.3V, 626.1A, 1921.4V, 1371.0A, 875.2V, 1378.0A, -2.25A, 1998.8V, 671.8A, **376.8**rad/sec, 3904.3N·m]^T, respectively. In practice, however, an absolutely stable equilibrium may never exist due to the uncertainties and external disturbances. To this end, the prediction model of Koopman-based MPC discussed in [93] along with the sliding-window scheme in [144] could be integrated to predict the quasi-equilibrium after assuming an EV charger is connected to the DC ADN. Development of such a predictive approach is left for future work.

MATLAB Parallel Computing Toolbox and Parallel Server are utilized for faster simulations in Stage 1 of ROA estimation. For the ADN Simulink model, a run time of 10 sec is sufficient to determine the convergence of each simulated trajectory. 20 10-sec simulation runs are then conducted, and 127 sec are taken to collect the trajectory data. No divergent trajectories commencing from the preset $\boldsymbol{G}$ are found. Nonetheless, the initial β is updated twice to generate a non-empty polytope. In Stage 2, the scipy.optimize and multiprocessing packages of Python are utilized to solve the LP problems in parallel. In addition, the fast and efficient HiGHS solver is chosen. Ideally, if more samples are collected to solve the LP problems, the union of the obtained invariant sets will be closer to the actual ROA. Given the tradeoff between solution time and accuracy, 500 tasks are distributed across all the logical cores. It consumes 1274.87 sec to obtain 500 invariant sets.

For different research focuses, the state variables of interest can be selected from the 21 states. In this study, the transient frequency and voltage stabilities are of interest. The estimated ROAs are respectively presented in a 2-dimensional plane with the other state variables set equal to zero, i.e., $v_{evdc,1}$ versus $i_{line,ev,1}$ and ω versus v_{bdc}. The proposed data-driven method is also compared with the SOSP approach in [86] due to similarities in the tested systems. To apply the SOSP, some simplifications are made to the system model (20). Firstly, the solar PV and the BESS are represented by a generic second-order model [145]. Secondly, the EV charging load is modeled as a CPL which can be further reduced as a controlled current source without internal dynamics [86]. Moreover, Taylor series expansion is utilized to recast the reduced-order model into a polynomial system because it contains rational equations. The scaled-diagonally-dominant sums-of-

squares programming (SDSOSP) [146] is also leveraged in lieu of the conventional SOSP for reduced solution time and improved scalability. The degree of the polynomial Lyapunov candidate function is selected as 4, while the degree of the truncated Taylor expansion is chosen as 3. In addition, the SPOT Toolbox and the MOSEK solver are used to solve the SDSOSP in MATLAB. However, this method still takes as much as 5260.44 sec to obtain an estimate and thus the real-time applications become impracticable. The results of our method and SDSOSP are compared in Fig. 5.8 and Fig. 5.9, wherein the red star represents the projection of $\boldsymbol{x}_0$ and the blue square stands for the $\boldsymbol{x}_{eq}$. The blue dashed line delineates the boundary of the ROA estimated by the SDSOSP, while each green solid line encloses an invariant sublevel set of our linearly parameterized Lyapunov functions.

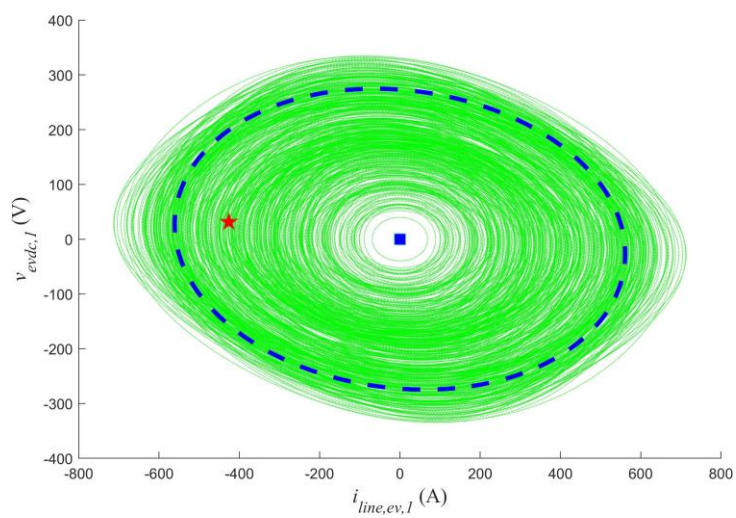

Figure 5.8. Comparison of estimated ROAs ($v_{evdc,1}$ vs. $i_{line,ev,1}$).

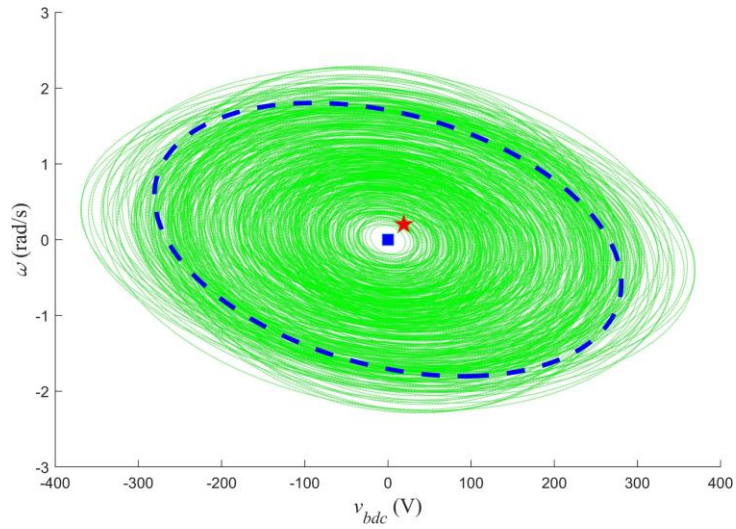

Figure 5.9. Comparison of estimated ROAs (ω vs. v_{bdc}).

Both figures show that $\boldsymbol{x}_0$ lies in the estimated ROAs of $\boldsymbol{x}_{eq}$, indicating a large transient stability margin for the ADN. However, the proposed data-driven approach achieves a better ROA estimation than the SDSOSP. The reason is twofold. First, the linearly parameterized Lyapunov candidate functions have a degree of 8, while the polynomial Lyapunov candidate function only has a degree of 4. Second, a forward invariant subset of the actual ROA is enlarged when the maximum of the corresponding LP objective function is positive. Besides, it can be observed that some of the obtained forward invariant subsets are quite small and may also coincide. Nonetheless, through an increasing number of samplings, the proposed method significantly lessens the conservativeness of the ROA estimation.

A numerical simulation is conducted to further validate the obtained estimation. The power level at the Ultra-Fast Charging Load (1) is increased to 1600 kW to mimic the connection of another two EV charging ports at t = 11.6 sec. Fig. 5.10 and Fig. 5.11 present

the transient responses of the state variables of interest. After the EV charging load is increased, the DC-link voltages stabilize to new equilibria very soon, as shown in Fig. 5.10. In contrast, Fig. 5.11 shows that the angular frequency of the AC grid settles down after a longer transient period. This results from the difference in time scale between electromechanical and electromagnetic dynamics.

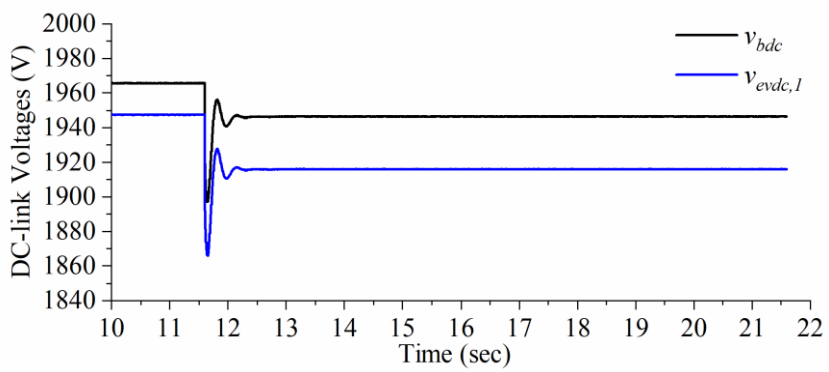

Figure 5.10. Transient response of DC-link voltages after EV load increases.

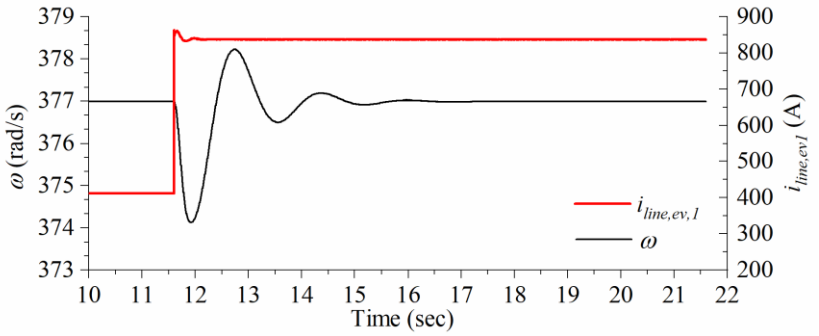

Figure 5.11. Transient response of angular frequency and charging current after EV load increases.

5.6 Conclusion

This chapter has proposed a Koopman-operator-based data-driven approach to estimate the ROA of a future DC ADN dominated by EV supercharging stations. Simulation results demonstrated that a less conservative ROA estimation can be obtained in a computationally efficient manner, compared with the SOSP-based method (SDSOSP). As a result, the proposed ROA estimation has the potential for real-time applications in the assessment of future ADN transient stability. In addition, the method is generic and could be readily applied to other dynamical systems if the system operation data is readily available.

Chapter 6

Conclusions and Future Work

6.1 Conclusions

The overall goal of this Ph.D. dissertation is to study optimal operation and control strategies of emerging electric distribution networks, which are subjected to several challenges, namely, low inertia, economic loss, uncertainty, cyber-physical threats, and transient instability, introduced by increasing integration of distributed renewable energy sources. Chapter 1 reviewed the state of the art in the operation and control of emerging electric distribution networks and identified the major research gaps as well as motivations and objectives. Chapter 2 focused on investigating the control of solar PVs, one of the dominating energy sources in the emerging distribution networks. In particular, control strategies of a campus microgrid that consists of CHP and PV systems has been designed for its islanded operation. A coordinated control was presented for stable operation of the campus microgrid. To further study the scenario of high PV penetration microgrids, the integration of a 10-MW PV farm into the campus microgrid was investigated, and a double-stage PV-VSG control strategy has been proposed and implemented for enhanced inertia support. This approach emulated inertia using the DC-link capacitor and achieved satisfactory transient performance under different operating conditions. In order to further explore the economic and secure operation of emerging distribution networks, Chapter 3 proposed a predictive hierarchical power management framework, which realized its economic operation via tertiary control in the time scale of tens of seconds by solving an AC-OPF problem computationally efficiently. For economic operation, an AC-OPF

problem was solved on the tertiary level. For the regulation of active power and frequency in microgrid systems, a centralized linear MPC secondary controller was designed. Furthermore, a unified linear input-state estimator in an unbiased minimum variance sense was proposed to accurately estimate both the system states and the control signals that are sent by the secondary controller and received by the primary controller in order to enhance the MPC performance by account for potential system anomalies. Compared with the conventional decentralized PI approaches, the proposed framework not only offered superior frequency regulation but also lowered the total operating costs. Considering the potential limitations of centralized control such as single point failure, limited scalability, and high costs of communications, together with increased integration of different DER assets in emerging distribution systems, in Chapter 4, a fully decentralized coordinated control technique was developed for a PV-BESS hybrid system, which only requires measurements of local DC bus voltages. The PV unit can smoothly switch between the MPPT mode and the droop mode to supply power and regulate the DC bus voltages. Furthermore, a SoC-based adaptive droop control was proposed for the BESSs to achieve overcharging and over-discharging protection. Recently, as a result of the availability of large amounts of data in power systems via advanced sensors, data analytics and artificial intelligence have become more appealing alternatives to traditional power system operation and control solutions. In Chapter 5, a data-driven approach based on the Koopman operator theory has been developed for transient stability evaluation of emerging distribution networks with high penetration of EV supercharging stations, i.e., systems with high volatility and reduced stability margin that require more accurate and real-time stability evaluation. When compared with the conventional SOSP-based approaches, the

proposed method provided a less conservative ROA estimation to a future DC ADN dominated by EV supercharging stations in considerably shorter time, thus allowing for real-time applications.

6.2 Future Work

In this Ph.D. dissertation, a few important research challenges of future electric distribution system operation have been addressed, but there are still several open questions that merit further research in the future:

1) The proposed PV-VSG utilizes the DC-link capacitor for inertia emulation. However, the capacitors may not always be able to store sufficient energy to support system inertia and frequent charging and discharging would shorten their lifespan. A synchronous generator powered by concentrated solar power can be integrated with the solar PV to provide robust inertia support, reactive power, and even short circuit contribution in islanded operation. On the other hand, the PV-VSG stability margin could be reduced when it is connected to a strong grid with a low grid impedance. Hence, adaptive virtual inertia control based on the identified grid impedance is highly desired to guarantee adequate stability margins under varying grid strengths.

2) The MPC secondary controller in the proposed hierarchical power management framework is based on a linearized system model, which only works well in the vicinity of a system operating point. It may not function effectively when large disturbances, e.g., a fault, occur. Furthermore, the BESSs are not considered in the testing system considering the renewable penetration level is relatively low compared with the total loads in most existing electric distribution networks. Furthermore, the system uncertainties introduced

by flexible loads and RESs also need to be considered, and a distributed stochastic nonlinear approach can be explored to further improve operational economics, efficiency, and accuracy.

3) Since the decentralized coordinated control proposed in Chapter 4 is for primary control, DC voltage deviations will inevitably occur and accumulate. Secondary control needs to be considered to eliminate those voltage deviations. Specifically, a distributed event-triggered control can be implemented as the secondary control, which only utilizes local information and current measurements from neighbors to help regulate average DC voltage. Additionally, the use of aperiodic communications in this method can reduce communication traffic.

4) The data-driven transient stability evaluation approach in Chapter 5 can be further enhanced in several aspects. Virtual aggregators can be used to add more EV chargers, and modular DNNs can help improve scalability. To anticipate the system's new equilibria only based on data, a predictive technique should be developed. Furthermore, dynamic EV charging can be optimized while adaptively increasing the estimated ROAs by using control-Lyapunov functions.

References

[1] EPA. "Inventory of U.S. Greenhouse Gas Emissions and Sinks." https://www.epa.gov/ghgemissions/inventory-us-greenhouse-gas-emissions-and-sinks (accessed 5 Nov., 2022).

[2] R. H. Lasseter, "Microgrids," in *2002 IEEE Power Engineering Society Winter Meeting. Conference Proceedings (Cat. No. 02CH37309)*, 2002, vol. 1: IEEE, pp. 305-308.

[3] R. Lasseter *et al.*, "Integration of distributed energy resources. The CERTS Microgrid Concept," Lawrence Berkeley National Lab.(LBNL), Berkeley, CA (United States), 2002. Accessed: 5 Nov. 2022.

[4] Mordor Intelligence, "Microgrid Market - Growth, Trends, Covid-19 Impact, and Forecasts (2022-2027)." [Online]. Available: https://www.mordorintelligence.com/industry-reports/micro-grid-market

[5] R. A. Kaushik and N. M. Pindoriya, "A hybrid AC-DC microgrid: Opportunities & key issues in implementation," in *2014 International Conference on Green Computing Communication and Electrical Engineering (ICGCCEE)*, 2014: IEEE, pp. 1-6.

[6] M. N. Alam, S. Chakrabarti, and A. Ghosh, "Networked microgrids: State-of-the-art and future perspectives," *IEEE Transactions on Industrial Informatics,* vol. 15, no. 3, pp. 1238-1250, 2018.

[7] D. Burmester, R. Rayudu, W. Seah, and D. Akinyele, "A review of nanogrid topologies and technologies," *Renewable and sustainable energy reviews,* vol. 67, pp. 760-775, 2017.

[8] J. M. Guerrero, J. C. Vasquez, J. Matas, L. G. De Vicuña, and M. Castilla, "Hierarchical control of droop-controlled AC and DC microgrids—A general approach toward standardization," *IEEE Transactions on industrial electronics,* vol. 58, no. 1, pp. 158-172, 2010.

[9] T. L. Vandoorn, J. C. Vasquez, J. De Kooning, J. M. Guerrero, and L. Vandevelde, "Microgrids: Hierarchical control and an overview of the control and reserve management strategies," *IEEE industrial electronics magazine,* vol. 7, no. 4, pp. 42-55, 2013.

[10] A. J. Wood, B. F. Wollenberg, and G. B. Sheblé, *Power generation, operation, and control*. John Wiley & Sons, 2013.

[11] C. Papadimitriou, E. Zountouridou, and N. Hatziargyriou, "Review of hierarchical control in DC microgrids," *Electric Power Systems Research,* vol. 122, pp. 159-167, 2015.

[12] N. L. Diaz, A. C. Luna, J. C. Vasquez, and J. M. Guerrero, "Centralized control architecture for coordination of distributed renewable generation and energy storage in islanded AC microgrids," *IEEE Transactions on Power Electronics,* vol. 32, no. 7, pp. 5202-5213, 2016.

[13] Y. Xu, H. Sun, W. Gu, Y. Xu, and Z. Li, "Optimal distributed control for secondary frequency and voltage regulation in an islanded microgrid," *IEEE Transactions on Industrial Informatics,* vol. 15, no. 1, pp. 225-235, 2018.

[14] D. E. Olivares *et al.*, "Trends in microgrid control," *IEEE Transactions on smart grid,* vol. 5, no. 4, pp. 1905-1919, 2014.

[15] CAISO, "Impacts of Renewable Energy on Grid Operations." Accessed: 5 Nov. 2022. [Online]. Available: https://www.caiso.com/documents/curtailmentfastfacts.pdf

[16] Z. L. J. Machowski, J. W. Bialek, and J. R. Bumby, *Power System Dynamics: Stability and Control 3rd ed.* Wiley, 2020.

[17] J. Rocabert, A. Luna, F. Blaabjerg, and P. Rodríguez, "Control of Power Converters in AC Microgrids," *IEEE Transactions on Power Electronics,* vol. 27, pp. 4734-4749, 2012.

[18] U. Tamrakar, D. Shrestha, M. Maharjan, B. P. Bhattarai, T. M. Hansen, and R. Tonkoski, "Virtual Inertia: Current Trends and Future Directions," *Applied Sciences,* vol. 7, no. 7, p. 654, 2017. [Online]. Available: https://www.mdpi.com/2076-3417/7/7/654.

[19] X. Meng, J. Liu, and Z. Liu, "A Generalized Droop Control for Grid-Supporting Inverter Based on Comparison Between Traditional Droop Control and Virtual Synchronous Generator Control," *IEEE Transactions on Power Electronics,* vol. 34, pp. 5416-5438, 2019.

[20] M. Mao, C. Qian, and Y. Ding, "Decentralized coordination power control for islanding microgrid based on PV/BES-VSG," 2018.

[21] X. Yan, X. Zhang, B. Zhang, Y. Ma, and M. Wu, "Research on Distributed PV Storage Virtual Synchronous Generator System and Its Static Frequency Characteristic Analysis," *Applied Sciences,* vol. 8, no. 4, p. 532, 2018. [Online]. Available: https://www.mdpi.com/2076-3417/8/4/532.

[22] A. F. Hoke, M. Shirazi, S. Chakraborty, E. Muljadi, and D. Maksimović, "Rapid Active Power Control of Photovoltaic Systems for Grid Frequency Support," *IEEE Journal of Emerging and Selected Topics in Power Electronics,* vol. 5, pp. 1154-1163, 2017.

[23] Z. Xing, G. Qian, Y. Hu, Z. Haizheng, and Z. Guo, "Active power reserve photovoltaic virtual synchronization control technology," *Chinese Journal of Electrical Engineering,* 2020.

[24] T. Hua, X. Yan, and W. Fan, "Research on power point tracking algorithm considered spinning reserve capacity in gird-connected photovoltaic system based on VSG control strategy," *2017 IEEE 3rd International Future Energy Electronics Conference and ECCE Asia (IFEEC 2017 - ECCE Asia),* pp. 2059-2063, 2017.

[25] S. A. Khajehoddin, M. Karimi-Ghartemani, and M. R. Ebrahimi, "Grid-Supporting Inverters With Improved Dynamics," *IEEE Transactions on Industrial Electronics,* vol. 66, pp. 3655-3667, 2019.

[26] X. Yan *et al.*, "Adaptive-MPPT-Based Control of Improved Photovoltaic Virtual Synchronous Generators," *Energies,* vol. 11, no. 7, p. 1834, 2018. [Online]. Available: https://www.mdpi.com/1996-1073/11/7/1834.

[27] M. Davari and Y. A.-R. I. Mohamed, "Robust Vector Control of a Very Weak-Grid-Connected Voltage-Source Converter Considering the Phase-Locked Loop Dynamics," *IEEE Transactions on Power Electronics,* vol. 32, pp. 977-994, 2017.

[28] M. Li *et al.*, "A novel virtual synchronous generator control strategy based on improved swing equation emulating and power decoupling method," *2016 IEEE Energy Conversion Congress and Exposition (ECCE),* pp. 1-7, 2016.

[29] W. I. Rowen, "Simplified Mathematical Representations of Single Shaft Gas Turbines in Mechanical Drive Service," in *ASME 1992 International Gas Turbine and Aeroengine Congress and Exposition*, 1992, vol. Volume 5: Manufacturing Materials and Metallurgy; Ceramics; Structures and Dynamics; Controls, Diagnostics and Instrumentation; Education, V005T15A001, doi: 10.1115/92-gt-022. [Online]. Available: https://doi.org/10.1115/92-GT-022

[30] Task Force on Turbine-Governor Modeling, "Dynamic Models for Turbine-Governors in Power System Studies," in "IEEE PES Technical Report," 29 Aug. 2013.

[31] N. Hadroug, A. Hafaifa, M. Guemana, A. Kouzou, A. Salam, and A. Chaibet, "Heavy duty gas turbine monitoring based on adaptive neuro-fuzzy inference system: speed and exhaust temperature control," *Mathematics-in-Industry Case Studies,* vol. 8, pp. 1-20, 2017.

[32] T. Sun, J. Lu, Z. Li, D. Lubkeman, and N. Lu, "Modeling Combined Heat and Power Systems for Microgrid Applications," *IEEE Transactions on Smart Grid,* vol. 9, pp. 4172-4180, 2018.

[33] H. Balaghi Enalou and E. Abbasi Soreshjani, "A Detailed Governor-Turbine Model for Heavy-Duty Gas Turbines With a Careful Scrutiny of Governor Features," *IEEE Transactions on Power Systems,* vol. 30, pp. 1435-1441, 2015.

[34] T. V. Vu, B. L. H. Nguyen, Z. Cheng, M. Y. Chow, and B. Zhang, "Cyber-Physical Microgrids: Toward Future Resilient Communities," *IEEE Industrial Electronics Magazine,* vol. 14, no. 3, pp. 4-17, 2020, doi: 10.1109/MIE.2019.2958039.

[35] I. B. Sperstad and M. Korpås, "Energy Storage Scheduling in Distribution Systems Considering Wind and Photovoltaic Generation Uncertainties," *Energies,* vol. 12, no. 7, p. 1231, 2019. [Online]. Available: https://www.mdpi.com/1996-1073/12/7/1231.

[36] X. Yang, Y. Zhang, H. He, S. Ren, and G. Weng, "Real-Time Demand Side Management for a Microgrid Considering Uncertainties," *IEEE Transactions on Smart Grid,* vol. 10, no. 3, pp. 3401-3414, 2019, doi: 10.1109/TSG.2018.2825388.

[37] M. K. Behera, I. Majumder, and N. Nayak, "Solar photovoltaic power forecasting using optimized modified extreme learning machine technique," *Engineering Science and Technology, an International Journal,* 2018.

[38] J. C. López, M. J. Rider, and Q. Wu, "Parsimonious Short-Term Load Forecasting for Optimal Operation Planning of Electrical Distribution Systems," *IEEE Transactions on Power Systems,* vol. 34, no. 2, pp. 1427-1437, 2019, doi: 10.1109/TPWRS.2018.2872388.

[39] H. Shuai, J. Fang, X. Ai, Y. Tang, J. Wen, and H. He, "Stochastic Optimization of Economic Dispatch for Microgrid Based on Approximate Dynamic Programming," *IEEE Transactions on Smart Grid,* vol. 10, pp. 2440-2452, 2019.

[40] H. Farzin, M. Fotuhi-Firuzabad, and M. Moeini-Aghtaie, "A Stochastic Multi-Objective Framework for Optimal Scheduling of Energy Storage Systems in Microgrids," *IEEE Transactions on Smart Grid,* vol. 8, pp. 117-127, 2017.

[41] M. Hosseinzadeh and F. R. Salmasi, "Robust Optimal Power Management System for a Hybrid AC/DC Micro-Grid," *IEEE Transactions on Sustainable Energy,* vol. 6, no. 3, pp. 675-687, 2015, doi: 10.1109/TSTE.2015.2405935.

[42] H. Qiu, W. Gu, Y. Xu, Z. Wu, S. Zhou, and J. Wang, "Interval-Partitioned Uncertainty Constrained Robust Dispatch for AC/DC Hybrid Microgrids With Uncontrollable Renewable Generators," *IEEE Transactions on Smart Grid,* vol. 10, no. 4, pp. 4603-4614, 2019, doi: 10.1109/TSG.2018.2865621.

[43] Y. Xiang, J. Liu, and Y. Liu, "Robust Energy Management of Microgrid With Uncertain Renewable Generation and Load," *IEEE Transactions on Smart Grid,* vol. 7, no. 2, pp. 1034-1043, 2016, doi: 10.1109/TSG.2014.2385801.

[44] J. Liu, H. Chen, W. Zhang, B. Yurkovich, and G. Rizzoni, "Energy Management Problems Under Uncertainties for Grid-Connected Microgrids: A Chance Constrained Programming Approach," *IEEE Transactions on Smart Grid,* vol. 8, no. 6, pp. 2585-2596, 2017, doi: 10.1109/TSG.2016.2531004.

[45] Y. Li, Z. Yang, G. Li, D. Zhao, and W. Tian, "Optimal Scheduling of an Isolated Microgrid With Battery Storage Considering Load and Renewable Generation Uncertainties," *IEEE Transactions on Industrial Electronics,* vol. 66, no. 2, pp. 1565-1575, 2019, doi: 10.1109/TIE.2018.2840498.

[46] B. Kouvaritakis and M. Cannon, *Model Predictive Control: Classical, Robust and Stochastic*. Springer.

[47] E. Mayhorn, L. Xie, and K. Butler-Purry, "Multi-Time Scale Coordination of Distributed Energy Resources in Isolated Power Systems," *IEEE Transactions on Smart Grid,* vol. 8, no. 2, pp. 998-1005, 2017, doi: 10.1109/TSG.2016.2547342.

[48] Y. Jia, Z. Y. Dong, C. Sun, and G. Chen, "Distributed Economic Model Predictive Control for a Wind–Photovoltaic–Battery Microgrid Power System," *IEEE Transactions on Sustainable Energy,* vol. 11, no. 2, pp. 1089-1099, 2020, doi: 10.1109/TSTE.2019.2919499.

[49] Y. Zheng, S. Li, and R. Tan, "Distributed Model Predictive Control for On-Connected Microgrid Power Management," *IEEE Transactions on Control Systems Technology,* vol. 26, no. 3, pp. 1028-1039, 2018, doi: 10.1109/TCST.2017.2692739.

[50] F. Delfino, G. Ferro, M. Robba, and M. Rossi, "An architecture for the optimal control of tertiary and secondary levels in small-size islanded microgrids," *International Journal of Electrical Power & Energy Systems,* vol. 103, pp. 75-88, 2018/12/01/ 2018, doi: https://doi.org/10.1016/j.ijepes.2018.05.026.

[51] M. A. Velasquez, J. Barreiro-Gomez, N. Quijano, A. I. Cadena, and M. Shahidehpour, "Intra-Hour Microgrid Economic Dispatch Based on Model Predictive Control," *IEEE Transactions on Smart Grid,* vol. 11, no. 3, pp. 1968-1979, 2020, doi: 10.1109/TSG.2019.2945692.

[52] S. R. Cominesi, M. Farina, L. Giulioni, B. Picasso, and R. Scattolini, "A Two-Layer Stochastic Model Predictive Control Scheme for Microgrids," *IEEE Transactions on Control Systems Technology,* vol. 26, no. 1, pp. 1-13, 2018, doi: 10.1109/TCST.2017.2657606.

[53] J. O. Lee, Y. S. Kim, and S. I. Moon, "Novel Supervisory Control Method for Islanded Droop-Based AC/DC Microgrids," *IEEE Transactions on Power Systems,* vol. 34, no. 3, pp. 2140-2151, 2019, doi: 10.1109/TPWRS.2018.2886051.

[54] A. Valibeygi, S. A. R. Konakalla, and R. d. Callafon, "Predictive Hierarchical Control of Power Flow in Large-Scale PV Microgrids With Energy Storage," *IEEE Transactions on Sustainable Energy,* vol. 12, no. 1, pp. 412-419, 2021, doi: 10.1109/TSTE.2020.3001260.

[55] V. Puvvula Sri Rama Venkata Ranga Sai Sesha and S. S. Kesanakurthy, "Model predictive control approach for frequency and voltage control of standalone micro-grid," *IET Generation, Transmission & Distribution,* vol. 12, no. 14, pp. 3405-3413, 2018, doi: https://doi.org/10.1049/iet-gtd.2017.0804.

[56] T. Morstyn, B. Hredzak, R. P. Aguilera, and V. G. Agelidis, "Model Predictive Control for Distributed Microgrid Battery Energy Storage Systems," *IEEE Transactions on Control Systems Technology,* vol. 26, no. 3, pp. 1107-1114, 2018, doi: 10.1109/TCST.2017.2699159.

[57] E. Ghahremani and I. Kamwa, "Local and Wide-Area PMU-Based Decentralized Dynamic State Estimation in Multi-Machine Power Systems," *IEEE Transactions on Power Systems,* vol. 31, no. 1, pp. 547-562, 2016, doi: 10.1109/TPWRS.2015.2400633.

[58] A. Paul, I. Kamwa, and G. Jóos, "Centralized Dynamic State Estimation Using a Federation of Extended Kalman Filters With Intermittent PMU Data From Generator Terminals," *IEEE Transactions on Power Systems,* vol. 33, no. 6, pp. 6109-6119, 2018, doi: 10.1109/TPWRS.2018.2834365.

[59] N. Zhou, D. Meng, Z. Huang, and G. Welch, "Dynamic State Estimation of a Synchronous Machine Using PMU Data: A Comparative Study," *IEEE Transactions on Smart Grid,* vol. 6, no. 1, pp. 450-460, 2015, doi: 10.1109/TSG.2014.2345698.

[60] S. Cho and J. Jiang, "Detection of Sensor Abnormalities in a Pressurizer by Means of Analytical Redundancy," *IEEE Transactions on Nuclear Science,* vol. 63, no. 6, pp. 2925-2933, 2016, doi: 10.1109/TNS.2016.2614579.

[61] P. McNamara and F. Milano, "Model Predictive Control-Based AGC for Multi-Terminal HVDC-Connected AC grids," *IEEE Transactions on Power Systems,* vol. 33, no. 1, pp. 1036-1048, 2018, doi: 10.1109/TPWRS.2017.2694768.

[62] M. Yaqoob, M. Nasir, J. C. Vasquez, and J. M. Guerrero, "Self-directed Energy Management System for an Islanded Cube Satellite Nanogrid," in *2020 IEEE Aerospace Conference*, 7-14 March 2020 2020, pp. 1-7, doi: 10.1109/AERO47225.2020.9172754.

[63] H. W. Yan, A. Narang, H. D. Tafti, G. G. Farivar, and J. Pou, "Reduced Battery Usage in a Hybrid Battery and Photovoltaic Stand-Alone DC Microgrid with Flexible Power Point Tracking," in *2020 IEEE Energy Conversion Congress and Exposition (ECCE)*, 11-15 Oct. 2020 2020, pp. 3894-3899, doi: 10.1109/ECCE44975.2020.9235615.

[64] D. Xu, A. Xu, C. Yang, and P. Shi, "A Novel Double-Quadrant SoC Consistent Adaptive Droop Control in DC Microgrids," *IEEE Transactions on Circuits and Systems II: Express Briefs*, vol. 67, no. 10, pp. 2034-2038, 2020, doi: 10.1109/TCSII.2019.2945009.

[65] D. Li and C. N. M. Ho, "Decentralized PV–BES Coordination Control With Improved Dynamic Performance for Islanded Plug-n-Play DC Microgrid," *IEEE Journal of Emerging and Selected Topics in Power Electronics*, vol. 9, no. 4, pp. 4992-5001, 2021, doi: 10.1109/JESTPE.2020.3039266.

[66] S. Sahoo, S. Mishra, S. Jha, and B. Singh, "A Cooperative Adaptive Droop Based Energy Management and Optimal Voltage Regulation Scheme for DC Microgrids," *IEEE Transactions on Industrial Electronics*, vol. 67, no. 4, pp. 2894-2904, 2020, doi: 10.1109/TIE.2019.2910037.

[67] H. Cai, J. Xiang, W. Wei, and M. Z. Q. Chen, "v- $\frac{dP}{dv}$ Droop Control for PV Sources in DC Microgrids," *IEEE Transactions on Power Electronics*, vol. 33, no. 9, pp. 7708-7720, 2018, doi: 10.1109/TPEL.2017.2771803.

[68] H. Cai, J. Xiang, and W. Wei, "Decentralized Coordination Control of Multiple Photovoltaic Sources for DC Bus Voltage Regulating and Power Sharing," *IEEE Transactions on Industrial Electronics*, vol. 65, no. 7, pp. 5601-5610, 2018, doi: 10.1109/TIE.2017.2779412.

[69] W. C. Chan, M. Armstrong, D. Atkinson, and V. Pickert, "V-dP/dI droop control technique with d2P/dI2 to improve steady state performance for multiple PV modules in a dc microgrid," in *2019 21st European Conference on Power Electronics and Applications (EPE '19 ECCE Europe)*, 3-5 Sept. 2019 2019, pp. P.1-P.10, doi: 10.23919/EPE.2019.8915405.

[70] S. Augustine, M. K. Mishra, and N. Lakshminarasamma, "A Unified Control Scheme for a Standalone Solar-PV Low Voltage DC Microgrid System With HESS," *IEEE Journal of Emerging and Selected Topics in Power Electronics*, vol. 8, no. 2, pp. 1351-1360, 2020, doi: 10.1109/JESTPE.2019.2916421.

[71] Y. Xia, M. Yu, P. Yang, Y. Peng, and W. Wei, "Generation-Storage Coordination for Islanded DC Microgrids Dominated by PV Generators," *IEEE Transactions on Energy Conversion*, vol. 34, no. 1, pp. 130-138, 2019, doi: 10.1109/TEC.2018.2860247.

[72] A. Emadi, A. Khaligh, C. H. Rivetta, and G. A. Williamson, "Constant power loads and negative impedance instability in automotive systems: definition, modeling, stability, and control of power electronic converters and motor drives," *IEEE Transactions on Vehicular Technology*, vol. 55, no. 4, pp. 1112-1125, 2006, doi: 10.1109/TVT.2006.877483.

[73] N. Pogaku, M. Prodanovic, and T. C. Green, "Modeling, Analysis and Testing of Autonomous Operation of an Inverter-Based Microgrid," *IEEE Transactions on Power Electronics*, vol. 22, no. 2, pp. 613-625, 2007, doi: 10.1109/TPEL.2006.890003.

[74] X. Wang, L. Harnefors, and F. Blaabjerg, "Unified Impedance Model of Grid-Connected Voltage-Source Converters," *IEEE Transactions on Power Electronics*, vol. 33, no. 2, pp. 1775-1787, 2018, doi: 10.1109/TPEL.2017.2684906.

[75] L. Xiong, X. Liu, Y. Liu, and F. Zhuo, "Modeling and stability issues of voltage-source converter dominated power systems: A review," *CSEE Journal of Power and Energy Systems*, pp. 1-18, 2020, doi: 10.17775/CSEEJPES.2020.03590.

[76] H. K. Khalil, *Nonlinear Systems*, 3rd ed. Upper Saddle River, NJ: Prentice Hall, 2002.

[77] T. Takagi and M. Sugeno, "Fuzzy identification of systems and its applications to modeling and control," *IEEE Transactions on Systems, Man, and Cybernetics*, vol. SMC-15, no. 1, pp. 116-132, 1985, doi: 10.1109/TSMC.1985.6313399.

[78] P. Magne, D. Marx, B. Nahid-Mobarakeh, and S. Pierfederici, "Large-Signal Stabilization of a DC-Link Supplying a Constant Power Load Using a Virtual Capacitor: Impact on the Domain of Attraction," *IEEE Transactions on Industry Applications*, vol. 48, no. 3, pp. 878-887, 2012, doi: 10.1109/TIA.2012.2191250.

[79] M. Kabalan, P. Singh, and D. Niebur, "Nonlinear Lyapunov Stability Analysis of Seven Models of a DC/AC Droop Controlled Inverter Connected to an Infinite Bus," *IEEE Transactions on Smart Grid*, vol. 10, no. 1, pp. 772-781, 2019, doi: 10.1109/TSG.2017.2752146.

[80] Y. Du, Y. Men, L. Ding, and X. Lu, "Large-Signal Stability Analysis for Inverter-Based Dynamic Microgrids Reconfiguration," *IEEE Transactions on Smart Grid*, pp. 1-1, 2021, doi: 10.1109/TSG.2021.3123937.

[81] J. G. a. W. Stevenson, *Power System Analysis*. McGraw Hill, 1994.

[82] Z. Li, W. Pei, H. Ye, and L. Kong, "Large signal stability analysis for DC microgrid under droop control based on mixed potential theory," *The Journal of Engineering*, vol. 2019, 03/01 2019, doi: 10.1049/joe.2018.8574.

[83] F. Chang, X. Cui, M. Wang, and W. Su, "Region of Attraction Estimation for DC Microgrids With Constant Power Loads Using Potential Theory," *IEEE Transactions on Smart Grid*, vol. 12, no. 5, pp. 3793-3808, 2021, doi: 10.1109/TSG.2021.3081573.

[84] S. Izumi, H. Somekawa, X. Xin, and T. Yamasaki, "Estimation of regions of attraction of power systems by using sum of squares programming," *Electrical Engineering*, vol. 100, no. 4, pp. 2205-2216, 2018/12/01 2018, doi: 10.1007/s00202-018-0690-z.

[85] Z. Zhang, R. Schuerhuber, L. Fickert, K. Friedl, G. Chen, and Y. Zhang, "Domain of Attraction's Estimation for Grid Connected Converters With Phase-Locked Loop," *IEEE Transactions on Power Systems*, vol. 37, no. 2, pp. 1351-1362, 2022, doi: 10.1109/TPWRS.2021.3098960.

[86] B. Severino and K. Strunz, "Enhancing Transient Stability of DC Microgrid by Enlarging the Region of Attraction Through Nonlinear Polynomial Droop Control," *IEEE Transactions on Circuits and Systems I: Regular Papers*, vol. 66, no. 11, pp. 4388-4401, 2019, doi: 10.1109/TCSI.2019.2924169.

[87] Y. Xia, W. Wei, T. Long, F. Blaabjerg, and P. Wang, "New Analysis Framework for Transient Stability Evaluation of DC Microgrids," *IEEE Transactions on Smart Grid*, vol. 11, no. 4, pp. 2794-2804, 2020, doi: 10.1109/TSG.2020.2964583.

[88] I. Mezić, "Koopman Operator, Geometry, and Learning," *arXiv: Dynamical Systems*, 2020.

[89] C. Josz, D. K. Molzahn, M. Tacchi, and S. Sojoudi, "Transient Stability Analysis of Power Systems via Occupation Measures," in *2019 IEEE Power & Energy Society Innovative Smart Grid Technologies Conference (ISGT)*, 18-21 Feb. 2019 2019, pp. 1-5, doi: 10.1109/ISGT.2019.8791570.

[90] M. Netto and L. Mili, "A Robust Data-Driven Koopman Kalman Filter for Power Systems Dynamic State Estimation," *IEEE Transactions on Power Systems*, vol. 33, no. 6, pp. 7228-7237, 2018, doi: 10.1109/TPWRS.2018.2846744.

[91] L. Guo *et al.*, "Data-Driven Power Flow Calculation Method: A Lifting Dimension Linear Regression Approach," *IEEE Transactions on Power Systems*, vol. 37, no. 3, pp. 1798-1808, 2022, doi: 10.1109/TPWRS.2021.3112461.

[92] P. Sharma, V. Ajjarapu, and U. Vaidya, "Data-Driven Identification of Nonlinear Power System Dynamics Using Output-Only Measurements," *IEEE Transactions on Power Systems*, vol. 37, no. 5, pp. 3458-3468, 2022, doi: 10.1109/TPWRS.2021.3131639.

[93] A. Husham, I. Kamwa, M. A. Abido, and H. Suprême, "Decentralized Stability Enhancement of DFIG-Based Wind Farms in Large Power Systems: Koopman Theoretic Approach," *IEEE Access,* vol. 10, pp. 27684-27697, 2022, doi: 10.1109/ACCESS.2022.3157747.

[94] A. Mauroy and I. Mezić, "Global Stability Analysis Using the Eigenfunctions of the Koopman Operator," *IEEE Transactions on Automatic Control,* vol. 61, no. 11, pp. 3356-3369, 2016, doi: 10.1109/TAC.2016.2518918.

[95] Y. Susuki and I. Mezić, "Nonlinear Koopman Modes and Power System Stability Assessment Without Models," *IEEE Transactions on Power Systems,* vol. 29, no. 2, pp. 899-907, 2014, doi: 10.1109/TPWRS.2013.2287235.

[96] Y. Hirase, Y. Ohara, N. Matsuura, and T. Yamazaki, "Dynamics Analysis Using Koopman Mode Decomposition of a Microgrid Including Virtual Synchronous Generator-Based Inverters," *Energies,* vol. 14, no. 15, p. 4581, 2021. [Online]. Available: https://www.mdpi.com/1996-1073/14/15/4581.

[97] S. B. Hyungjin Choi. U. o. I. a. Urbana-Champaign. (2018). Transient Stability Analysis of Power Systems using Koopman Operators. Available: https://boses.ece.illinois.edu/files/TSKoopman.pdf

[98] M. O. Williams, I. G. Kevrekidis, and C. W. Rowley, "A Data–Driven Approximation of the Koopman Operator: Extending Dynamic Mode Decomposition," *Journal of Nonlinear Science,* vol. 25, no. 6, pp. 1307-1346, 2015/12/01 2015, doi: 10.1007/s00332-015-9258-5.

[99] J. E.-R. Minghao Han, Robert K. Katzschmann, "DeSKO: Stability-Assured Robust Control with a Deep Stochastic Koopman Operator " presented at the ICLR 2022, Virtual, 25 April, 2022.

[100] V. J. Chin, Z. Salam, and K. Ishaque, "Cell modelling and model parameters estimation techniques for photovoltaic simulator application: A review," *Applied Energy,* vol. 154, pp. 500-519, 2015/09/15/ 2015, doi: https://doi.org/10.1016/j.apenergy.2015.05.035.

[101] J. P. Ram, T. S. Babu, and N. Rajasekar, "A comprehensive review on solar PV maximum power point tracking techniques," *Renewable and Sustainable Energy Reviews,* vol. 67, pp. 826-847, 2017/01/01/ 2017, doi: https://doi.org/10.1016/j.rser.2016.09.076.

[102] R. I. Putri, S. Wibowo, and M. Rifa'i, "Maximum Power Point Tracking for Photovoltaic Using Incremental Conductance Method," *Energy Procedia,* vol. 68, pp. 22-30, 2015/04/01/ 2015, doi: https://doi.org/10.1016/j.egypro.2015.03.228.

[103] H. Akagi, E. H. Watanabe, and M. Aredes, *Instantaneous power theory and applications to power conditioning,* 1st ed. Wiley-IEEE Press, 2007.

[104] P. W. Sauer, M. A. Pai, and J. H. Chow, *Power system dynamics and stability: with synchrophasor measurement and power system toolbox*. John Wiley & Sons, 2017.

[105] M. P. Kazmierkowski, Z. Lubosny, J. W. Bialek, and J. R. Bumby, *Power System Dynamics: Stability and Control*, 3rd ed. Wiley, 2020.

[106] H. Alatrash, A. Mensah, E. Mark, G. Haddad, and J. Enslin, "Generator Emulation Controls for Photovoltaic Inverters," *IEEE Transactions on Smart Grid*, vol. 3, no. 2, pp. 996-1011, 2012, doi: 10.1109/TSG.2012.2188916.

[107] J. Bai, S. Liu, Y. Hao, Z. Zhang, M. Jiang, and Y. Zhang, "Development of a new compound method to extract the five parameters of PV modules," *Energy Conversion and Management*, vol. 79, pp. 294-303, 2014/03/01/ 2014, doi: https://doi.org/10.1016/j.enconman.2013.12.041.

[108] H. Wu *et al.*, "Small-Signal Modeling and Parameters Design for Virtual Synchronous Generators," *IEEE Transactions on Industrial Electronics*, vol. 63, no. 7, pp. 4292-4303, 2016, doi: 10.1109/TIE.2016.2543181.

[109] M. Ebrahimi, S. A. Khajehoddin, and M. Karimi-Ghartemani, "An Improved Damping Method for Virtual Synchronous Machines," *IEEE Transactions on Sustainable Energy*, vol. 10, no. 3, pp. 1491-1500, 2019, doi: 10.1109/TSTE.2019.2902033.

[110] M. R. B. Tavakoli, B. Vahidi, and W. Gawlik, "An Educational Guide to Extract the Parameters of Heavy Duty Gas Turbines Model in Dynamic Studies Based on Operational Data," *IEEE Transactions on Power Systems*, vol. 24, no. 3, pp. 1366-1374, 2009, doi: 10.1109/TPWRS.2009.2021231.

[111] S. Turbines. "Centaur 40 Compressor Set." https://www.solarturbines.com/en_US/products/gas-compressor-packages/centaur-40.html (accessed 8 Nov., 2022).

[112] J. Lavaei and S. H. Low, "Zero Duality Gap in Optimal Power Flow Problem," *IEEE Transactions on Power Systems*, vol. 27, no. 1, pp. 92-107, 2012, doi: 10.1109/TPWRS.2011.2160974.

[113] S. Z. Yong, M. Zhu, and E. Frazzoli, "A unified filter for simultaneous input and state estimation of linear discrete-time stochastic systems," *Automatica*, vol. 63, pp. 321-329, 2016/01/01/ 2016, doi: https://doi.org/10.1016/j.automatica.2015.10.040.

[114] P. Kundur and N. J. Balu, *Power System Stability and Control*. McGraw-Hill, 1994.

[115] G. Zhang, J. McCalley, and Q. Wang, "An AGC Dynamics-Constrained Economic Dispatch Model," *IEEE Transactions on Power Systems*, vol. 34, no. 5, pp. 3931-3940, 2019, doi: 10.1109/TPWRS.2019.2908988.

[116] J. D. Glover, T. Overbye, and M. S. Sarma, *Power System Analysis and Design*. Cengage Learning, 2016.

[117] C. Wan, J. Zhao, Y. Song, Z. Xu, J. Lin, and Z. Hu, "Photovoltaic and solar power forecasting for smart grid energy management," *CSEE Journal of Power and Energy Systems*, vol. 1, no. 4, pp. 38-46, 2015, doi: 10.17775/CSEEJPES.2015.00046.

[118] B. Chen, P. Lin, Y. Lai, S. Cheng, Z. Chen, and L. Wu, "Very-Short-Term Power Prediction for PV Power Plants Using a Simple and Effective RCC-LSTM Model Based on Short Term Multivariate Historical Datasets," *Electronics*, vol. 9, no. 2, p. 289, 2020. [Online]. Available: https://www.mdpi.com/2079-9292/9/2/289.

[119] A. Visioli, *Practical PID Control*. Springer London, 2006.

[120] N. Hou, W. Song, and M. Wu, "Minimum-Current-Stress Scheme of Dual Active Bridge DC–DC Converter With Unified Phase-Shift Control," *IEEE Transactions on Power Electronics*, vol. 31, no. 12, pp. 8552-8561, 2016, doi: 10.1109/TPEL.2016.2521410.

[121] N. Hou and Y. Li, "Communication-Free Power Management Strategy for the Multiple DAB-Based Energy Storage System in Islanded DC Microgrid," *IEEE Transactions on Power Electronics*, vol. 36, no. 4, pp. 4828-4838, 2021, doi: 10.1109/TPEL.2020.3019761.

[122] T. L. Nguyen, G. Griepentrog, and V. T. Phung, "Modeling and control of dual active bridge converter with two control loops and output filter," in *IECON 2017 - 43rd Annual Conference of the IEEE Industrial Electronics Society*, 29 Oct.-1 Nov. 2017 2017, pp. 4683-4689, doi: 10.1109/IECON.2017.8216807.

[123] G. S. Misyris, D. I. Doukas, T. A. Papadopoulos, D. P. Labridis, and V. G. Agelidis, "State-of-Charge Estimation for Li-Ion Batteries: A More Accurate Hybrid Approach," *IEEE Transactions on Energy Conversion*, vol. 34, no. 1, pp. 109-119, 2019, doi: 10.1109/TEC.2018.2861994.

[124] U. S. EPA. "Sources of Greenhouse Gas Emissions." https://www.epa.gov/ghgemissions (accessed 2 Dec., 2022).

[125] NJBPU, "2019 New Jersey Energy Master Plan," 27 Jan. 2020. [Online]. Available: https://nj.gov/emp/docs/pdf/2020_NJBPU_EMP.pdf

[126] M. Safayatullah, M. T. Elrais, S. Ghosh, R. Rezaii, and I. Batarseh, "A Comprehensive Review of Power Converter Topologies and Control Methods for Electric Vehicle Fast Charging Applications," *IEEE Access*, vol. 10, pp. 40753-40793, 2022, doi: 10.1109/ACCESS.2022.3166935.

[127] J. J. Justo, F. Mwasilu, J. Lee, and J.-W. Jung, "AC-microgrids versus DC-microgrids with distributed energy resources: A review," *Renewable and Sustainable Energy Reviews*, vol. 24, pp. 387-405, 2013/08/01/ 2013, doi: https://doi.org/10.1016/j.rser.2013.03.067.

[128] T. Ma, H. Yang, and L. Lu, "Solar photovoltaic system modeling and performance prediction," *Renewable and Sustainable Energy Reviews*, vol. 36, pp. 304-315, 2014/08/01/ 2014, doi: https://doi.org/10.1016/j.rser.2014.04.057.

[129] A. Sangwongwanich, Y. Yang, F. Blaabjerg, and H. Wang, "Benchmarking of constant power generation strategies for single-phase grid-connected Photovoltaic systems," in *2016 IEEE Applied Power Electronics Conference and Exposition (APEC)*, 20-24 March 2016 2016, pp. 370-377, doi: 10.1109/APEC.2016.7467899.

[130] M. Akil, E. Dokur, and R. Bayindir, "The SOC Based Dynamic Charging Coordination of EVs in the PV-Penetrated Distribution Network Using Real-World Data," *Energies*, vol. 14, no. 24, p. 8508, 2021. [Online]. Available: https://www.mdpi.com/1996-1073/14/24/8508.

[131] O. Tremblay, L. A. Dessaint, and A. I. Dekkiche, "A Generic Battery Model for the Dynamic Simulation of Hybrid Electric Vehicles," in *2007 IEEE Vehicle Power and Propulsion Conference*, 9-12 Sept. 2007 2007, pp. 284-289, doi: 10.1109/VPPC.2007.4544139.

[132] M. L. Remus Teodorescu, Pedro Rodríguez, *Grid Converters for Photovoltaic and Wind Power Systems*. West Sussex, UK: Wiley-IEEE Press, 2010.

[133] H. T. Jonathan, W. R. Clarence, M. L. Dirk, L. B. Steven, and J. N. Kutz, "On dynamic mode decomposition: Theory and applications," *Journal of Computational Dynamics*, vol. 1IS - 2SP - 391, p. 421, 2014, doi: 10.3934/jcd.2014.1.391.

[134] R. Mohr and I. Mezi'c, "Construction of eigenfunctions for scalar-type operators via Laplace averages with connections to the Koopman operator," *arXiv: Spectral Theory*, 2014.

[135] E. Yeung, S. Kundu, and N. Hodas, "Learning Deep Neural Network Representations for Koopman Operators of Nonlinear Dynamical Systems," in *2019 American Control Conference (ACC)*, 10-12 July 2019 2019, pp. 4832-4839, doi: 10.23919/ACC.2019.8815339.

[136] A. Mauroy, I. Mezic, and Y. Susuki, *The Koopman Operator in Systems and Control Concepts, Methodologies, and Applications: Concepts, Methodologies, and Applications*. Springer, 2020.

[137] K. J. Åström and B. Wittenmark, *Computer-Controlled Systems: Theory and Design, Third Edition*. Dover Publications, 2011.

[138] G. Mamakoukas, O. Xherija, and T. D. Murphey, "Memory-Efficient Learning of Stable Linear Dynamical Systems for Prediction and Control," *arXiv: Learning,* 2020.

[139] N. Gillis, M. Karow, and P. Sharma, "Approximating the nearest stable discrete-time system," *Linear Algebra and its Applications,* vol. 573, pp. 37-53, 2019/07/15/ 2019, doi: https://doi.org/10.1016/j.laa.2019.03.014.

[140] D. M. Mount, (Fall 2016). *Computational Geometry*. [Online]. Available: https://www.cs.umd.edu/class/fall2016/cmsc754/Lects/cmsc754-fall16-lects.pdf

[141] B. Cousins, "Efficient high-dimensional sampling and integration," Ph.D. dissertation, Coll. Comp., Tech. GT, Atlanta, GA, USA, 2017.

[142] S. Bacha, I. Munteanu, and A. I. Bratcu, *Power Electronic Converters Modeling and Control with Case Studies*. London, UK: Springer-Verlag, 2014, pp. 55-71.

[143] L. Yao, W. H. Lim, and T. S. Tsai, "A real-time charging scheme for demand response in electric vehicle parking station," *IEEE Trans. Smart Grid*, vol. 8, no. 1, pp. 52-62, Jan. 2017.

[144] I. Nayak, M. Kumar, and F. L. Teixeira, "Detection and prediction of equilibrium states in kinetic plasma simulations via mode tracking using reduced-order dynamic mode decomposition," *J. Comput. Phys.*, vol. 447, Dec. 2021.

[145] M. A. Mahmud, T. K. Roy, S. Saha, M. E. Haque, and H. R. Pota, "Robust nonlinear adaptive feedback linearizing decentralized controller design for islanded DC microgrids," *IEEE Trans. Ind. Appl.*, vol. 55, no. 5, 650 pp. 5343-5352, Sep. 2019.

[146] A. A. Ahmadi and A. Majumdar, "DSOS and SDSOS optimization: More tractable alternatives to sum of squares and semidefinite optimization," *SIAM J. Appl. Algebra Geometry*, vol. 3, no. 2, pp. 193-230, Apr. 2019.